

Critical Heat Flux in Multi-Microchannel Copper Elements with Low Pressure Refrigerants

THÈSE N° 4223 (2008)

PRÉSENTÉE LE 30 OCTOBRE 2008

À LA FACULTE SCIENCES ET TECHNIQUES DE L'INGÉNIEUR
LABORATOIRE DE TRANSFERT DE CHALEUR ET DE MASSE
PROGRAMME DOCTORAL EN ENERGIE

ÉCOLE POLYTECHNIQUE FÉDÉRALE DE LAUSANNE

POUR L'OBTENTION DU GRADE DE DOCTEUR ÈS SCIENCES

PAR

Jung Eung PARK

M.Sc. in aerospace engineering, Korea advanced institute of science and technology, Daejeon, Corée du Sud
et de nationalité sud-coréenne

acceptée sur proposition du jury:

Prof. P. Monkewitz, président du jury
Prof. J. R. Thome, directeur de thèse
Dr G. P. Celata, rapporteur
Prof. M. Deville, rapporteur
Prof. P. Stephan, rapporteur



ÉCOLE POLYTECHNIQUE
FÉDÉRALE DE LAUSANNE

Suisse
2008

Acknowledgements

The completion of a doctoral thesis work is a long and complex task, and the author would like to thank all those who, over the years, have contributed to it. Special thanks go to Professor John Richard Thome for his support and encouragement. The discussion with him is always of interest and has yielded valuable progress continuously. I am also grateful for the lively discussion and suggestions of the thesis jury: Professors Peter Monkewitz, Gian Piero Celata and Peter Stephan. I would especially thank Professor Michel Deville for his trust and friendship.

I wish to thank the Swiss Federal Office for Professional Education and Technology (KTI) for sponsoring this work under contracts no. 6862.2 DCS-NM and 9229.1 PFNM-NM. I also wish to recognize the support of the IBM Zurich Research Laboratory for the cooperation and the fabrication of the heating elements.

Many of the ideas in this work were developed in collaboration with my colleagues. I would like to thank the present and past LTCM members for their support and stimulating conversations. I would especially thank some who have contributed regularly over the years: Bruno, Lixin, Lorenzo, Navid, Rémi and Diego.

I wish to acknowledge the ATSE technicians, especially Freddy, Laurent and Marc. I have always enjoyed working with them and have learned much from their experience. I must also record my gratitude to Cécile, Nathalie, Monique and Salomé for their careful aid for administrative work.

On a more personal side, I wish to acknowledge my good friends who have made this school period more pleasant and enjoyable. I have appreciated the time of playing football, dining and tasting coffee and wine with them. I would especially thank Bogdan and Enio for their respect and friendship. I also wish to thank the friends in the Geneva Korean church and the Bible study group in Lausanne. Among them, I would especially thank Seorim's family with whom my family has made a lot of happy memories.

I dedicate this thesis to my wife Seong Jin and our daughter Eunsu for their understanding and love.

Lausanne, October 2008

PARK Jung Eung

In his heart a man plans his course, but the LORD determines his steps.

Proverbs 16:9

Version Abrégée

De nouvelles données de flux de chaleur critique (CHF) ont été obtenues expérimentalement dans deux évaporateurs différents, faits en cuivre et composés de micro-canaux, avec trois réfrigérants à basse pression (R134a, R236fa, R245fa). Une des sections d'essai avait 20 canaux rectangulaires parallèles, larges de $467\ \mu\text{m}$ et hauts de $4052\ \mu\text{m}$, l'autre avait 29 canaux, larges de $199\ \mu\text{m}$ et hauts de $756\ \mu\text{m}$. Les micro-canaux étaient longs de 30 millimètres dans le sens de l'écoulement et la longueur chauffée au centre de l'évaporateur était de 20 millimètres. L'élément chauffant était une résistance électrique déposée sur une plaque de silicium.

Des valeurs de CHF de surface de 37 à $342\ \text{W}/\text{cm}^2$ ont été mesurées pour des flux de masse de 100 à $4000\ \text{kg}/\text{m}^2\text{s}$. En augmentant le flux de masse, on a observé que les valeurs de CHF augmentent et que le taux d'accroissement était plus petit à des flux plus élevés. La température de saturation en entrée ($10 \leq T_{\text{sat}} \leq 50^\circ\text{C}$) et le sous-refroidissement ($0 \leq \Delta T_{\text{sub}} \leq 20\ \text{K}$) ont une influence modérée ou négligeable sur le CHF, particulièrement dans le cas des canaux plus petits. Les données expérimentales ont été comparées aux méthodes de prédiction existantes. En utilisant le diamètre hydraulique chauffé équivalent D_{he} et le flux de masse réel G_{eq} dans les corrélations pour tubes circulaires, les données ont montré une bonne concordance avec plusieurs méthodes. Les données expérimentales ont également été bien prédites par un modèle théorique récent.

La visualisation de l'écoulement a été faite avec et sans orifice à l'admission de chaque micro-canal. La visualisation a confirmé l'existence d'instabilités dans l'écoulement, de recirculations et d'une distribution non-uniforme de l'écoulement dans les canaux lorsque les orifices sont enlevés. Les configurations d'écoulement dans les micro-canaux et leur évolution avec l'augmentation de flux thermique ont été observées. Les courbes d'ébullition suggèrent que dans le cas où les orifices ne sont pas présents, le commencement de l'ébullition se produit à un flux thermique plus élevé, ceci ayant pour résultat une augmentation plus élevée de la température de paroi. De plus, l'écoulement était facilement sujet à des instabilités, ce qui mena à des valeurs de CHF beaucoup plus basses que celles mesurées lorsque les orifices étaient en place.

Mots-clé: CHF, micro-canal, écoulement en ébullition, réfrigérant, refroidissement de microprocesseur

Abstract

New saturated critical heat flux (CHF) data have been obtained experimentally in two different multi-microchannel heat sinks made in copper with three low pressure refrigerants (R134a, R236fa, R245fa). One of the test sections had 20 parallel rectangular channels, $467\ \mu\text{m}$ wide and $4052\ \mu\text{m}$ deep while the second had 29 channels, $199\ \mu\text{m}$ wide and $756\ \mu\text{m}$ deep. The microchannels were 30 mm long in the flow direction where a 20 mm length in the middle was heated with an electrical resistance deposited on a silicon plate.

Base CHF values were measured from 37 to $342\ \text{W}/\text{cm}^2$ for mass velocities from 100 to $4000\ \text{kg}/\text{m}^2\text{s}$. When increasing the mass velocity, CHF was observed to increase while the rate of increase was slower at high velocities. While CHF increased moderately with large inlet subcooling (e.g. 20 K) in the $H = 4052\ \mu\text{m}$ channels, inlet subcooling seemed to play less a role as the channel size decreased. CHF showed reversed tendency with increasing inlet saturation temperature ($10 \leq T_{\text{sat}} \leq 50^\circ\text{C}$) for the two test sections. The experimental data were compared with existing prediction methods. The data demonstrated good agreement with several predictive methods using the heated equivalent diameter D_{he} and the actual mass velocity G_{eq} to implement the circular tube correlations.

Flow visualization was conducted with and without an orifice at the inlet of each microchannel. Visualization confirmed the existence of flow instability, back flow and non-uniform distribution of flow among the channels when the orifices were removed. Flow patterns in the microchannels and their evolution with increasing heat flux were observed. The flow boiling curves suggest that in the case of omitting the orifice, the boiling incipient occurred at a higher heat flux resulting in a higher overshoot of wall temperature. Moreover, the flow was easily subjected to instability and caused CHF to occur at much lower values than occurred with the orifices in place.

Key words: Critical heat flux, microchannel, flow boiling, refrigerant, chip cooling

Contents

List of figures	8
List of tables	12
1 Introduction	15
2 State of the art of critical heat flux in microchannels	17
2.1 Experimental data for microchannel CHF	17
2.2 Discussion of the experimental data	30
2.3 CHF prediction methods	31
2.4 Summary and problem statement	38
3 Experimental facility	39
3.1 Description of the Test Facility	39
3.1.1 Flow Loop	39
3.1.2 Test section	42
3.1.3 Measurement system	47
3.2 Operation and data reduction processes	50
3.2.1 Operating procedures	50
3.2.2 Data reduction for wall heat flux, q_w	52
3.3 Uncertainty Analysis	56
3.3.1 Uncertainty of measurement	56
3.3.2 Uncertainty of results and the main sources of error	56
3.3.3 Additional uncertainty considerations	60
3.3.4 Conclusions	60

4	Validation	63
4.1	Energy Balance	63
4.2	Single Phase Pressure Drop Measurement	66
4.3	Conclusion	70
5	Experimental results	73
5.1	Flow boiling curves	73
5.2	Effect of parameters	77
5.3	Conclusions	79
6	CHF prediction methods and their comparison to the database	81
6.1	CHF prediction methods	81
6.2	Comparison results	84
6.2.1	Comparison for each geometrical definition	84
6.2.2	Comparison for each test section	85
6.2.3	Detailed analysis of each prediction method	89
6.3	Conclusions	93
7	Effect of inlet orifice and flow visualization	95
7.1	Flow characteristics without the inlet orifice insert	95
7.2	Flow characteristics with the inlet orifice insert	100
7.3	Comparison of flow boiling curves and CHF results	107
7.4	Conclusions	110
8	General Conclusions	111
A	CHF database	113
B	Step-by-step procedures for uncertainty analysis	121
	Nomenclature	133
	Bibliography	137
	Curriculum Vitae	141

List of Figures

1.1	Schematic diagram of an annular liquid film and dry out location. e_B , e_w , and d represent droplet entrainment due to boiling and disturbance waves, and droplet deposition, respectively (see Ref. [9]).	15
2.1	Flow boiling curves for 0.51 mm diameter tubes for subcooling of 10, 20 and 30 K (see Ref. [6]).	18
2.2	Superheated exit conditions with measured exit fluid temperatures and predicted exit saturation temperatures (see Ref. [6]).	19
2.3	A test section with 17 circular tubes of 0.51 mm diameter (see Ref. [6]).	20
2.4	Variation of CHF with mass velocity for 30 K and 60 K inlet subcooling (see Ref. [34]). . . .	21
2.5	Sketch of the observed vapor back flow at a heat flux near CHF (see Ref. [34]).	22
2.6	Variation of CHF with mass velocity in 0.5 and 0.8 mm diameter tubes (see Ref. [46]).	23
2.7	Influence of inlet subcooling on CHF (see Ref. [46]).	24
2.8	A flow boiling curve generated during the measurement of CHF (see Ref. [46]).	24
2.9	Microchannel devices and inlet restriction configuration (see Ref. [26]).	25
2.10	Average surface temperatures of the devices at $G = 265 \text{ kg/m}^2\text{s}$ (see Ref. [26]).	26
2.11	Comparison of OUB with CHF correlations (see Ref. [26]).	26
2.12	CHF dependence on exit pressure (see Ref. [27]).	27
2.13	Experimental wall CHF results as a function of the mass velocity for R236fa, $L = 20 \text{ mm}$, $W = 223 \text{ }\mu\text{m}$, $H = 680 \text{ }\mu\text{m}$ and $T_{\text{sat}} = 26^\circ\text{C}$ (see Ref. [3]).	28
2.14	Comparison between the experimental CHF data and the Wojtan et al. correlation (see Ref. [3]).	28
2.15	Comparison between the experimental CHF data and the Revellin and Thome correlation (see Ref. [3]).	29
2.16	Comparison of the Katto-Ohno correlation with saturated CHF data (see Ref. [47]).	32
2.17	Comparison of the Shah correlation with saturated CHF data (see Ref. [47]).	33
2.18	Control volume of two phase flow in annular flow regime (see Ref. [37]).	37

2.19	CHF model showing the annular film thickness variation along the channel plotted versus the wave height. The simulation is for R-134a at a saturation temperature of 30°C in a 0.5 mm channel of 20 mm heated length without inlet subcooling for a mass velocity of 500 kg/m ² s, yielding a CHF of 396 kW/m ² (see Ref. [37]).	37
3.1	A schematic diagram of the test facility for CHF measurement.	40
3.2	The top view of the H = 756 μ m microchannel heat sink.	42
3.3	Test section for CHF measurement with ten micro-thermocouples.	43
3.4	The top and bottom view of the test section. The location of each thermocouple is shown with its index in parenthesis (unit: mm). Flow direction is from left to right.	44
3.5	Test section assembly.	45
3.6	(a) serpentine heater deposited on a silicon substrate, (b) circular hole type orifice for H = 4052 μ m channels, and (c) slot type orifice for H = 756 μ m channels.	46
3.7	Schematic of local property variation and wall heat flux.	52
3.8	Schematic of the microchannels.	55
3.9	Wall CHF data for R236fa at $T_{\text{sat}} = 25^\circ\text{C}$ in H = 756 μ m.	59
3.10	Wall CHF data for R134a at $T_{\text{sat}} = 25^\circ\text{C}$ in H = 4052 μ m ignoring the systematic error due to the CHF detection method and the error in estimating the actual heating area.	60
3.11	Wall CHF data for R134a at $T_{\text{sat}} = 25^\circ\text{C}$ in H = 756 μ m ignoring the systematic error due to the CHF detection method and the error in estimating the actual heating area.	61
4.1	Energy loss measured in single phase experiments for R245fa in the H = 4052 μ m test section showing the error band.	65
4.2	Energy loss measured in single phase experiments for R245fa in the H = 756 μ m test section showing the error band.	65
4.3	Friction factors computed from the single phase pressure drop measurements at different Reynolds numbers in the H = 4052 μ m test section without an orifice.	68
4.4	Total and singular pressure drops measured at different mass velocities at adiabatic conditions, and their second order curve fit for the singularity constant, in the H = 4052 μ m test section without an orifice.	69
4.5	Total and singular pressure drops measured at different mass velocities at adiabatic conditions, and their second order curve fit for the singularity constant, in the H = 4052 μ m test section with a 300 μ m circular orifice at the entrance of each channel.	69
4.6	Comparison of total pressure drop in the H = 756 μ m test section with and without 200 μ m rectangular slit orifices at the entrance of each channel.	71

4.7	Friction factors computed from the single phase pressure drop measurements at different Reynolds numbers in the $H = 756 \mu\text{m}$ test section with $200 \mu\text{m}$ rectangular slit orifices at the entrance of each channel.	71
5.1	Three types of flow boiling curve measured by the 3rd(red circle), 5th(blue square) and 8th(green triangle) thermocouples located at 5 mm, 9 mm and 15 mm downstream from the front edge of the heater, respectively (See Figure 3.4).	75
5.2	Local wall temperature and local wall heat flux at $G = 3000 \text{ kg/m}^2\text{s}$, $T_{\text{sat}} = 25^\circ\text{C}$, and $\Delta T_{\text{sub}} = 3 \text{ K}$ and $q_b = 206 \text{ W/cm}^2$ with R134a.	76
5.3	CHF data for R134a at $T_{\text{sat}} = 25^\circ\text{C}$ in $H = 4052 \mu\text{m}$ channels.	77
5.4	CHF data for R134a at $T_{\text{sat}} = 25^\circ\text{C}$ in $H = 756 \mu\text{m}$ channels.	78
5.5	Effect of channel size with R134fa at $T_{\text{sat}} = 20^\circ\text{C}$	79
5.6	CHF data for different refrigerants at $T_{\text{sat}} = 25^\circ\text{C}$ and $\Delta T_{\text{sub}} = 5 \text{ K}$ in $H = 756 \mu\text{m}$ channels.	80
5.7	CHF data for different inlet saturation temperatures at fixed inlet subcooling of 5 K.	80
6.1	Comparison of all data with the Katto-Ohno [22] correlation using D_{he} and G_{eq}	86
6.2	Comparison of all data with the Wojtan et al. [46] correlation using D_{he} and G_{eq}	87
6.3	Comparison of all data with the Revellin-Thome [37] numerical method using D_{he} and G_{eq}	88
6.4	Katto-Ohno prediction to measured CHF versus test parameters.	90
6.5	Wojtan et al. prediction to measured CHF versus test parameters.	91
6.6	Revellin-Thome prediction to measured CHF versus test parameters.	92
7.1	Visualization of the $H = 4052 \mu\text{m}$ test section at a high mass velocity (a) without and (b) with the orifice insert. Flow direction is from left to right. Red dashed line shows the heating area. Bright area in the channels represents single phase liquid (near inlet) or annular flow (near outlet) while dark area represents two phase bubble mixture.	97
7.2	Visualization of the $H = 4052 \mu\text{m}$ test section at a low mass velocity (a) without and (b) with the orifice insert. $G = 80 \text{ kg/m}^2\text{s}$, $T_{\text{sat}} = 40^\circ\text{C}$, $\Delta T_{\text{sub}} = 20 \text{ K}$ and $q_b = 115 \text{ W/cm}^2$. Flow direction is from left to right. Red dashed line shows the heating area. Bright area in the channels represents single phase liquid (near inlet) or annular flow (near outlet) while dark area represents two phase bubble mixture. Very bright area represents dryout zone in top image.	98
7.3	Sequence of images with time near the inlet of channels showing back flow and parallel channel instability in a case with no orifice insert. The main flow direction is from left to right at $G = 240 \text{ kg/m}^2\text{s}$, $T_{\text{sat}} = 50^\circ\text{C}$, $\Delta T_{\text{sub}} = 20 \text{ K}$ and $q_b = 212 \text{ W/cm}^2$ in the $H = 4052 \mu\text{m}$ test section.	99
7.4	Flow patterns at different heat fluxes at $T_{\text{sat}} = 50^\circ\text{C}$, $\Delta T_{\text{sub}} = 20 \text{ K}$, $G = 200 \text{ kg/m}^2\text{s}$ with R245fa in the $H = 4052 \mu\text{m}$ test section.	101

7.5	Visualization of recirculating flow near the inlet with the orifice insert installed. Sequence of images on one channel at the frame rate of 4000 image/sec (every 5 msec) during 6.25 msec. Images are for R134a at $T_{\text{sat}} = 21^\circ\text{C}$, $\Delta T_{\text{sub}} = 11\text{ K}$, $G = 680\text{ kg/m}^2\text{s}$ and $q_b = 100\text{ W/cm}^2$ in the $H = 4052\text{ }\mu\text{m}$ test section. Bright area represents single phase liquid while dark area represents bubble mixture.	103
7.6	Visualization of recirculating flow near the inlet with the orifice insert installed. Sequence of images on one channel taken every 5 msec during 80 msec. Images are for R245fa at $T_{\text{sat}} = 50^\circ\text{C}$, $\Delta T_{\text{sub}} = 30\text{ K}$, $G = 200\text{ kg/m}^2\text{s}$ and $q_b = 45\text{ W/cm}^2$ in the $H = 4052\text{ }\mu\text{m}$ test section.	104
7.7	(a) Visualization of inlet jet stream near the inlet with the orifice insert installed and (b) a schematic diagram of the video image. Images are for R245fa at $T_{\text{sat}} = 50^\circ\text{C}$, $\Delta T_{\text{sub}} = 17\text{ K}$, $G = 106\text{ kg/m}^2\text{s}$ and $q_b = 172\text{ W/cm}^2$ in the $H = 4052\text{ }\mu\text{m}$ test section.	105
7.8	(a) Visualization of flashing effect through the orifice insert installed and (b) a schematic diagram of the video image. Images are for R134a at $T_{\text{sat}} = 17^\circ\text{C}$, $\Delta T_{\text{sub}} = 0\text{ K}$, $G = 280\text{ kg/m}^2\text{s}$ and $q_b = 20\text{ W/cm}^2$ in the $H = 4052\text{ }\mu\text{m}$ test section.	106
7.9	Flow boiling curves at $G = 2000\text{ kg/m}^2\text{s}$, $T_{\text{sat}} = 25\text{ }^\circ\text{C}$ and $\Delta T_{\text{sub}} = 10\text{ K}$ with R134a in $H = 756\text{ }\mu\text{m}$ channels with and without the orifice.	107
7.10	Wall CHF versus subcooling at $T_{\text{sat}} = 50\text{ }^\circ\text{C}$ with R245fa in $H = 4052\text{ }\mu\text{m}$ channels with and without the orifice.	108
7.11	Wall CHF versus subcooling at $T_{\text{sat}} = 25\text{ }^\circ\text{C}$ with R134a in $H = 756\text{ }\mu\text{m}$ channels with and without the orifice.	109
7.12	Wall CHF versus mass velocity at $T_{\text{sat}} = 25\text{ }^\circ\text{C}$ and $\Delta T_{\text{sub}} = 5\text{ K}$ with R134a in $H = 756\text{ }\mu\text{m}$ channels with and without the orifice.	109
B.1	Illustration of the systematic and random error [4].	123
B.2	Wall CHF data for R236fa at $T_{\text{sat}} = 25^\circ\text{C}$ in $H = 756\text{ }\mu\text{m}$	130

List of Tables

2.1	Correlations for multi channel saturated CHF	34
2.2	Correlations for single channel saturated CHF	35
3.1	List of loop elements	41
3.2	Measurement system components	49
3.3	Range of test conditions	50
3.4	Measurement uncertainty summary.	57
3.5	Uncertainty of the results	59
4.1	Rectangular ducts $K(\infty)$, $f_d \cdot \text{Re}$ and C to be used in Equation 4.6 from Shah and London [40]	67
4.2	Contribution of inlet and outlet configuration on the singular pressure loss coefficient in the $H = 4052 \mu\text{m}$ test section.	70
5.1	Changes of parameters during the wall temperature excursion in Figure 5.1 (a)	76
6.1	Correlations for saturated CHF	82
6.2	Definition of diameters and values	83
6.3	Mean absolute error (MAE) of experimental data to the prediction	84
A.1	Range of test conditions and the number of data points acquired	113
A.2	Presentation of CHF database	120
B.1	The main independent measurement parameters and their nominal values.	122
B.2	Random error of each parameter	124
B.3	Elemental systematic error sources.	126
B.4	Measurement uncertainty summary.	127

B.5	Propagation of measurement uncertainties in the local wall CHF.	128
B.6	Propagation of measurement uncertainties in the mass velocity.	129
B.7	Propagation of measurement uncertainties in the local wall CHF.	129
B.8	Uncertainty of the results	130

Chapter 1

Introduction

Critical heat flux (CHF) refers to the value of heat flux at which the local heat transfer coefficient decreases sharply due to the replacement of liquid by vapor adjacent to the heat transfer surface. There exists other terminologies for this condition in the literature such as burnout, DNB (departure from nucleate boiling), dryout, and boiling crisis; however, none of these is fully satisfactory. For saturated flow boiling, CHF is assumed to occur in annular flow when the liquid film on the heated wall dries out as illustrated in Figure 1.1 by Celata et al. [9]. In most cases, once this limiting condition is detected as a sharp rise of surface temperature, the heating power must be cut before the component physically burns out. For designing microprocessor chip cooling systems and for the cooling of power electronics, knowledge of the CHF is essential in determining the upper operating limit of the cooling system for safe operation.

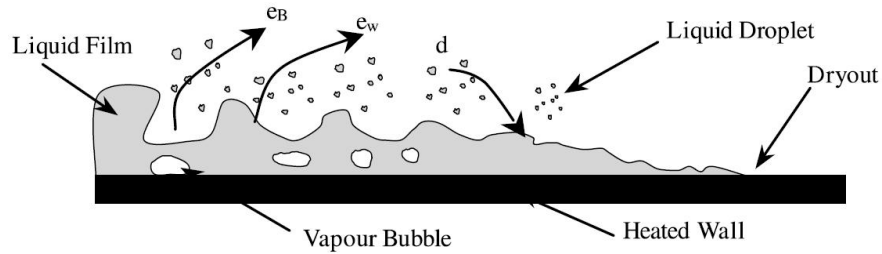


Figure 1.1: Schematic diagram of an annular liquid film and dry out location. e_B , e_w , and d represent droplet entrainment due to boiling and disturbance waves, and droplet deposition, respectively (see Ref. [9]).

The microelectronics and power electronics industries are now facing the challenge of removing very high heat fluxes of 300 W/cm^2 or more while maintaining their operating temperature below the targeted temperature, such as 85°C for CPUs. Although conventional cooling solutions, such as air-cooled heat sinks, have been used successfully until now, no straightforward extension is expected for such high heat fluxes (Chu et al. [10]). Alternative solutions such as jet impingement cooling, single-phase and two-phase cooling in microchannels have been explored and showed different advantages or drawbacks (e.g. Agostini et al. [2], Colgan et al. [12] and Faulkner et al. [15]). Among them, two-phase flow boiling in microchannels seems to be the most promising approach.

The energy consumption by data centers, or servers, has doubled from 2000 to 2005 due to the rapid expansion of internet based companies such as Google according to Koomy [25]. The percentage of electricity consumed by such centers in the United States is comparable to that of a color television in each home, and the total amount is equivalent to the power generated by five 1000 MW power plants. As a consequence, energy saving issues have begun to drive the development of efficient systems in the electronics industry. Since two-phase cooling in microchannels is a highly effective heat transfer mechanism, its potential to reduce energy consumption by data centers has been noted by the industry. However, an understanding of micro-channel Critical Heat Flux (CHF) is needed to determine the maximum heat dissipation rates and safe operating limit of such systems.

Presently in the literature, the experimental data available for CHF in multi-microchannel cooling elements is quite limited, in particular for refrigerants that are the most promising candidates to act as the working fluid in such systems. Thus, the objective of this work is to experimentally investigate CHF in several multi-microchannel test elements for three different refrigerants, perform a flow visualization study on the process and develop an approach to achieve stable flow with good uniformity in the distribution to numerous parallel flow channels.

The present thesis is organized as follows. Chapter 2 presents the state of the art review on saturated CHF research in mini or micro channels covering experiments and prediction methods. Chapter 3 provides the description of the test loop built for CHF tests, followed by its operating procedures, the data reduction process and discussions on the uncertainty of results. Chapter 4 shows the estimation of single phase pressure drops and heat losses to validate the current measurement. Chapter 5 presents the experimental results achieved in this study. Flow boiling curves and the effect of each input parameter were analyzed. In Chapter 6, the experimental results were compared with existing prediction methods. Chapter 6 provides visualization of multi-microchannel flow taken by a high speed camera. Investigation on the effect of an orifice on flow behavior and CHF were also presented. Finally, general conclusions and the ideas for future research are given in Chapter 8. All the CHF data acquired in this research and detailed process for uncertainty analysis were provided separately in Appendices.

Chapter 2

State of the art of critical heat flux in microchannels

A very large database of CHF already exists in the literature (e.g. Hall and Mudawar [16] and Zhang et al. [47]); however, most of the work has been aimed at macro scale systems, such as for nuclear power plants. Accordingly, a great portion of these studies employed a single macroscale circular tube. To maximize CHF, flow conditions of high mass velocity and high operating pressure have been tested with highly subcooled water and refrigerants. Extensive reviews of the work for subcooled CHF were provided by Celata et al. [8] and Katto [21].

However, for computer chip cooling, a moderate pressure is generally preferred for practical reasons. Furthermore, a relatively low mass flow rate in small channels with minimal subcooling at the entrance is preferred to reduce the pump power. Therefore, saturated CHF is encountered with these flow conditions. Additionally, instead of circular channels, non-circular channels functioning in parallel are more common in chip cooling modules for the convenience of fabrication. The application of macroscale methods based on a single circular macrochannel to predict CHF in mini/micro rectangular multi-channels with saturated exit conditions is not necessarily appropriate (Thome [43] [44]), which will be also shown by the experimental studies discussed below.

In this chapter, recent studies on saturated CHF conducted with mini or micro channels (essentially channels smaller than 3 mm in diameter) are reviewed. Newly conducted experiments on this subject are listed in the first section. Some issues related to the experimental data are discussed in the second section. Empirical correlations and theoretical models to predict CHF are summarized in the next section. Finally, unresolved issues in the literature are presented, with reference to the problems to be tackled by this thesis.

2.1 Experimental data for microchannel CHF

Bowers and Mudawar (1994)

Bowers and Mudawar [6] performed saturated CHF tests for flow in an array of circular tubes inserted in a test block. R113 was tested over mass velocities from 31 to 150 kg/m²s for mini-channels (2.54 mm

diameter) and 120-480 kg/m²s for micro-channels (0.51 mm diameter). The inlet pressure was 1.38 bar and the inlet subcooling ranged from 10 K and 32 K. In contrast to previous CHF correlations in a single channel (e.g. Katto and Ohno [22]), a lack of inlet subcooling effect on CHF was observed. Figure 2.1 shows flow boiling curves at different inlet subcooling conditions. Regardless of the subcooling, the curves converged at high heat fluxes and yielded an identical CHF value of just below 200 W/cm² relative to the base area. They explained that since the fluid reached the saturation temperature far before arriving at CHF, the inlet subcooling barely affected CHF.

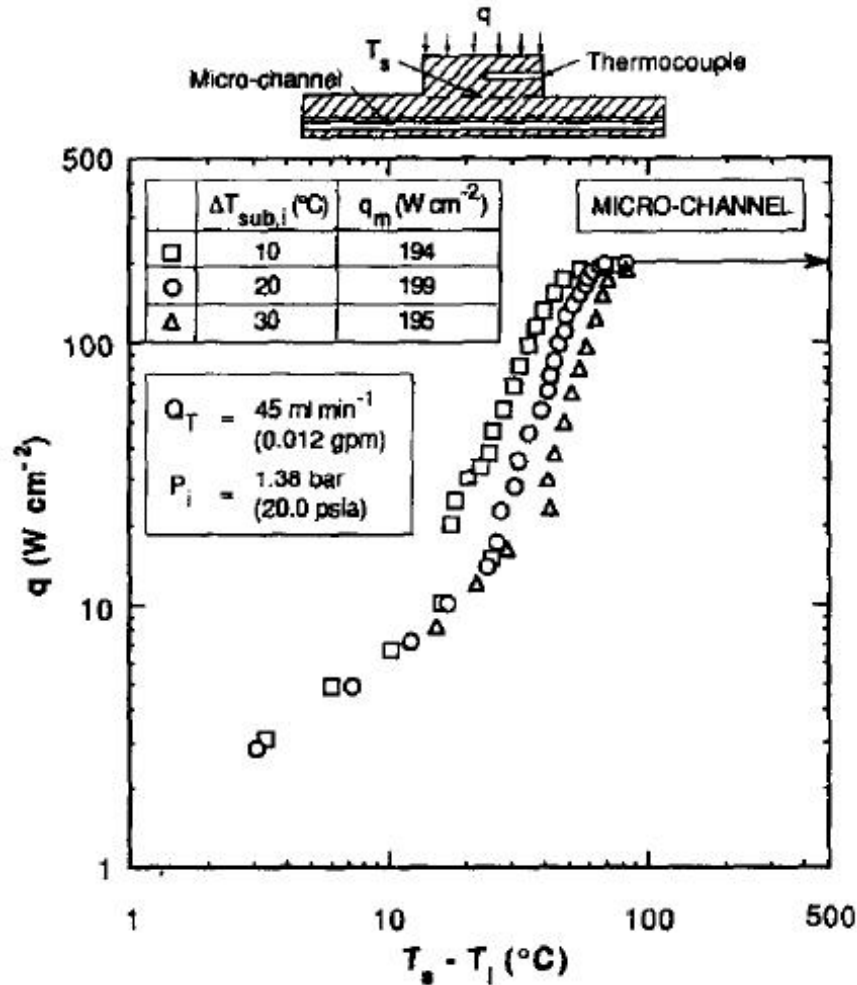


Figure 2.1: Flow boiling curves for 0.51 mm diameter tubes for subcooling of 10, 20 and 30 K (see Ref. [6]).

Another interesting feature of their results is illustrated in Figure 2.2. For the test cases at low flow rates, the exit fluid temperature exceeds the outlet saturation temperature. Even though the fluid reaches total dryout, a superheated exit condition is attained before encountering CHF. Figure 2.3 shows the test section and heating element used in their study. It consists of a nickel plate and a copper block which were silver-soldered together. A thick-film resistor was soldered on the top area of the copper block to generate heating. An overall temperature was measured using a thermocouple inserted in the copper block and corrected by the one-dimensional heat conduction theory. A superheated outlet condition was maintained by spreading

heat laterally through the thickness of the copper block before inducing the overall wall temperature rise. It is noticed that their assumption of 1D heat conduction is no longer valid in this case, which may increase the measurement uncertainty. Furthermore, use of only one centrally located thermocouple is rather limiting when trying to detect CHF, because CHF is supposed to occur at the end of the channel first and then to propagate backwards towards the entrance as the surface progressively heats up.

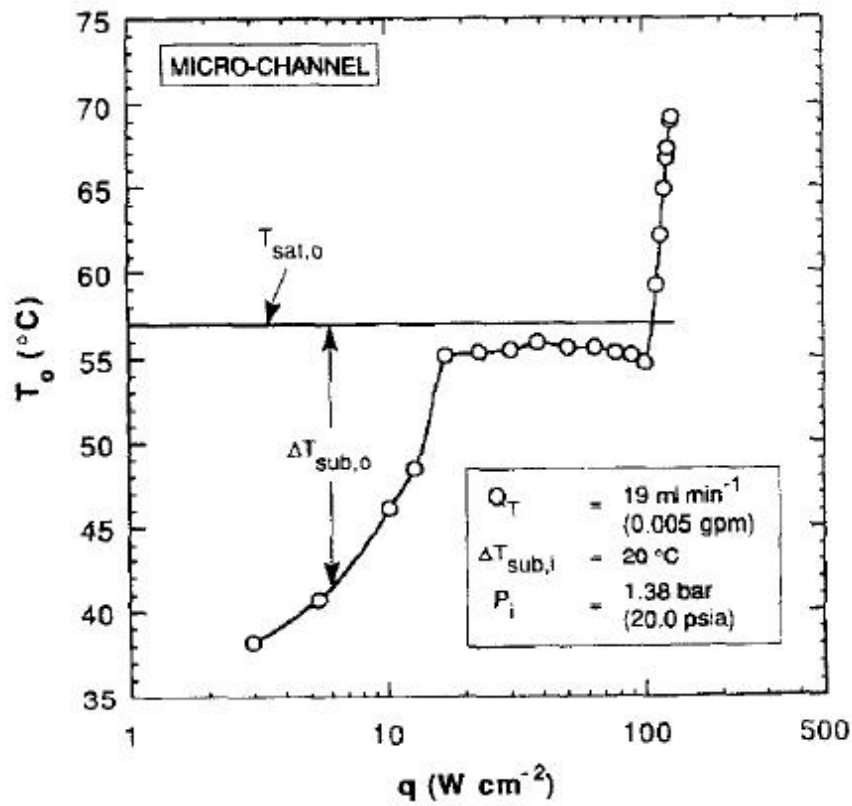


Figure 2.2: Superheated exit conditions with measured exit fluid temperatures and predicted exit saturation temperatures (see Ref. [6]).

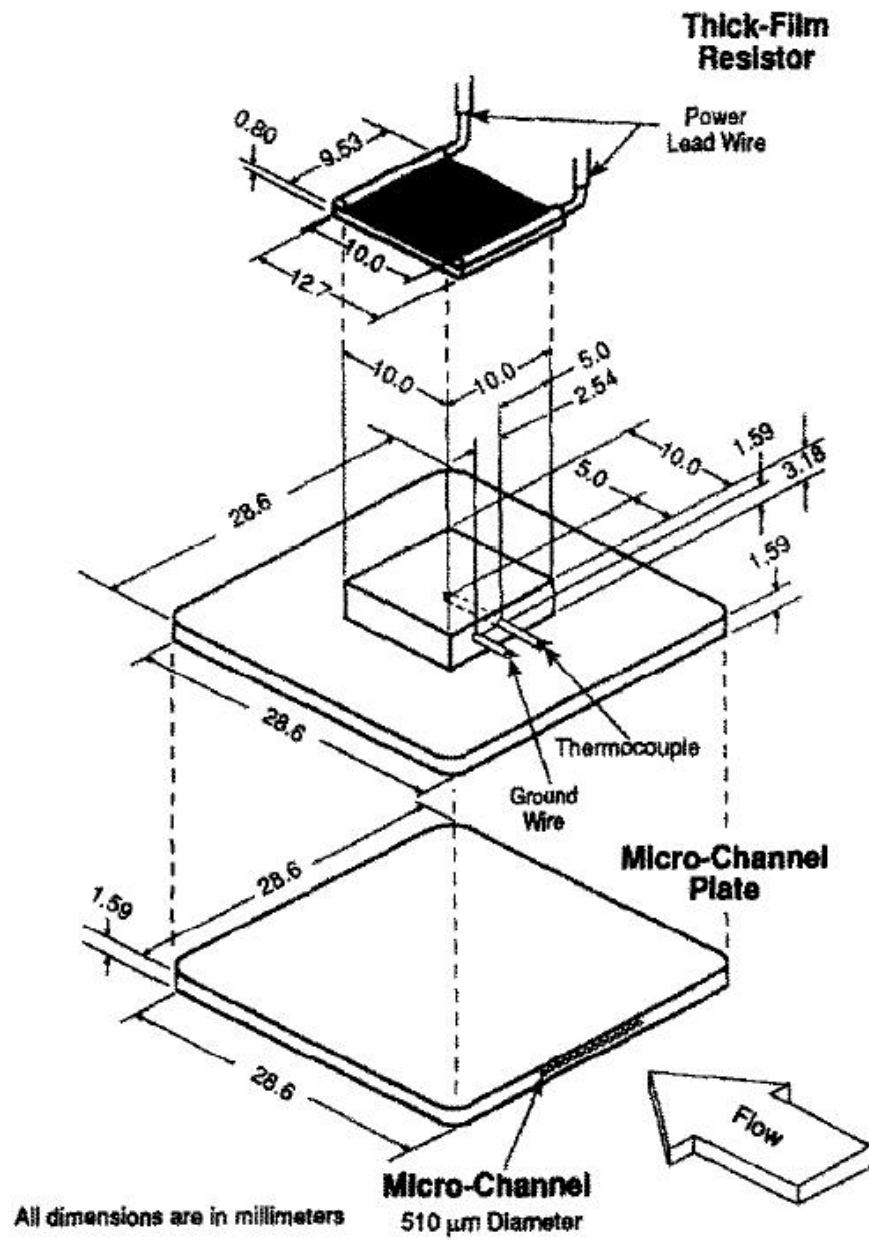


Figure 2.3: A test section with 17 circular tubes of 0.51 mm diameter (see Ref. [6]).

Qu and Mudawar (2004)

Qu and Mudawar [34] conducted saturated water CHF tests in a new microchannel copper heat sink composed of an array of 21 rectangular channels of $215 \times 821 \mu\text{m}$ (width \times depth) machined in its top surface. The top area was 10 mm in width and 44.8 mm in length. New CHF data at 18 flow conditions were reported over a mass velocity range of 86-368 $\text{kg/m}^2\text{s}$ with two inlet fluid temperatures, 30°C and 60°C , at an inlet pressure close to the ambient (thus with 70 K and 40 K of subcooling, respectively). As shown in Figure 2.4, a lack of subcooling effect on CHF was observed similar to Bowers and Mudawar [6] and was attributed to an instability inherent to their multi-channel configuration with periodic backflow into the inlet header. This explanation seems to be more appropriate than that of Bowers and Mudawar [6] to explain the unusual lack of subcooling effect. Although an instability from the upstream compressible volume was reduced by controlling a valve in front of the inlet, a Ledinegg instability was still observed as sketched in Figure 2.5. When approaching CHF, this instability also induced an abnormal increase of the inlet fluid temperature.

No superheated exit condition was reported, even though their channels were machined on a copper block of significant volume which allowed lateral heat conduction. On the contrary, the exit vapor quality of the newly reported CHF values ranges from as low as 0.172 at the highest mass flow rate to 0.562 at the lowest flow rate.

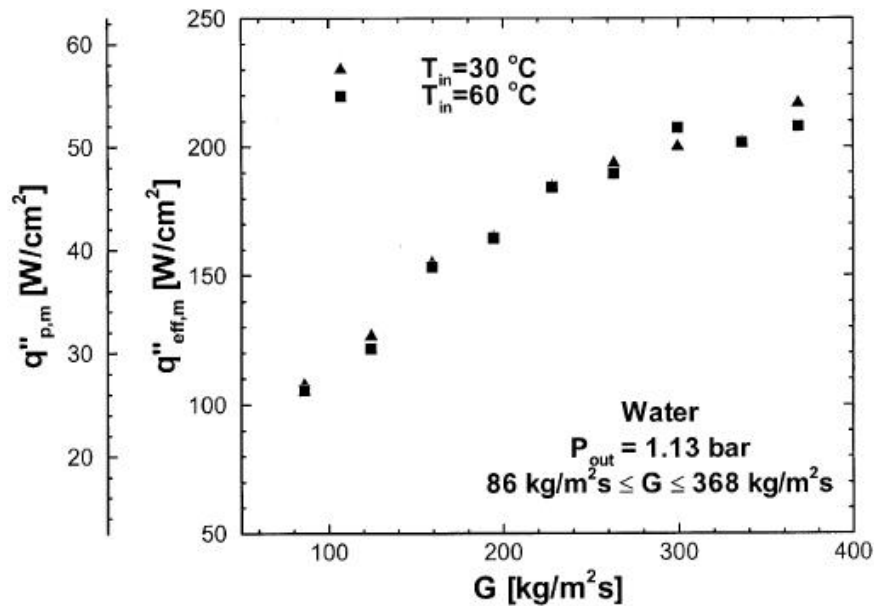


Figure 2.4: Variation of CHF with mass velocity for 30 K and 60 K inlet subcooling (see Ref. [34]).

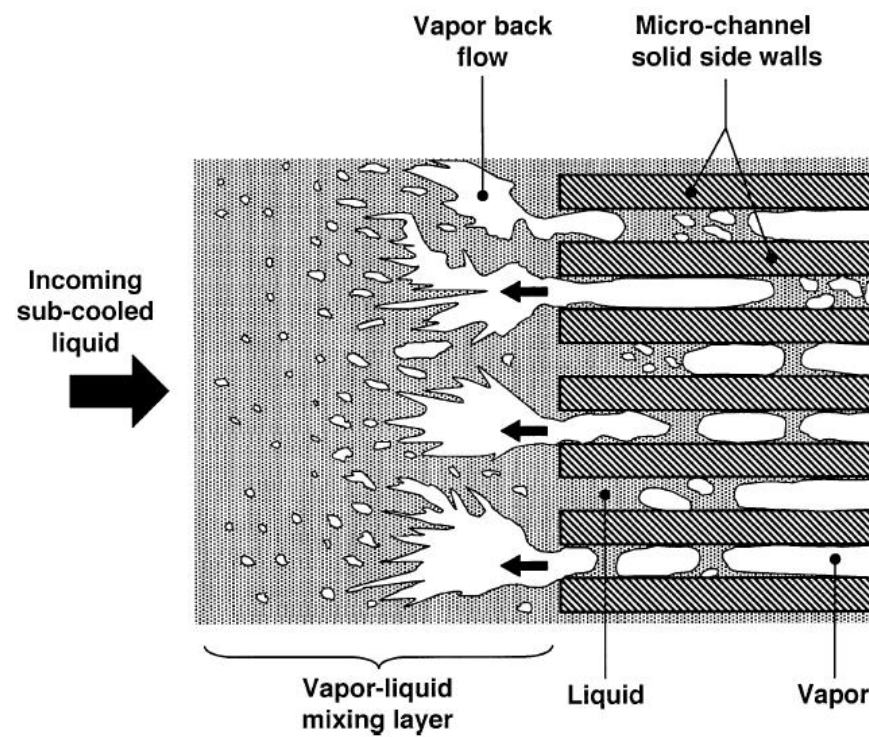


Figure 2.5: Sketch of the observed vapor back flow at a heat flux near CHF (see Ref. [34]).

Wojtan et al. (2006)

Wojtan et al. [46] conducted a series of saturated CHF tests with R134a and R245fa, which are promising coolants for electronic cooling applications. A single circular tube was heated electrically over lengths from 20 to 70 mm. Flow was stabilized using a valve just before their preheater used to set the inlet subcooling. Figure 2.6 shows the measured variation of CHF as a function of mass velocity and inner tube diameter. The CHF increased with mass velocity and tube diameter (0.5 and 0.8 mm). The tests were conducted with small inlet subcoolings ranging from 4.5 to 12 K and showed no significant influence of this parameter, as shown in Figure 2.7. This trend agreed with the tests of Qu and Mudawar [34] and Bowers and Mudawar [6], both of which were conducted in multi-channels. In fact, Qu and Mudawar explained this as a result of an instability inherent in multi-channel heat sinks which is not the case here. The flow conditions in the Wojtan et al. tests were reported to be stable and thus instability was not an issue. Nonetheless, the flow boiling curve in Figure 2.8 suggests that the temperature difference between the wall and the fluid saturation temperature becomes unstable as the heat flux approaches CHF. CHF was determined to occur always in the annular flow regime as identified in the flow pattern map developed in a companion study by Revellin et al. [35].

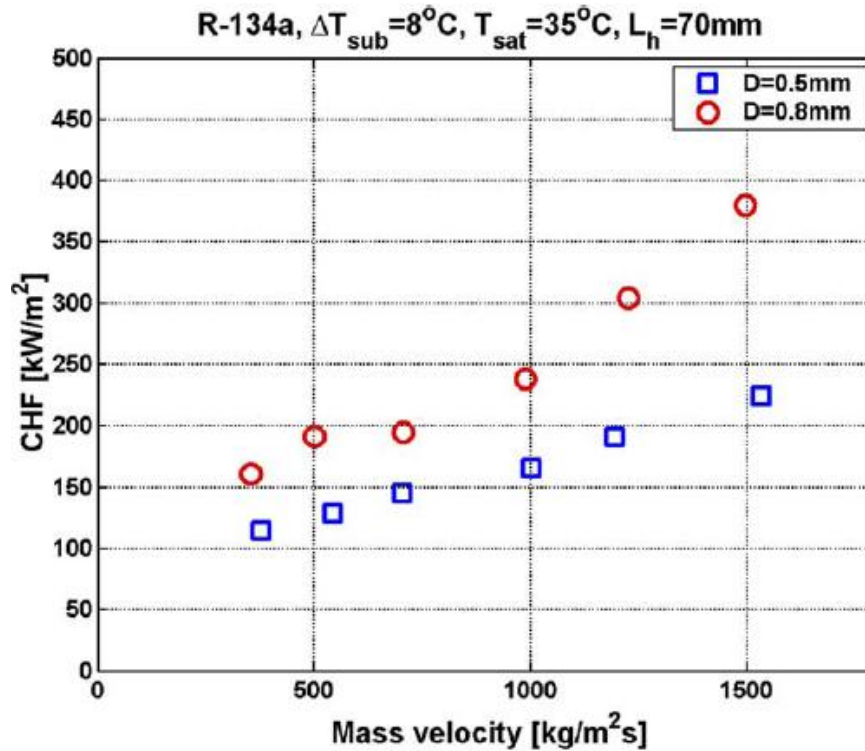


Figure 2.6: Variation of CHF with mass velocity in 0.5 and 0.8 mm diameter tubes (see Ref. [46]).

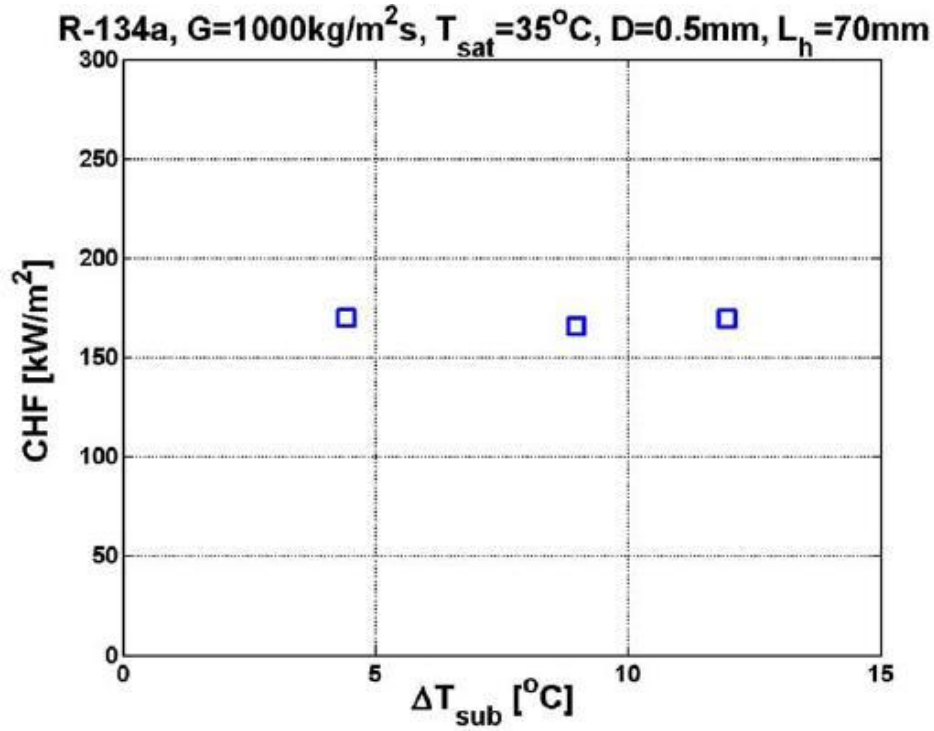


Figure 2.7: Influence of inlet subcooling on CHF (see Ref. [46]).

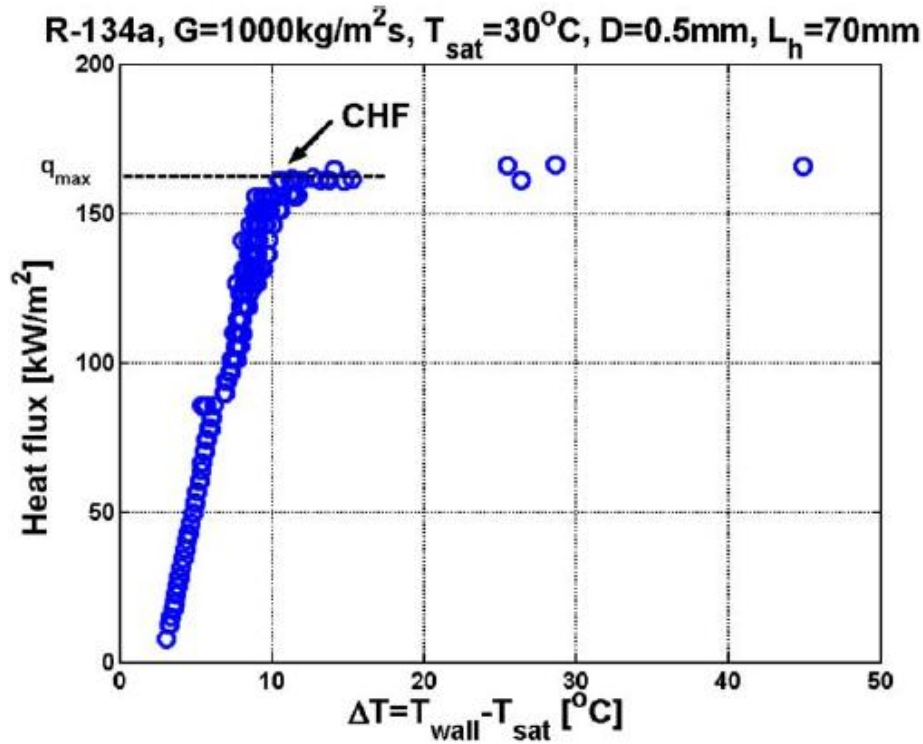


Figure 2.8: A flow boiling curve generated during the measurement of CHF (see Ref. [46]).

Kosar et al. (2006, 2007)

Kosar et al. [26] examined the effect of an inlet flow restriction to suppress the instabilities encountered in multi-microchannels. Orifices of zero, 50, 100 and 400 μm in length with the same 20 μm width were fabricated at the inlet of each microchannel. The test section consisted of 5 microchannels of $200 \times 264 \times 10000$ μm (width \times depth \times length) as shown in Figure 2.9. The onset of unstable boiling (OUB) was measured at mass velocities of 115–389 $\text{kg}/\text{m}^2\text{s}$ with water.

Figure 2.10 shows their flow boiling curves from using the different orifices. Even though all the flow boiling curves fall on a single curve, the OUB was increased by using higher pressure drop orifices. Interestingly, the OUBs of 3R200 and 4R400 are almost the same, suggesting that the applied inlet flow resistance is sufficient to avoid the hydrodynamic instabilities. Comparison of these data with existing CHF prediction methods showed that the trends in OUB agreed qualitatively well (but not quantitatively) with existing CHF correlations as illustrated in Figure 2.11.

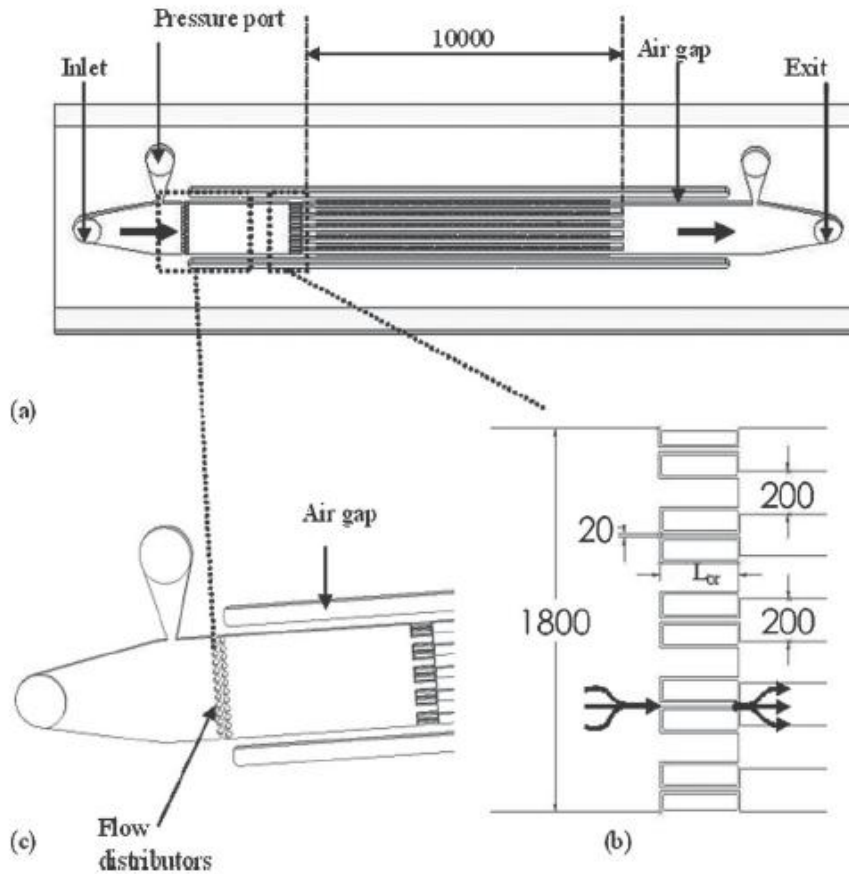


Figure 2.9: Microchannel devices and inlet restriction configuration (see Ref. [26]).

Kosar and Peles [27] later reported CHF data of R-123 gathered in the same test section. In this experimentation, only the orifices of 400 μm in length were used to suppress flow instability. They found that their CHF data increased with mass velocity and decreased with exit quality. With increasing pressure, CHF increased up to a certain value but decreased beyond the maximum (Figure 2.12). They explained that several key parameters were correlated with the system pressure: the latent heat of vaporization, the

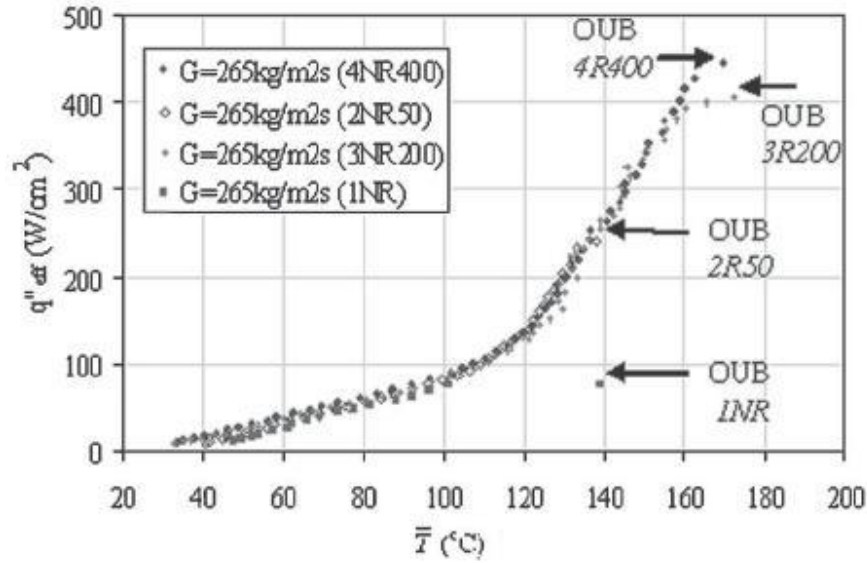


Figure 2.10: Average surface temperatures of the devices at $G = 265 \text{ kg/m}^2\text{s}$ (see Ref. [26]).

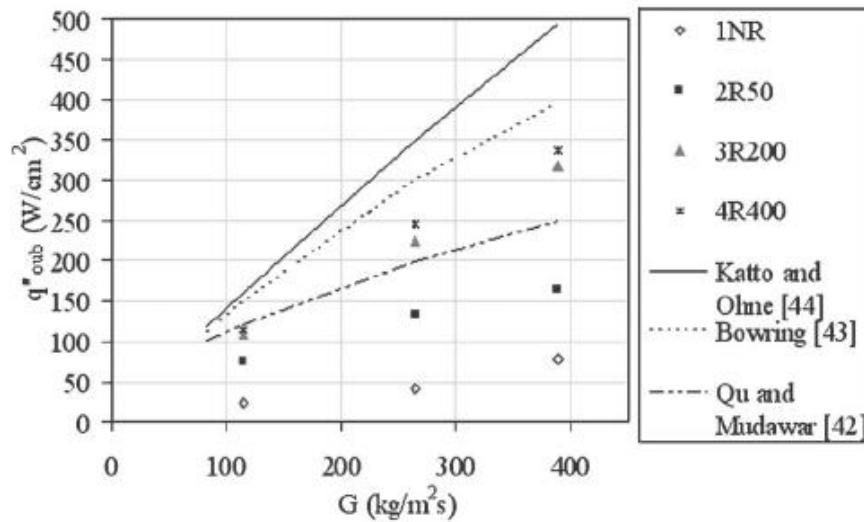


Figure 2.11: Comparison of OUB with CHF correlations (see Ref. [26]).

liquid to vapor density ratio, the surface tension and the inlet subcooling for the same inlet temperature. Those parameters worked adversely with increasing system pressure, which caused a local maximum in the CHF value. From flow visualization, they identified that dryout was the leading CHF mechanism for their experimental conditions.

Kandlikar et al. (2006)

Similar to the above study, Kandlikar et al. [19] investigated the effect of an inlet pressure restriction and fabricated nucleation sites as a means to prevent instability. Their inlet manifold was modified to reduce

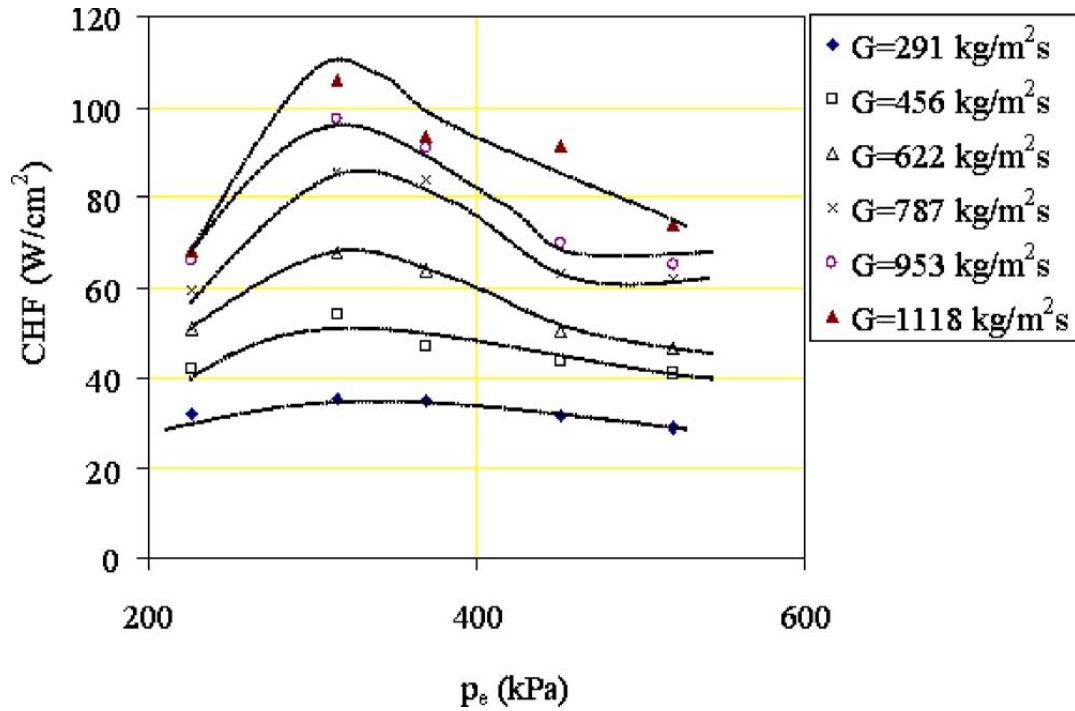


Figure 2.12: CHF dependence on exit pressure (see Ref. [27]).

the opening area of each channel inlet to 51% and 4% of the channel cross-section. The 51% area element partially reduced pressure fluctuations but failed to eliminate flow reversal. For the case of the 4% area restriction with fabricated nucleation sites, flow reversal was completely avoided. However, the pressure drop was significantly increased due to the reduced inlet area. The possibility of improving heat transfer performance by stabilizing the flow was also suggested.

Agostini et al. (2008)

Agostini et al. [3] measured saturated CHF for R236fa in a silicon multi-microchannel heat sink composed of 67 parallel channels, which were $223 \times 680 \mu\text{m}$ (width \times depth) with $80 \mu\text{m}$ thick fins separating the channels. An orifice of $500 \times 223 \mu\text{m}$ was used at the inlet of each channel to inhibit flow instabilities and backflow. Five RTDs (Resistance Temperature Detectors) were deposited on the lower face of the silicon die to measure wall temperature as well as a serpentine resistance heater for generating heat flux. The CHF increased with mass velocity but the inlet saturation temperature and the inlet subcooling were found to have a negligible influence on CHF in their test conditions. Figures 2.13 to 2.15 shows some of their test results.

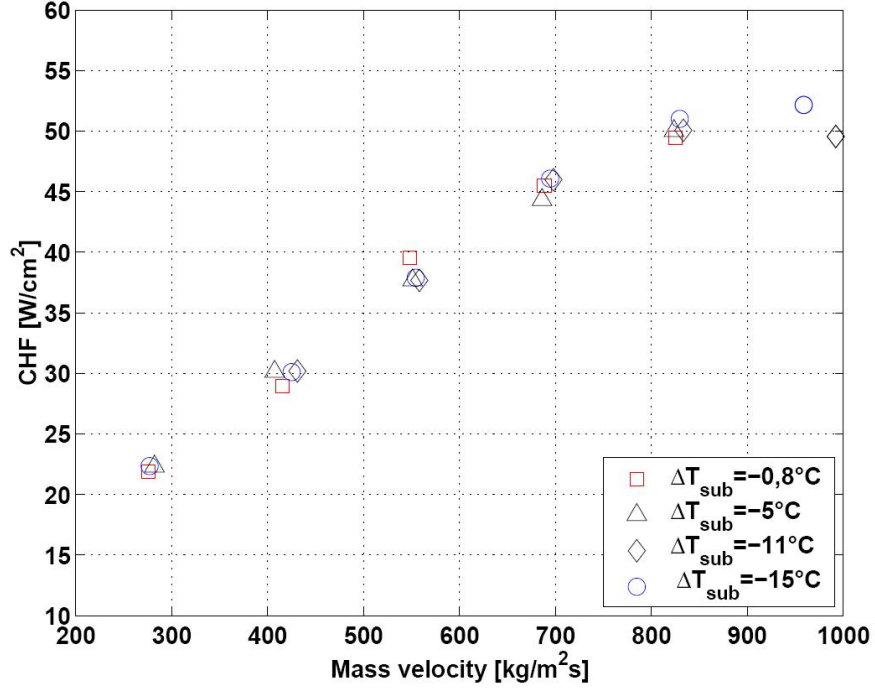


Figure 2.13: Experimental wall CHF results as a function of the mass velocity for R236fa, $L = 20$ mm, $W = 223 \mu\text{m}$, $H = 680 \mu\text{m}$ and $T_{\text{sat}} = 26^\circ\text{C}$ (see Ref. [3]).

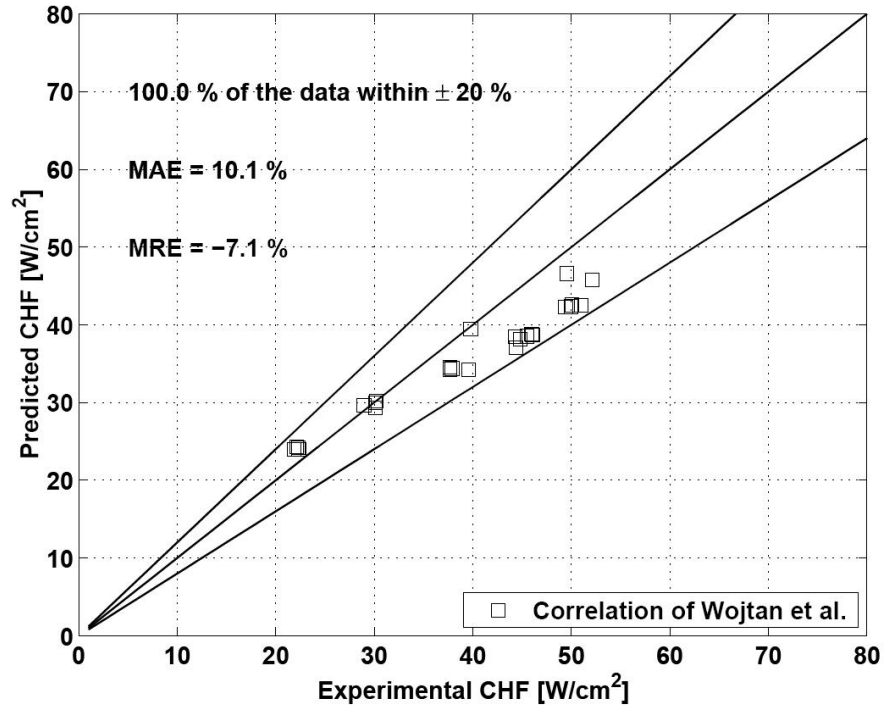


Figure 2.14: Comparison between the experimental CHF data and the Wojtan et al. correlation (see Ref. [3]).

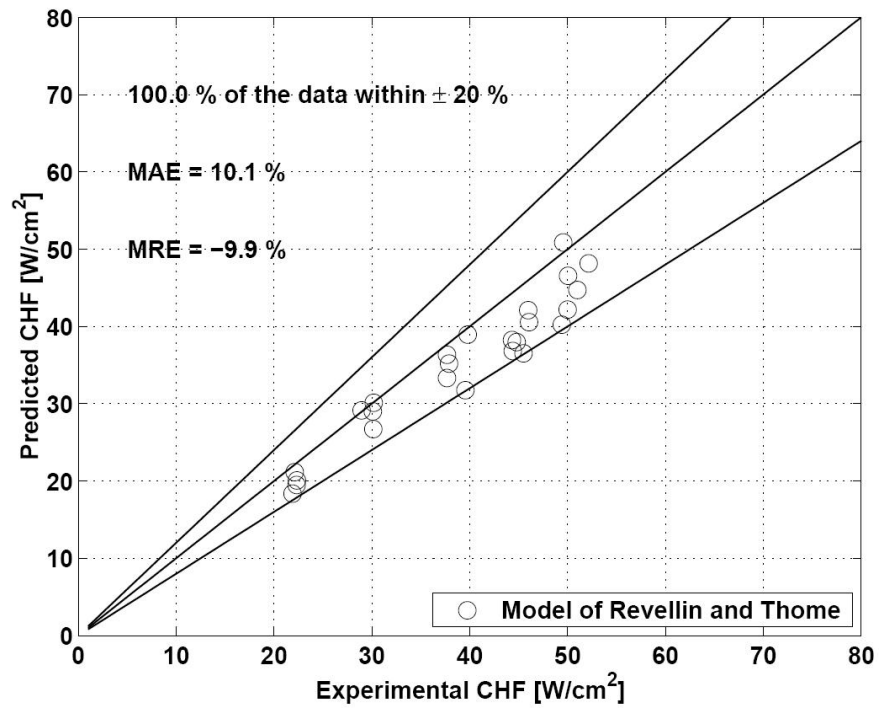


Figure 2.15: Comparison between the experimental CHF data and the Revellin and Thome correlation (see Ref. [3]).

2.2 Discussion of the experimental data

Bergles and Kandlikar (2005)

Bergles and Kandlikar [5] reviewed the existing CHF studies on saturated CHF in microchannels and suggested a guideline for new studies. Since most of the existing small-tube data taken at high mass velocities were not applicable to the micro-channel heat sink design, more data covering a wider range of fluids, channel configurations and operating conditions at low mass velocities were recommended. They also suggested investigations on the CHF mechanism itself. An instability issue was highly emphasized by arguing that all of the previous tests in multi-microchannels, at the time of their 2005 review, were conducted at unstable conditions. Upstream compressible volume instability and excursive instability were suggested as the two major instabilities affecting CHF in microchannels. The experiment of Qu and Mudawar [34] was argued to be influenced by instability since their proposed correlation is opposite to the conventional correlation for water. Namely, they predicted that CHF decreases with decreasing diameter. Furthermore, the vapor backflow observation negated the inlet subcooling effect. It was suggested that the data were subject to the excursive instability even though a throttle valve was installed to avoid the compressible volume instability. Therefore, the CHF value is lower than the real CHF that would be taken in a stable condition. Installing a restriction at the inlet of each channel was suggested to eliminate the excursive or Ledinegg instability, which was examined by Kosar et al. [26] and Kandlikar et al. [19].

In addition to this, several guidelines were suggested for future studies: (1) Flow distribution should not be a problem for the flow boiling in microchannels since the two phase pressure drop in the channels will be much higher than the pressure drop in the inlet plenum; (2) To handle conjugate effects in rectangular channels, a numerical approach seems to be the only option since measuring a local temperature around the circumference of a microchannel is unrealistic; (3) Particular attention is needed to deal with the experimental uncertainty; (4) Visual observation is preferred to investigate the effect of flow pattern, flow stagnation and flow reversal.

Finally, Bergles and Kandlikar [5] gave guidelines for future studies into CHF in microchannels. They suggested the need for more CHF tests at conditions appropriate for real applications of the microchannels, while considering the issues associated with microchannel heat sinks such as instability.

Pribyl et al. (2003)

Pribyl et al. [33] investigated the flow regime dependence on the flow boiling CHF of macroscale data. A databank compiled at Columbia University was sorted by the use of the Taitel-Dukler flow regime map [41] and examined by plotting the regime-sorted CHF data against the vapor quality. The data were also compared with predictions from existing correlations.

Plotting the flow regime-sorted CHF versus the vapor quality proved that CHF varies linearly with quality at a different slope for each flow regime. In addition, several prediction methods such as Bowring [7] and Katto and Ohno [22] were evaluated for the different flow regime data. In the bubble and annular flow regimes, the correlations were far more accurate than the CHF predictions in intermittent flow. They concluded that flow regimes appeared to influence the hydrodynamic and heat transfer mechanisms that define CHF. Therefore, they suggested that a regime-based correlation may well yield significant improvements in predicting CHF.

2.3 CHF prediction methods

Empirical correlations

The basic forms of the correlations to predict multichannel and single channel saturated CHF are summarized in Tables 2.1 and 2.2, respectively.

Qu and Mudawar [34] also evaluated the validity of the existing correlations by comparing them with the CHF data from their laboratory. The widely used Katto-Ohno [22] and Bowring [7] correlations compared well with data in a single channel gathered from the literature. However, these methods failed to correlate the multi-channel test data of Bowers and Mudawar [6] and their new data. Since no previous correlation matched their test data, they developed a modified version of the Katto-Ohno correlation [22] for their multi-channel CHF data.

Wojtan et al. [46] found a significant discrepancy between their experimental data and the predictions of the Katto-Ohno [22] and Qu and Mudawar [34] correlations. Therefore, a new correlation based on a modification of the Katto-Ohno correlation [22] was suggested based on their data for two refrigerants and two microchannel diameters.

Kosar et al. [26] developed a correlation based on their parametric studies for quantifying the onset of unstable boiling. The effect of the inlet orifice was considered by introducing a pressure drop multiplier parameter M :

$$M = \frac{\Delta p_{\text{ch}} + \Delta p_{\text{ori}}}{\Delta p_{\text{ch}}} \quad (2.1)$$

Based on the observation that the OUB increased asymptotically with M , and the assumption that the OUB is directly related to the CHF, the following correlation was suggested:

$$q_{\text{OUB}} = 0.00375 \cdot G \cdot h_{lv} \cdot \text{We}^{-0.06} \cdot x_{\text{o},400\mu\text{m}}^{-0.32} [1 - \exp(-1.005 \cdot \text{Re}^{-0.37} \cdot M^{0.82})] \quad (2.2)$$

where q_{OUB} is the heat flux at the onset of unstable boiling, $x_{\text{o},400\mu\text{m}}$ is the outlet vapor quality in the test section of the 400 μm orifice, and We and Re are Weber number and Reynolds number, respectively. It was deduced that the OUB in microscale channels would be more effected by instabilities as the channel size decreased if the inlet restriction was not reduced sufficiently.

Kosar and Peles [27] suggested a new CHF correlation for multichannel saturated CHF based on their R-123 tests. Since no existing correlation followed their CHF trend with the system pressure, they developed a new CHF correlation as a function of the exit pressure.

Zhang et al. [47] evaluated the existing CHF correlations for flow boiling of water in mini-channels. Available CHF data in the literature for small diameters, ranging from 0.33 to 6.22 mm, were collected. Then, these data were classified as either subcooled or saturated CHF. For saturated CHF, which is appropriate for electric chip cooling, the Bowring [7], Katto-Ohno [22] and Shah [39] correlations were evaluated. The short form of each of these multichannel correlations can be found in Table 2.1. Among them, the Shah correlation was proved to predict values with the smallest mean deviation. They found that the Katto-Ohno correlation correlates all the data successfully with a relatively small scatter but predicts slightly higher values. The

Bowring correlation was reported to deviate systematically from the experimental data at high CHF values, even though low CHF values were generally well predicted. The comparison of saturated CHF data with the Katto-Ohno and Shah correlations are illustrated in Figure 2.16 and Figure 2.17, respectively.

Even though all the existing correlations predicted the saturated CHF values generally well, each of them consists of many empirical constants, equations and complicated conditional statements for choosing the proper expression. Moreover, significant discontinuities were found at each boundary between the adjoining equations for neighboring ranges of conditions, causing jumps which are not observed in experimental data. Such jumps also create problems when one wishes to find an optimum solution in thermal design. Therefore, a new correlation was developed systematically with the aid of an artificial neural network technique and a parametric trend analysis. The new water only correlation proved to have the smallest mean deviation among all the tested correlations for the collected database and consists of only one single equation shown in Table 2.2

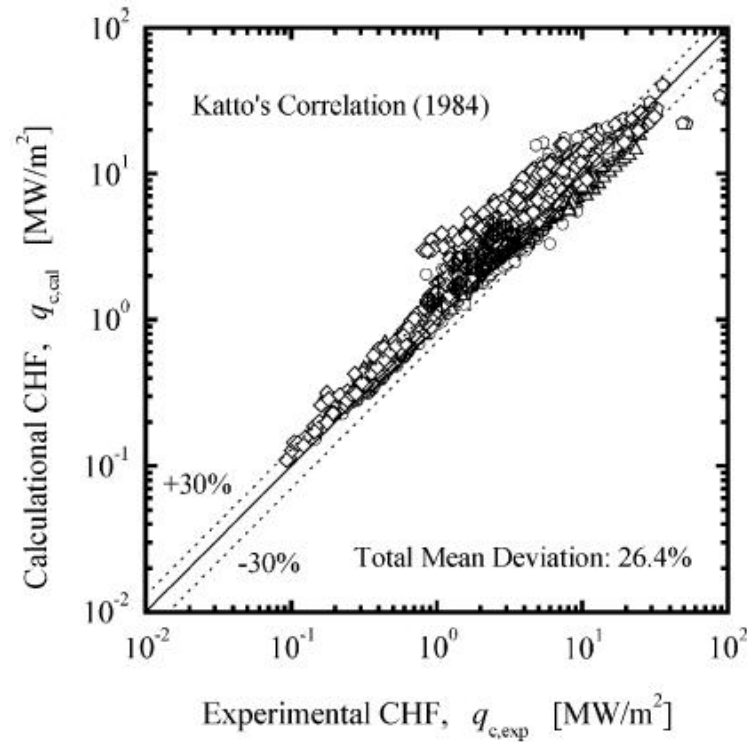


Figure 2.16: Comparison of the Katto-Ohno correlation with saturated CHF data (see Ref. [47]).

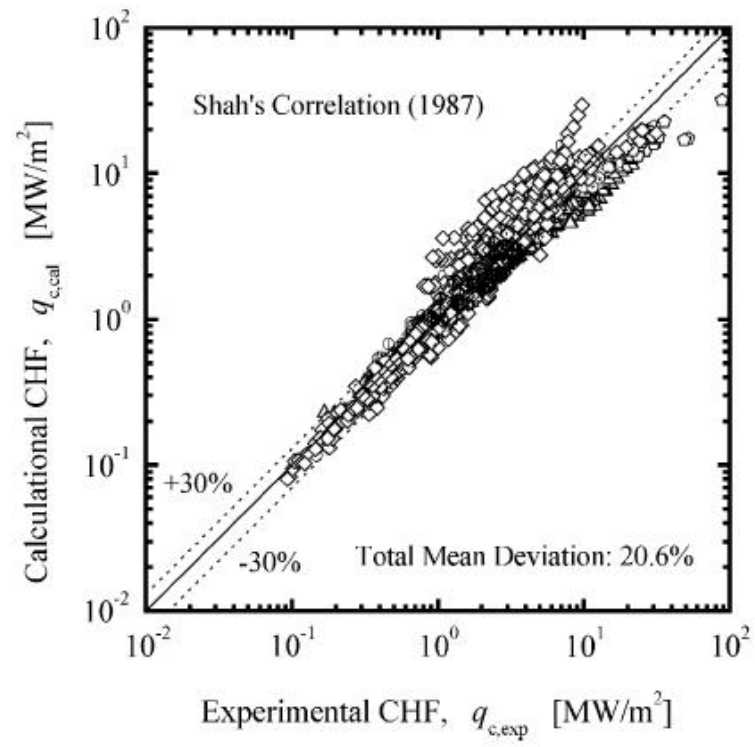


Figure 2.17: Comparison of the Shah correlation with saturated CHF data (see Ref. [47]).

Table 2.1: Correlations for multi channel saturated CHF

Reference	Basic form of CHF correlation
Bowring [7]	$q_c = \frac{A' + 0.25 \cdot D_h \cdot G \cdot \Delta h_{\text{in}}}{C' + L}$ $A', C' = \text{fn}(D_h, G, h_{lv}, p_o)$
Qu and Mudawar [34]	$q_c = 33.43 \cdot G \cdot h_{lv} \cdot \text{We}^{-0.21} \left(\frac{\rho_v}{\rho_l} \right)^{1.11} \left(\frac{L}{D} \right)^{-0.36}$
Kosar et al. [26]	$q_c = 0.00375 \cdot G \cdot h_{lv} \cdot \text{We}^{-0.06} \cdot x_{o,400\mu\text{m}}^{-0.32} \cdot [1 - \exp(-1.005 \cdot \text{Re}^{-0.37} \cdot M^{0.82})]$ $M = \frac{\Delta p_{\text{ch}} + \Delta p_{\text{ori}}}{\Delta p_{\text{ch}}}$
Kosar and Peles [27]	$q_c = G \cdot h_{lv} \cdot \left(\left[9.34 \times 10^{-2} \frac{p_o}{p_c} - 0.34 \left(\frac{p_o}{p_c} \right)^2 - 1.3 \times 10^{-4} \right] x_o^{0.59} \right)^{1/1.08}$

Table 2.2: Correlations for single channel saturated CHF

Reference	Basic form of CHF correlation
	$q_c = q_{c0} \left(1 + K \frac{\Delta h_{\text{in}}}{h_{lv}} \right)$
Katto and Ohno [22] Katto [20]	$\frac{q_{c0}}{G \cdot h_{lv}} = \text{fn} \left(\frac{\rho_v}{\rho_l}, \text{We}, \frac{L}{D} \right)$ $\text{We} = \frac{G^2 L}{\sigma \rho_l}$
	Upstream condition correlation (UCC)
	$\frac{q_c}{G \cdot h_{lv}} = \text{fn} \left(\frac{L}{D_h}, Y, x_{\text{in}} \right)$
Shah [39]	Local condition correlation (LCC)
	$\frac{q_c}{G \cdot h_{lv}} = \text{fn} \left(\frac{L}{D_h}, Y, x_o, p_r \right)$ $Y = \text{Pe} \cdot \text{Fr}^{0.4} \cdot (\mu_l / \mu_v)^{0.6}$
Wojtan et al. [46]	$q_c = 0.437 \cdot G \cdot h_{lv} \cdot \text{We}^{-0.24} \left(\frac{\rho_v}{\rho_l} \right)^{0.073} \left(\frac{L}{D} \right)^{-0.72}$
Zhang et al. [47]	$q_c = 0.0352 \cdot G \cdot h_{lv} \left(\text{We}_D + 0.0119 \left(\frac{L}{D_h} \right)^{2.31} \left(\frac{\rho_v}{\rho_l} \right)^{0.361} \right)^{-0.295}$ $\cdot \left(\frac{L}{D_h} \right)^{-0.311} \left(2.05 \left(\frac{\rho_v}{\rho_l} \right)^{0.170} - x_{\text{in}} \right)$

Theoretical methods

Revellin and Thome [37] proposed the first theoretical model for predicting saturated CHF in uniformly heated circular microchannel tubes. The dryout process of a liquid film in annular flow was modelled by solving the one dimensional, two phase flow conservation equations numerically. Although ideally dryout occurs when the film thickness is totally vaporized without the existence of the interfacial waves, it was assumed that interfacial waves usually observed in microchannel annular flows will trigger an early onset of dryout when the film thickness decreases to the height of the interfacial waves.

The mass, momentum and energy conservation equations as well as the Laplace-Young equation were formulated in a two phase flow control volume as illustrated in Figure 2.18. The equations were solved using the 4th order Runge-Kutta method. The ideal dryout occurs when the film thickness δ is totally vaporized when no interfacial waves are present, i.e. at $x = 1.0$. However, the existence of the interfacial waves causes the early onset of dryout when the film thickness δ decreases to the height of the interfacial waves $\Delta\delta_i$. An example of the computed liquid film profile is illustrated in Figure 2.19. To calculate the height of the interfacial waves, the following empirical formula based on the Kelvin-Helmholtz theory was proposed to predict the interfacial wave height:

$$\frac{\Delta\delta_i}{R} = 0.09 \left(\frac{u_v}{u_l} \right)^{-3/5} \left[\frac{(\rho_l - \rho_v) \cdot g \cdot \delta^2}{\sigma} \right]^{-1/5} \quad (2.3)$$

This model was successful in predicting independent data from three different laboratories for four different fluids (R113, R134a, R245fa and water). Moreover, this method has also been extended to predict CHF under hotspots [36].

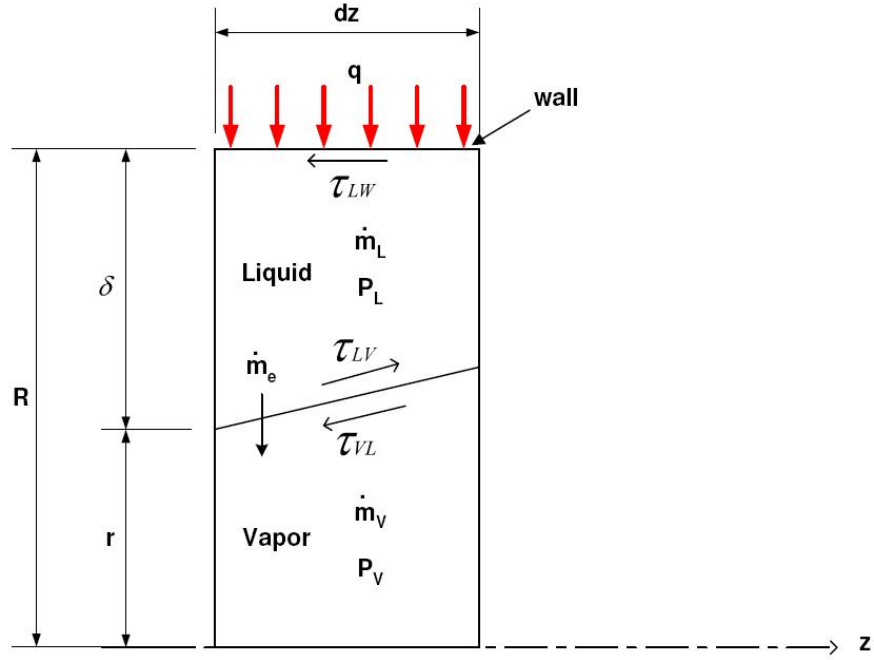


Figure 2.18: Control volume of two phase flow in annular flow regime (see Ref. [37]).

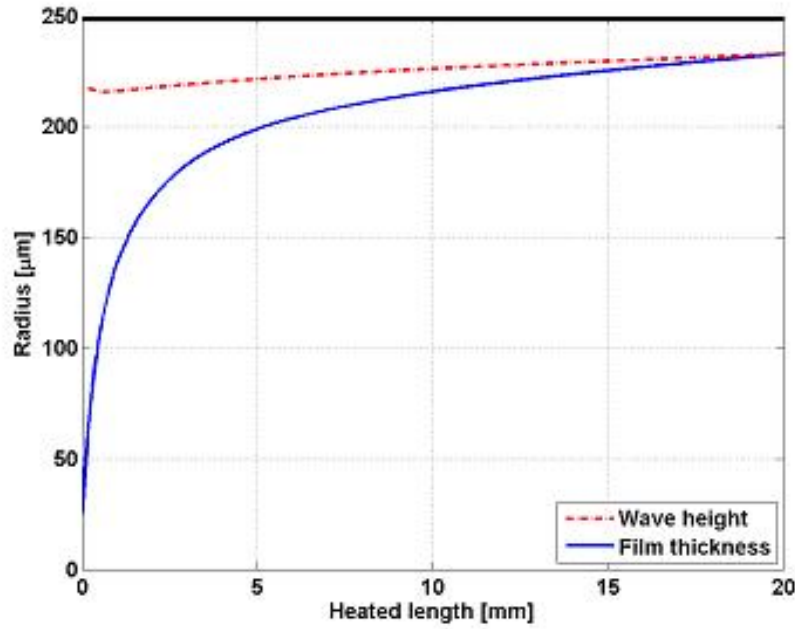


Figure 2.19: CHF model showing the annular film thickness variation along the channel plotted versus the wave height. The simulation is for R-134a at a saturation temperature of 30°C in a 0.5 mm channel of 20 mm heated length without inlet subcooling for a mass velocity of $500 \text{ kg/m}^2\text{s}$, yielding a CHF of 396 kW/m^2 (see Ref. [37]).

2.4 Summary and problem statement

In this chapter, recent studies on saturated CHF in mini/micro channels have been reviewed. This suggests several objectives for the current research:

- More CHF data at low mass velocities and low pressures for microchannel heat sinks are needed. Furthermore, the significance of understanding the basic mechanisms of CHF in microchannels should be emphasized more as opposed to simple empirical prediction methods.
- Flow instabilities were revealed to play an important role in the sudden increase of wall temperature marking the triggering of CHF. Without a sufficient inlet restriction, CHF will be induced by the flow instability in advance of the steady-state CHF. Thus, a sufficient inlet restriction should be applied for stabilizing the flow for the saturated CHF in mini/micro channels. Alternatively, the pressure drop increase imposed by the inlet restriction may be considered as a main parameter controlling flow stability to achieve the highest possible values of CHF.
- Visualization of the flow will provide a better understanding the CHF mechanisms and generate a physically based model.
- Proper treatment of uncertainty is crucial. The effect of fabrication tolerance is amplified in the micro scale. In addition to that, accurate measurements become difficult due to flow instabilities, high heat fluxes and high temperature gradients.

Therefore, the main engineering problem that this thesis tackles can be stated concisely as:

How can the CHF be accurately estimated in multi-microchannel heat sinks with low pressure refrigerants?

According to the literature review conducted here, this question has not yet been answered properly. Furthermore, the prediction methods found in the literature should be validated, since all of them were developed based on different test conditions. Discrepancies from using microchannels vs. macrochannels, rectangular vs. circular cross-section, single vs. multi-channels, water vs. refrigerants, and stable vs. unstable flow conditions need to be examined carefully. Understanding the mechanism of CHF, and estimating CHF in multi-microchannels, is crucial for the safe design of flow boiling in highly efficient cooling devices.

Therefore, in this study, flow conditions aiming at the application to the computer chip cooling have been fully investigated with three different fluids in two multi-microscale channel geometries.

Chapter 3

Experimental facility

In this chapter, the experimental test facility and data reduction methods used in this study are explained in detail. A new test loop built for CHF tests is described, including the specifications of each device. Operating procedures for CHF tests as well as the data reduction process are described. Finally, the uncertainty of each parameter and the propagation of errors in the results, such as CHF, are computed step by step.

3.1 Description of the Test Facility

A flow loop has been built to conduct the CHF experiments with relatively low pressure refrigerants. The pump and condenser were selected to provide for a wide range of experimental conditions. Two separate test sections were fabricated to investigate the effect of different channel sizes. Various types of measurement systems were used to characterize the experiments. The characteristics of each measurement are now described.

3.1.1 Flow Loop

Figure 3.1 presents a schematic diagram of the test facility constructed for this study. The fluid, circulated by an oil free micro gear pump, flows through a Coriolis mass flow meter and an electrical pre-heater before arriving at the test section. Between the pump and the mass flow meter, a reservoir is connected, where an external thermal bath controls the saturation temperature of the fluid in the reservoir to maintain the desired working pressure at the junction. Therefore, the fluid pressure or its corresponding saturation temperature at the inlet, which is far downstream from the junction, can be decided by the combination of the reservoir pressure and the mass flow rate. The volume of the reservoir is large enough to take back all the fluid when the facility is at rest. At the outlet of the test section, a plate heat exchanger condenses the evaporated refrigerant. Then, the fluid goes back to the pump, thus closing the loop. K type thermocouples, pressure transducers, sight glasses, and gas detectors were installed at several locations to monitor changes of parameters inside the loop. High pressure safety valves, a micro-filter and a degassing valve were employed for maintaining safe operation. The bypass was not used in the present test. The test facility is fully automated through a PC using Labview and a National Instruments data acquisition system. The model name and specification of the main components are summarized in Table 3.1.

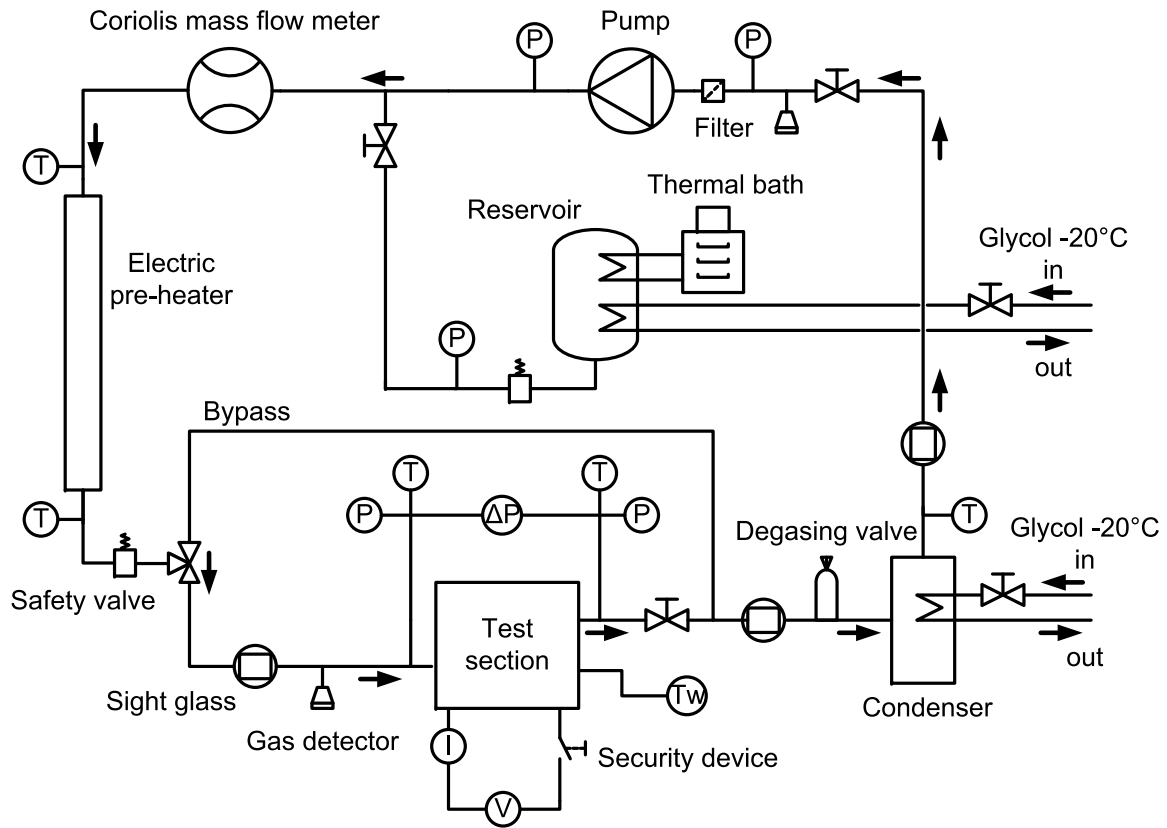


Figure 3.1: A schematic diagram of the test facility for CHF measurement.

Pump A 9 mm magnetic drive gear pump from the Diener Precision Pump company was used. This pump has two input voltages: One (24 DC Volts) for the main power and the other for controlling the rotational speed of the motor. This pump was able to provide a flow rate of 0.7 l/min with a pressure difference of 2 bar at a motor speed of 1500 rpm. This was a sufficient flow rate to keep the vapor quality below 0.8 at 300 W/cm² in the current test loop. The two input voltages were provided by a Hameg power supply.

Preheater Joule heating of an electric resistance circuit was used to set the fluid temperature before the inlet of the test section. Coils were wound around the preheater section which is 80 cm long and insulated on its external surface. The heating power was provided by a Sorensen DLM 150-7 power supply.

Condenser A plate condenser from Alfa Laval was used with glycol at - 20°C. The temperature of the glycol was maintained with a fluctuation of less than 0.5°C over a time period of 30 minutes. This fluctuation was small enough to maintain a steady flow condition at the inlet of the test section. Moreover, the mass flow rate of the glycol could be adjusted by a manual valve to control the condensing load.

Reservoir The volume of the reservoir was designed to contain around 4 kg of refrigerant in its liquid phase at room temperature. The temperature of the refrigerant inside the reservoir was controlled by water-glycol circulated by an external thermal bath.

Table 3.1: List of loop elements

Device type	Manufacturer and Model name	Description
Pump	Diener, 9mm magnetic drive gear pump	0.7 l/min @ 2 bar, 1500 rpm
Preheater	ATSE-LTCM	Coil resistance
Test section	ATSE-LTCM	Copper, milling and electric erosion
Condenser	Alfa Laval, CB26-40H	Brazed plate heat exchanger
Reservoir	ATSE-LTCM	Diameter 17 cm, Volume 347.3 ccm
Thermal bath	Lauda, Proline RP855C	Thermostat
Power supply	Hansmeg, HM8142	2 outputs for pump control
Power supply	Sorensen, DLM150-7	1 kW for preheater
Power supply	Sorensen, DLM300-10	3 kW for heater
Power supply	APC, Backups RS500	Stable power supply for PC

Refrigerant Three different refrigerants were tested: R134a, R236fa, and R245fa. Among them, R134fa has the highest saturation pressure at the same temperature. R245fa (1,1,1,3,3-pentafluoropropane) is a new type of environment friendly refrigerant, which is nonflammable and has a normal boiling point slightly below room temperature. Low saturation temperature and low saturation pressure refrigerants are generally preferred for consumer electronic cooling applications.

3.1.2 Test section

Two heat sinks with different channel geometries were fabricated in copper by electro-erosion and milling machining. One had 20 parallel rectangular microchannels of $467 \times 4052 \mu\text{m}$ (width \times depth) with a 0.55 mm wall thickness between each channel. The other had 29 channels of $199 \times 756 \mu\text{m}$ (width \times depth) with a 0.5 mm wall thickness between each channel. The microchannels are 30 mm long in the flow direction, with a surface roughness of $1 \mu\text{m}$ measured by a profilometry. Figure 3.2 shows the top view of the $H = 756 \mu\text{m}$ microchannel heat sink. On the bottom of each heat sink, 10 straight grooves of $300 \mu\text{m}$ depth were machined perpendicular to the flow direction, with their tips equally spaced along the heated length of the middle channel. Calibrated K type thermocouples, with a $250 \mu\text{m}$ diameter, were inserted in each groove and fixed with tin soldering to minimize contact resistance as shown in Figure 3.3. The location of the wall temperature measurement can be found in Figure 3.4.

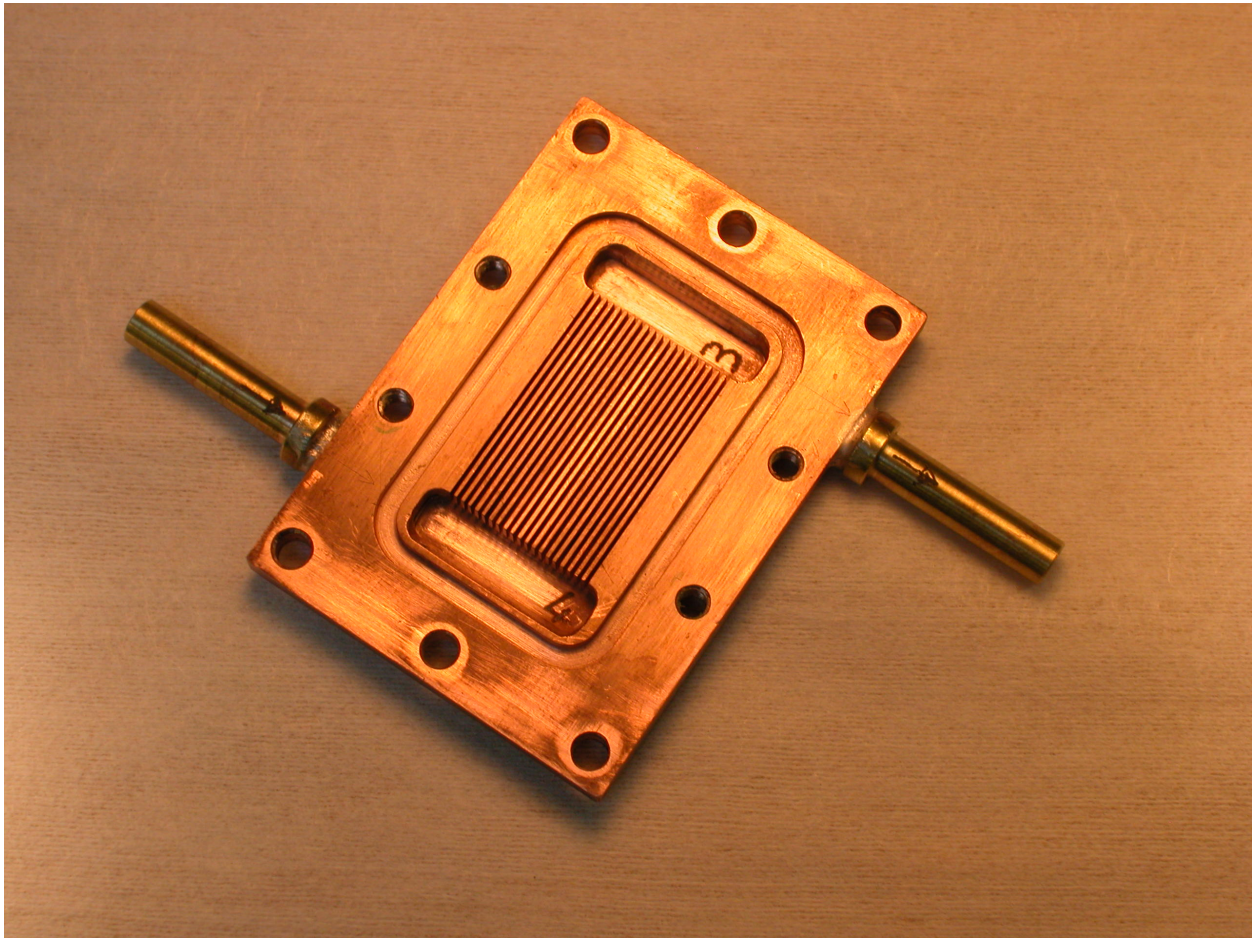


Figure 3.2: The top view of the $H = 756 \mu\text{m}$ microchannel heat sink.

Figure 3.5 shows an exploded view of the test section. On the top of the heat sink with deep channels, a glass plate with O-ring sealing was used for visualization; while for the other heat sink, a machined transparent cover that fitted on the top of the lowered fin height was made from lexan. On the bottom of the heat sink, a heater on a PCB (printed circuit board), shown in Figure 3.6 (a), was attached with indium as a thermal interface material. The indium has a thermal conductivity of 86 W/mK at 85°C . To build a firm support

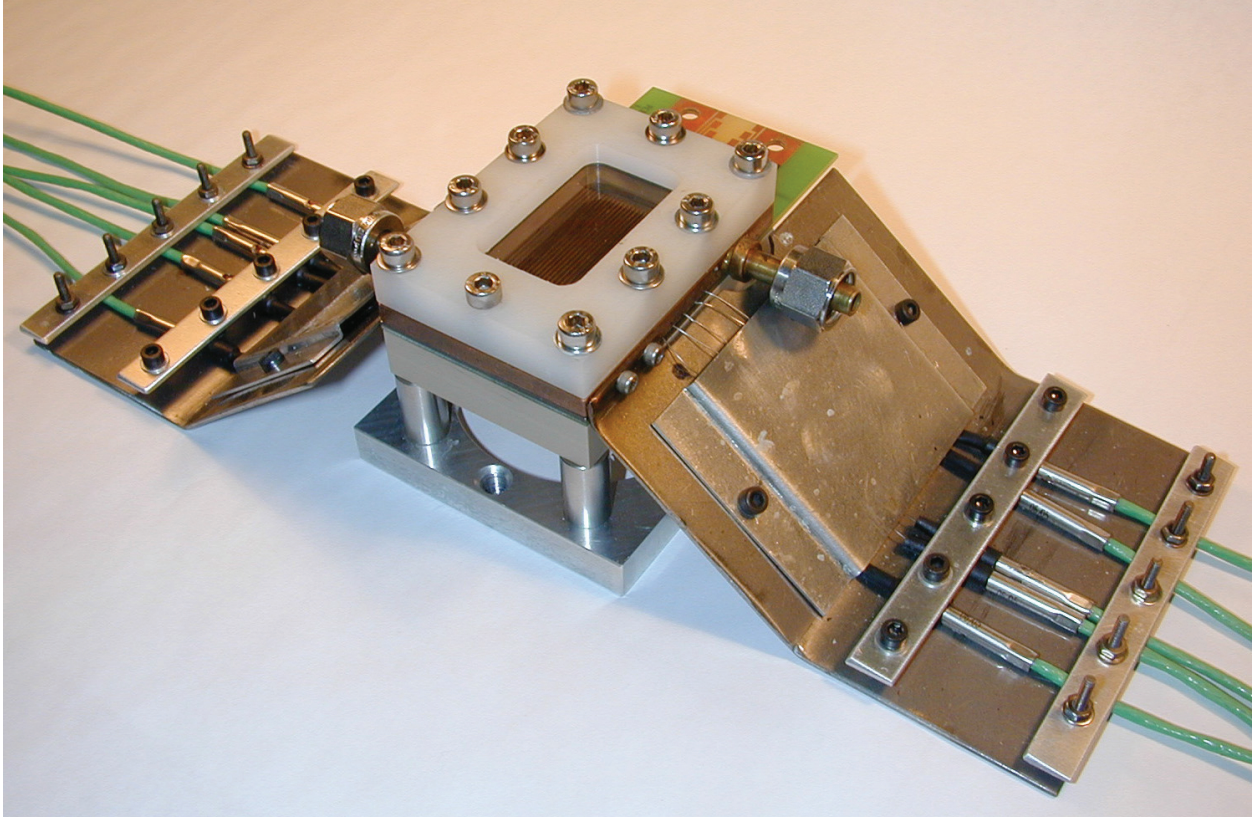


Figure 3.3: Test section for CHF measurement with ten micro-thermocouples.

and facilitate the assembly, a metal plate of $700\ \mu\text{m}$ thickness and a PEEK (Polyetheretherketone) plate with a melting point of 250°C were bolted together with the PCB and heat sink.

The electric heater, shown in Figure 3.6 (a) was fabricated and provided by the IBM Zurich Research Laboratory, a collaborating partner in this research. The heater has an electrical resistance of about $25\ \Omega$ at an ambient temperature and consists of layers of $2\ \mu\text{m}$ SiO_2 , $10\ \text{nm}$ Ti, $160\ \text{nm}$ Ni and $15\ \text{nm}$ Au, deposited on a silicon chip of $725\ \mu\text{m}$ thickness. The heating area is $2\ \text{cm} \times 2\ \text{cm}$, and is located $0.5\ \text{cm}$ from the entrance of the microchannels and spanning their width as shown in Figure 3.4.

An insert with an orifice at the entrance of each microchannel was used to suppress back flow, create a stable flow, and obtain a uniform flow distribution. Moreover, the pressure drop across this orifice slightly flashed the liquid, which had the benefit of jump-starting the boiling process. Therefore, the inlet flow may enter the channel as two-phase mixture when inlet flow has a very low subcooling. This flashing effect through the orifice has an advantage of reducing the overshoot of wall temperature for onset of boiling as well as providing spatially a more uniform wall temperature distribution. For microchannels of $H = 4052\ \mu\text{m}$, the orifices were circular holes of $300\ \mu\text{m}$ diameter drilled into a copper insert that fitted into the inlet plenum, as shown in Figure 3.6 (b). For the microchannels of $H = 756\ \mu\text{m}$, a rectangular slit of $200\ \mu\text{m}$ high was used, as shown in Figure 3.6 (c), to form a rectangular orifice at each channel inlet. Thus, the orifices formed were at the bottom of each microchannel to increase their effectiveness.

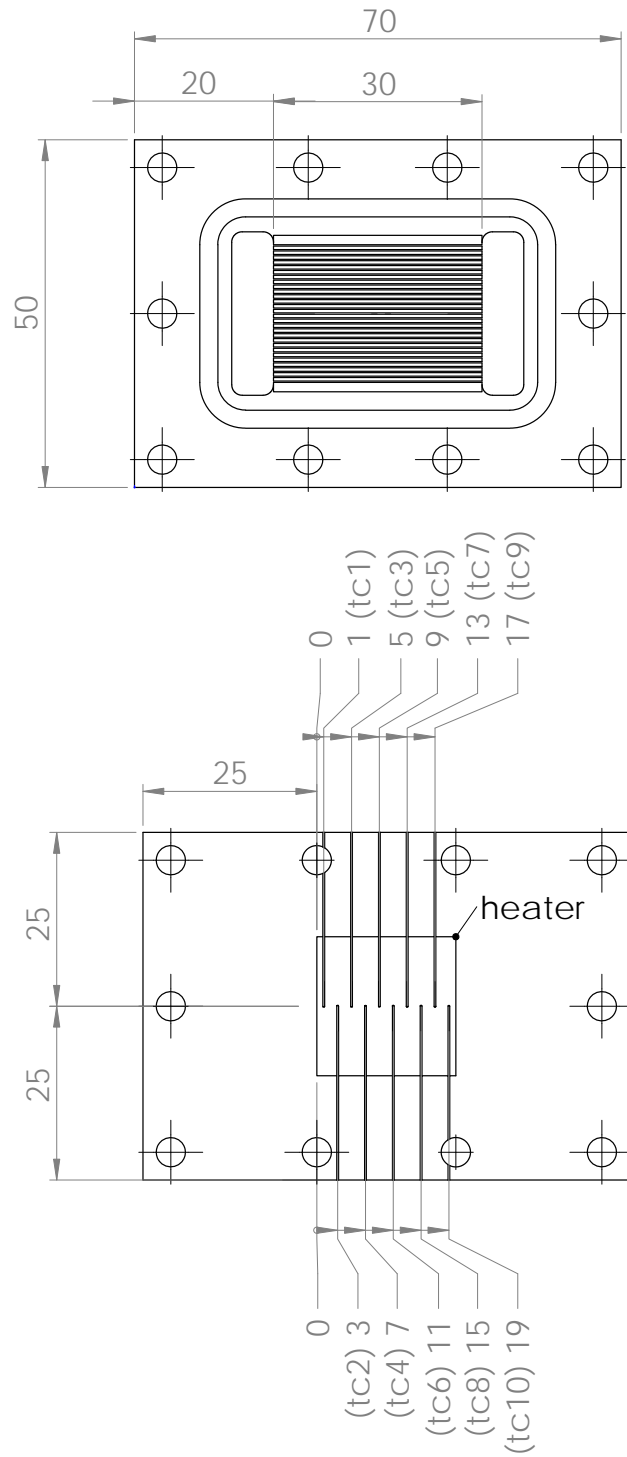


Figure 3.4: The top and bottom view of the test section. The location of each thermocouple is shown with its index in parenthesis (unit: mm). Flow direction is from left to right.

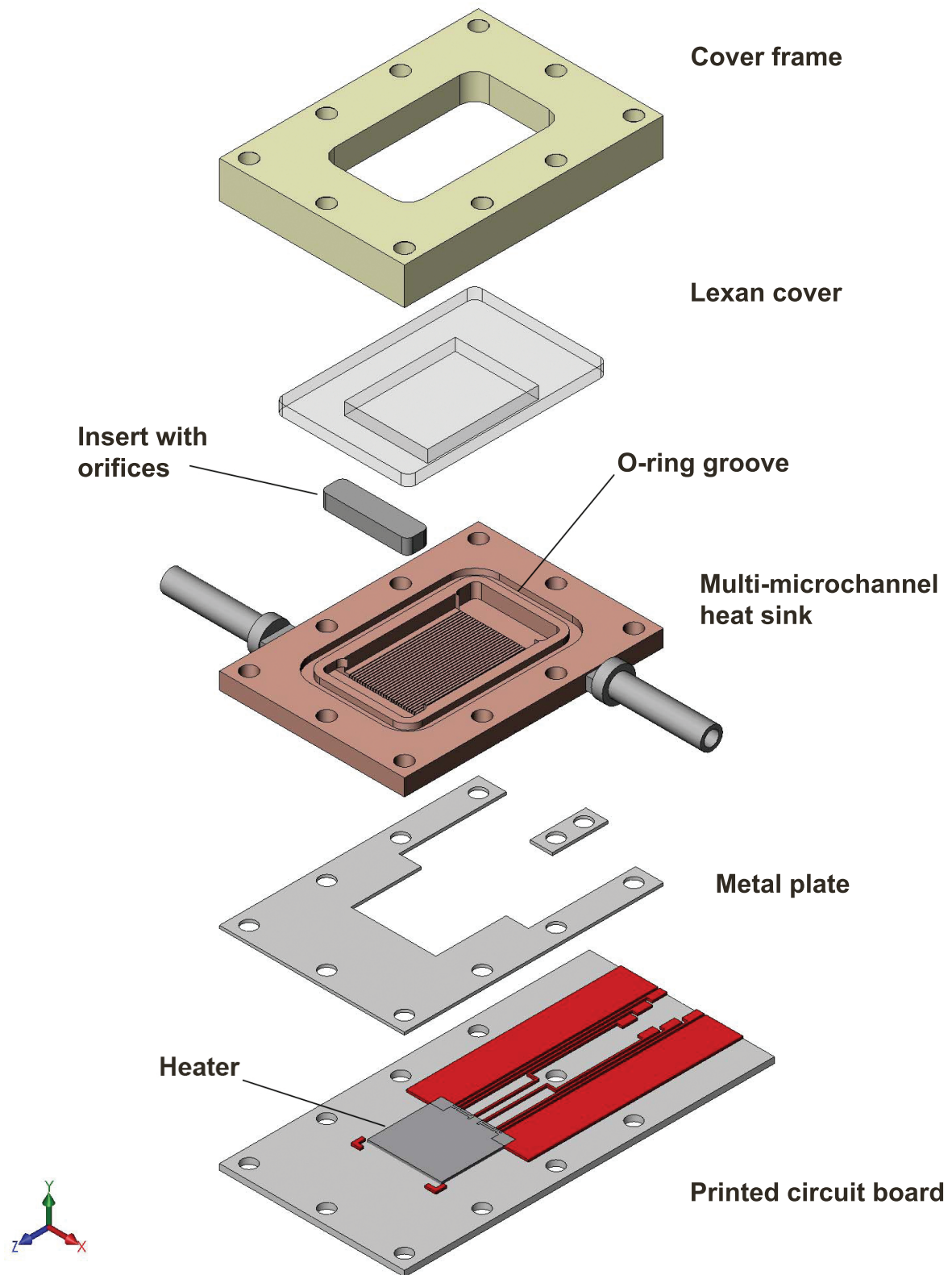


Figure 3.5: Test section assembly.

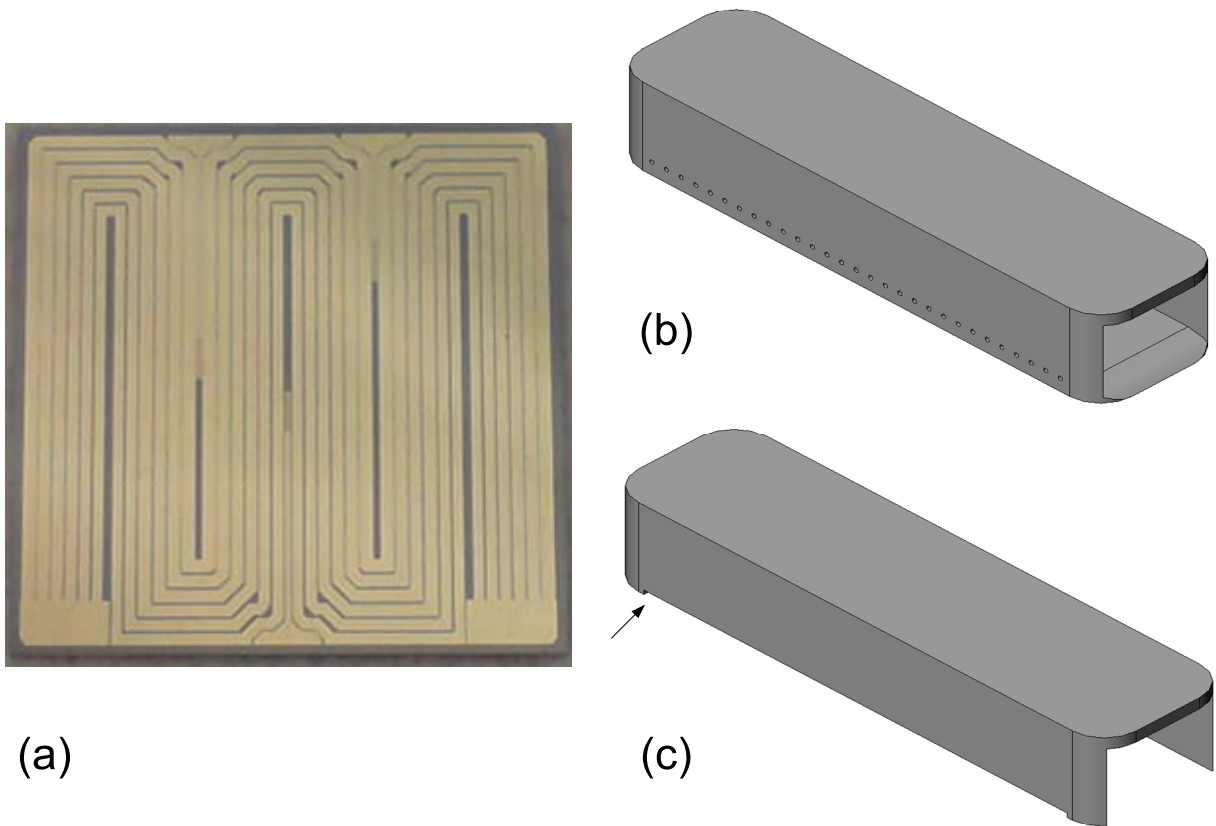


Figure 3.6: (a) serpentine heater deposited on a silicon substrate, (b) circular hole type orifice for $H = 4052 \mu\text{m}$ channels, and (c) slot type orifice for $H = 756 \mu\text{m}$ channels.

3.1.3 Measurement system

All of the measurement systems were calibrated either on site or before purchase by the manufacturer. The model name and specification of each measurement system are summarized in Table 3.2.

Temperature K type thermocouples from Thermocoax were used in this study. Stainless steel sheathed thermocouples of 500 μm diameter were used for the fluid temperature, while thermocouples of 250 μm diameter were used for wall temperature measurement in the test section. They were calibrated by a platinum thermometer system, ATP-4200, from Omega. By comparing measurements from the thermometer and thermocouples in a thermal bath at different temperatures, a correlating equation was made between the two measurements. This correlation was implemented with Labview software to correct the values from the thermocouples. The calibration was conducted after connecting the thermocouples to the data acquisition cards, using the same monitoring software with the same averaging and filtering settings, to avoid any discrepancy with the real experiments. Even though platinum thermometers of 0.03°C uncertainty were used to calibrate the thermocouples, the uncertainty of the inlet flow temperature was estimated to be 0.1 K considering a spatial variation inside the tube and ambient effect.

Pressure Two absolute pressure sensors with a maximum range of 10 bar and a differential pressure sensor with a maximum range of 500 mbar were installed at the inlet and outlet of the test section. Pressure drops could thus be measured either by subtracting the two absolute pressures or by the differential pressure sensor. When the pressure drop was less than 500 mbar, the value from the differential pressure sensor was chosen, while for the higher pressure drop, the value from the two absolute pressure sensors was used. The absolute pressure gages were calibrated with an oil balance Industrial Dead-weight Tester from Barnet Instruments Ltd. The differential pressure gauges were calibrated with ethanol columns. All the pressure gages were calibrated after being connected to the data acquisition cards using the same data correcting procedures found in the real experiments. The absolute pressure transducer has an accuracy up to $\pm 0.075\%$ of full scale, thus ± 7.5 mbar while the differential pressure transducer was accurate to $\pm 0.075\%$ of full scale, thus ± 0.4 mbar. However, considering a mounting effect as well as the tube connection from the actual location and the gage, 10 mbar was considered for its uncertainty. Comparison between the measurement of the absolute pressure gage and that of the differential pressure gage confirmed the validity of 10 mbar error estimation.

Mass flow rate A Coriolis mass flow meter from Emerson was installed upstream of the pre-heater. The maximum flow rate of this mass flow meter was 108 kg/hr and stable operation was checked both with water and refrigerant. The meter was accurate to $\pm 0.1\%$ of the readings.

Voltage and current measurement Voltage and current could be read from the power supply. However, to eliminate the voltage drop in the connecting cables at high power, the voltage was also measured at the test section with an SCXI 1327 data acquisition card from the National Instruments. The current measurement from the power supply has an uncertainty of 0.09 A (0.75% of $I_{\text{max}} + 1$ count) while the voltage measurement from the NI data acquisition card is 0.06% of the value, i.e. maximum 0.18 V for 300 V. They yield less than 0.02 W for the uncertainty of the power input measurement.

Data acquisition card and PC communication A data acquisition device from the National Instrument was used to gather information from each sensor. To avoid the electrical noise of the 50Hz AC power, 100 samples at 5000 Hz, taken in a 0.02 second period, were gathered and averaged to produce one data point.

High speed video camera The digital camera used to record the boiling process in the test section, a Fastcam-ultima APX from Photron, has a minimum shutter speed of $1/250'000$ s and a maximum recording speed of 120'000 frames per second at a resolution of 128 x 16. Lowering the recording speed enables a higher resolution up to 1024 x 1024. The optical lens is interchangeable to increase magnification. Camera settings, such as the shutter speed and aperture, were chosen considering the rate of change of the phenomena, the amount of the light available, and the depth of field. Several light sources were tested to improve the quality of the video. A halogen light source using constant voltage gave uniformly illuminated stable images over a wide area at the expense of heating up the test section. Consequently, it is unusable for low heat flux condition experiments. A long duration light source from Cordin's flash system (Model 395) enabled high speed recording over a duration of 10 ms. A normal flash system was also employed for a snapshot photography of certain flow conditions.

Table 3.2: Measurement system components

Device type	Manufacturer and Model name	Description
Temperature sensor	Thermocoax, K type 500 μm diameter K type 250 μm diameter	- Fluid temperature measurement - Wall temperature measurement
Pressure sensor	Endress+Hauser, Deltabar S PMD70 Cerabar S PMP71 Haenni, ED 510	- Diff. pressure, max 500 mbar - Absolute pressure, max 10 bar - Absolute pressure, max 5 bar
Signal converter	Camille Bauer, Power pack SIRAX B811-6 Backplane SIRAX BP902-181	Connected to the pressure sensor output converting current (4-20mA) to voltage (0-10V)
Mass flow meter	Emerson, Micro motion elite sensor CMF010	Max 108kg/h
Acquisition card	National Instruments, SCXI 1302 SCXI 1327 SCXI 1102 module SCXI 1125 module SCXI 1000	- 32 channels - High voltage (300 V) - Backplane - Backplane - 4 slot chassis
Calibration thermometer	Omega, ATP 4200	Platinum, 0.025°C error
High speed video camera	Photron, Fastcam-ultima APX	1024 x 1024 @ 2000 fps 128 x 16 @ 120'000 fps Min. shutter speed 1/250'000 sec

3.2 Operation and data reduction processes

This section describes the operating procedures used for running the experiments; this includes process control, data acquisition and safety procedures. The analysis of the acquired raw data will also be described.

3.2.1 Operating procedures

For each test section and refrigerant, the test matrix covered a wide range of flow conditions to investigate the effect of the following parameters on CHF: mass velocity G , inlet saturated fluid temperature T_{sat} , and inlet fluid subcooling ΔT_{sub} . Table 3.3 summarizes the test conditions. The channel with $H = 4052 \mu\text{m}$ has a hydraulic diameter of 0.84 mm based on its total wetted perimeter while the $H = 756 \mu\text{m}$ channel has a value of 0.32 mm.

As a macro-to-microscale two-phase flow transition criterion, a confinement number can be calculated as proposed by Kew and Cornwell [23]:

$$\text{Co} = \left(\frac{\sigma}{g(\rho_l - \rho_v)D} \right)^{1/2} \quad (3.1)$$

They reported that the heat transfer and flow characteristics were significantly different than those observed in macrochannels for $\text{Co} > 0.5$. In this experimental campaign, the confinement number ranged from 1.0 to 1.3 for the channel with $H = 4052 \mu\text{m}$ and from 2.6 to 3.4 for the channel with $H = 756 \mu\text{m}$, thus classifying the test conditions as a microscale.

Table 3.3: Range of test conditions

Channel geometry $W \times H (\mu\text{m})$	Fluid	Saturation temperature (°C)	Mass velocity (kg/m ² s)	Inlet subcooling (K)	Re $\left(\frac{GD_h}{\mu_l} \right)$
467×4052	R245fa	25-50	90-230	0-24	170-600
	R236fa	20-35	100-300	3-20	220-900
	R134a	10-30	100-450	3-20	310-1600
199×756	R245fa	25-50	200-2400	0-15	140-2200
	R236fa	15-40	200-3000	0-15	190-3300
	R134a	15-25	200-4000	0-15	280-5700

In the present study, mass velocity is defined and reported as the mass flow rate per flow area, i.e. with respect to the total cross sectional area of the channels. The inlet pressure is measured upstream of the

test section and used to calculate its saturation temperature with the NIST REFPROP software (version 8). At that location, the fluid temperature is also measured and subtracted from the saturation temperature to obtain the subcooling.

All of the parameters are controlled and monitored by the computer and the interface program made in Labview. By controlling the pump speed, the mass velocity G could be adjusted. The pressure inside the reservoir is controlled by the temperature of the water circulating from the thermal bath. Since the reservoir is connected to the loop with a T junction, the fluid pressure at this junction is maintained at the same level. Therefore, the fluid pressure (or its corresponding saturation temperature T_{sat}) at the inlet, which is far downstream from the junction, can be decided by the combination of the reservoir pressure and mass velocity. The fluid is heated up to the desired subcooling, ΔT_{sub} , by the pre-heater before reaching to the test section.

A Proportional-Integral-Derivative (PID) algorithm was implemented in the Labview program to assist the control of the operating parameters. A PID controller is a robust and simple feedback algorithm that is widely used in industrial control applications [14]. Since flow boiling often accompanies sudden changes of parameters and nonlinear behaviors, the gain coefficients as well as the output range of the PID controller were adjusted carefully depending on the flow conditions. However, in the unsettled flow conditions near to CHF, the PID functions were turned off to avoid any amplification of the fluctuations.

The experiments began at a high heat flux, typically at about 50-70% of the expected CHF. After achieving the desired flow condition at that heat flux, the heat input was increased in small steps. When the wall temperature rose over a certain limit, the heat input was cut off to avoid burnout of the test section (i.e. to avoid damaging the heater). Two separate security systems were employed. One was an electric circuit working independently. Since the resistance of the heater varies with its temperature, the device checks the resistance and turned the power supply off at a preset limit. The other was a checking algorithm implemented in the interface of the Labview program. When the wall temperature surpassed 110°C, the power input to the heater was cut. This limit was chosen based on the melting point of the interface material between the heater and the test section, as well as trial and error experience. Utilizing both of these security systems, the CHF tests were safely and successfully conducted.

Unlike other flow boiling tests for measuring pressure drop or heat transfer coefficient, CHF is measured at the moment it occurs while increasing heat flux. Therefore, averaging data over a time period at a steady state condition is not feasible in CHF tests. In this study, the average of 100 data acquired at 5000 Hz, taken in a 0.02 second period, is used as a single data point. By enabling communication between the PC and the data acquisition cards, three to four data points per a second could be recorded continuously into a spread sheet. Instead of saving one single data point at CHF, this continuous record at each flow condition was stored for further analysis. Furthermore, when steady state values were required, an average of these data points and their standard deviation was recorded into a separated spread sheet. For certain conditions, high frequency data, such as continuous data at a frequency of 1000 Hz for 3 seconds, has been gathered. In addition, the high speed camera was used to record the flow patterns found in the channels for some conditions at high heat fluxes.

3.2.2 Data reduction for wall heat flux, q_w

In this section, details of the data reduction procedures are given. Starting with the measured base heat flux, the wall heat flux on the channel wall based on the effective area (including the fin efficiency effect) must be calculated to reduce the data to general terms and compare with prediction methods found in the literature. The procedures were coded in a Matlab software and were also used to calculate the propagation of errors in the results. Schematic diagrams for local property variation and wall heat flux are presented in Figure 3.7 to help understanding of the process.

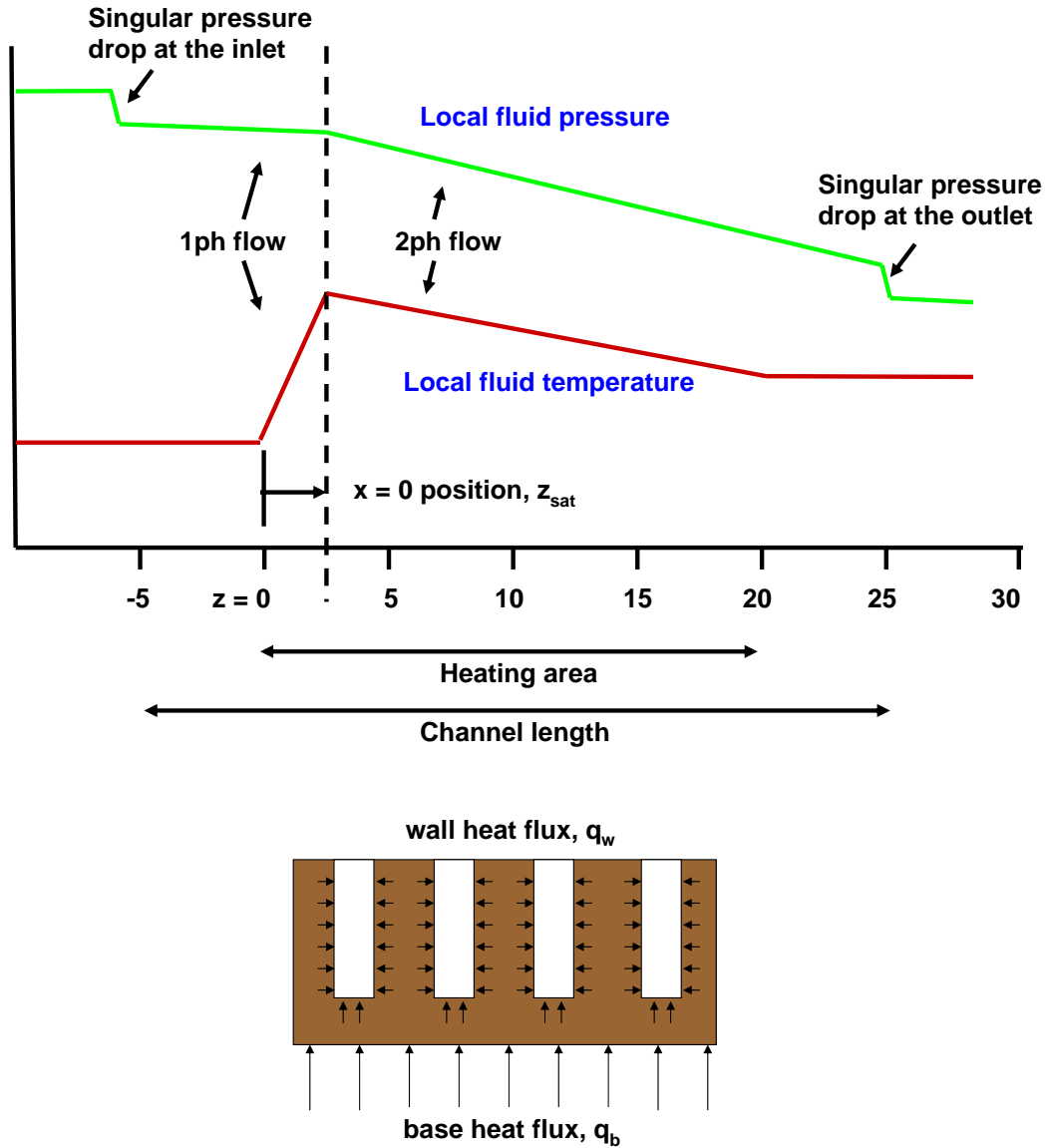


Figure 3.7: Schematic of local property variation and wall heat flux.

Here, the mass quality, x is defined as

$$x = \frac{\dot{M}_v}{\dot{M}_v + \dot{M}_l} \quad (3.2)$$

When both liquid and vapor phases are in thermodynamic equilibrium, then an alternative definition of mass quality x can be given based on thermodynamic properties:

$$x = \frac{h - h_l}{h_{lv}} \quad (3.3)$$

In the following procedures, the vapor quality x refers to this thermodynamic vapor quality, thus can have a negative value depending on the conditions.

The processing steps are as follows:

1. Find the position at which the vapor quality x is 0 in the channels:
 - (a) Assume a saturation temperature, T_{sat} at a channel position.
 - (b) Calculate a single phase flow length from the energy balance from:

$$Q \frac{z_{\text{sat}}}{L_h} = \dot{M} \cdot \overline{c_{pl}} \cdot (T_{\text{sat}} - T_{\text{in}}) \quad (3.4)$$

where

$$\overline{c_{pl}} = c_{pl}(\overline{T}) \quad (3.5)$$

$$\overline{T} = \frac{T_{\text{sat}} + T_{\text{in}}}{2} \quad (3.6)$$

Q is the total power input; z_{sat} is the distance from the front edge of the heater to the $x = 0$ position; L_h is the total length of the heated area; \dot{M} is mass flow rate; c_{pl} is the liquid specific heat; T_{in} is the measured inlet temperature.

- (c) Calculate the pressure, p_{sat} at this position from the single phase pressure drop:

$$p_{\text{sat}} = p_{\text{in}} - \Delta p_{\text{singular}} - \Delta p_{\text{fric}} \quad (3.7)$$

$$= p_{\text{in}} - \frac{\xi}{2\rho_l} G^2 - \int_{-z_{\text{in}}}^{z_{\text{sat}}} \frac{G^2}{2\rho_l} \cdot 4f \cdot \frac{dz}{D_h} \quad (3.8)$$

where ξ is a singular pressure drop coefficient which is decided by the configuration. It was calculated from a series of single phase experiments by curve-fitting the measured pressure drop data. f is the Fanning friction factor and can be found from Shah and London [40]. Since f varies with distance in a developing laminar flow, the frictional pressure drop was computed in short lengths and integrated from the inlet of the channel to the $x = 0$ position. z is the location in the flow direction from the front edge of the heater, and z_{in} is the unheated length from the inlet of the channel to the front edge of the heater.

- (d) Find the corresponding saturation temperature using the NIST REFROP software.
- (e) Iterate until T_{sat} converges.

2. Single phase local fluid property at $z < z_{\text{sat}}$:

- (a) The local fluid temperature is calculated again with the energy balance from the previous step.
- (b) The local pressure is calculated from the single phase pressure drop in the previous step.
- (c) The vapor quality is defined as the ratio of the vapor mass flow rate to the total mass flow rate. The local thermodynamic vapor quality in the single phase region has negative values to account for the subcooling. All the energy input is assumed to be absorbed by the fluid between the two positions. This vapor quality is calculated from an energy balance between the inlet and the measurement location:

$$x(z) = \frac{1}{h_{lv}} \cdot \left(\frac{z}{L_h} \cdot \frac{Q}{\dot{M}} - \overline{c}_{pl} \cdot (T_{\text{sat}}(p(z)) - T_{\text{in}}) \right) \quad (3.9)$$

where

$$h_{lv} = h_{lv}(p(z)) \quad (3.10)$$

3. Two phase local fluid property at $z > z_{\text{sat}}$:

- (a) Local fluid temperature: In the two phase region, the fluid temperature corresponds to the fluid saturation temperature at the local pressure and has been calculated using the NIST REFROP software.
- (b) Local Pressure: a linear pressure profile was assumed from the $x = 0$ position, z_{sat} to the outlet of the channel, z_o :

$$p(z) = p_o + \frac{p_{\text{sat}} - p_o}{z_{\text{sat}} - z_o} (z - z_o) \quad (3.11)$$

where p_o is the measured pressure at the outlet.

- (c) Local vapor quality: The vapor quality in the two phase region has a positive value and can be calculated from Equation 3.9.

4. Perimeter heat flux on the channel wall: q_w is the wall heat flux that is based relative to the effective wetted area, i.e. that accounting for the fin efficiency. An iteration process is required to determine q_w because the fin efficiency, effective area and wall heat flux change as the value of the local heat transfer coefficient changes. Following the notations of Figure 3.8, the process based on Incropera [17] is as follows:

- (a) Assume a fin efficiency, for example $\eta = 0.8$.
- (b) Calculate the perimeter heat flux ignoring the top glass plate that is assumed to be adiabatic:

$$q_w = \frac{q_b(W_{\text{ch}} + W_{\text{f}})}{(W_{\text{ch}} + 2\eta H_{\text{f}})} \quad (3.12)$$

where

$$q_b = \frac{V \cdot I}{A_b} \quad (3.13)$$

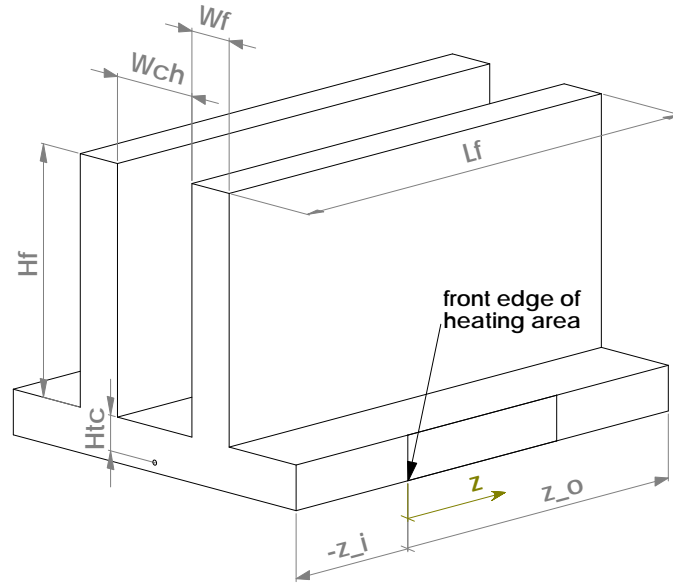


Figure 3.8: Schematic of the microchannels.

- (c) Calculate the heat transfer coefficient:

$$h = \frac{q_w}{T_w - T_{fl}} \quad (3.14)$$

where T_w is corrected from the thermocouple measurement by:

$$T_w = T_{tc} - \frac{q_b H_{tc}}{k_s} \quad (3.15)$$

For the thermal conductivity of copper, k_s , a constant value of 397 W/mK was used since it varies only 1% over the current wall temperature range.

- (d) Using 1-d heat conduction theory, the value of the fin efficiency is iterated until it converges to a fixed value, where

$$\eta = \frac{\tanh(mH_f)}{mH_f} \quad (3.16)$$

$$m^2 = \frac{hP}{k_s A_f} = \frac{h \cdot 2(W_f + L_f)}{k_s (W_f L_f)} \quad (3.17)$$

and P is the fin perimeter.

3.3 Uncertainty Analysis

Experimentation is not just pushing a start button and taking data. Lack of knowledge on the experimental uncertainty can result in poor quality data and to misleading conclusions. For example, many researchers at first erroneously concluded that conventional macro scale pressure drop theory made from macro scale research was not appropriate for micro scale channels. However, it was found later (e.g. Agostini et al. [1]) that the uncertainty of experimental parameters, such as that of channel geometry, played an important role in micro scale phenomena, which was ignored in macro scales. In this chapter, the uncertainties of our measurements and their propagation in the results have been analyzed. Since several decades, many references on uncertainty treatment have been available, such as Kline and McClintock [24], Moffat [30] [31], Coleman and Steele [11] and Taylor [42]. In this study, the ASME standard [4] provided a systematic procedure for uncertainty analysis and helped us to determine the most critical error source, thus reducing the total uncertainty. This standard is in harmony with the ISO Guide [18] even though they use different error classifications. The step-by-step calculation procedures from chapter 9 of ASME PTC-19.1 are listed below:

1. Define the Measurement Process
 - Review test objectives and test duration
 - List all independent measurement parameters and their nominal levels
 - List all calibrations and instrument setups
 - Define the functional relationship between the parameters and results
2. List the Elemental Uncertainty Sources
3. Calculate the Systematic and Random standard deviation
4. Propagate the Systematic and Random standard deviation
5. Calculate the Uncertainty

In this chapter, only the main results found from the step-by-step analysis are listed. The details of each procedure can be found in Appendix B.

3.3.1 Uncertainty of measurement

All the measurement systems were calibrated before experimentation. Table 3.4 summarizes the uncertainty components of each measured parameter for a nominal flow condition. The random error was calculated from data gathered from repeated measurements. On the other hand, the systematic uncertainty estimate is based on engineering judgement and analysis of elemental systematic errors, which include manufacturer's specifications, the uncertainty of the calibration and experimenter's experience.

3.3.2 Uncertainty of results and the main sources of error

Experimental results which cannot be measured directly are calculated from a functional relationship of the measured parameters such as temperature and pressure. In addition, some basic parameters are often

Table 3.4: Measurement uncertainty summary.

Symbol	Mean value (\bar{X})	Systematic Uncertainty ($B = [\sum_{i=1}^K b_i^2]^{\frac{1}{2}}$)	Sample Standard Deviation (S_X)	Total Uncertainty of a Measurement (U_{95})
$T_{\text{in}}(^{\circ}\text{C})$	20.1	0.1	0.005	0.1
$T_{\text{o}}(^{\circ}\text{C})$	18.5	0.1	0.044	0.2
$p_{\text{in}}(\text{bar})$	2.73	0.01	0.0001	0.01
$p_{\text{o}}(\text{bar})$	2.18	0.01	0.0006	0.01
$Q(\text{W})$	529	58.2	0.4	58.2
$\dot{M}(\text{kg/h})$	23.2	0.03	0.022	0.05
$T_{\text{w}}(^{\circ}\text{C})$	76.8	5	0.16	5.0
$A_{\text{h}}(\text{cm}^2)$	4	0.2	0	0.2
$W_{\text{ch}}(\mu\text{m})$	199	3	0	3
$H_{\text{f}}(\mu\text{m})$	756	6	0	6
$z(\text{mm})$	9	0.1	0	0.1

modified for better interpretation of the test conditions. For example, mass velocity is often reported instead of mass flow rate in internal flow experiments to include the effect of the channel size. Below are listed such parameters and their relationships to measured parameters.

Mass velocity

$$G = \frac{\dot{M}}{A_{\text{ch}}} = \frac{\dot{M}}{W_{\text{ch}} \times H_{\text{f}} \times N_{\text{ch}}} \quad (3.18)$$

where A_{ch} is the total cross sectional area of the channels.

Subcooling

$$\Delta T_{\text{sub}} = T_{\text{sat}}(p_{\text{in}}) - T_{\text{in}} \quad (3.19)$$

where the corresponding T_{sat} of p_{in} is computed with the NIST REFROP software.

Base heat flux

$$q_{\text{b}} = \frac{V \cdot I}{A_{\text{h}}} \quad (3.20)$$

where V , I , A_{h} are the voltage, the current and the area of the heater, respectively. However, the actual heat

delivered to the fluid differs from the heat input as shown in the following Chapter 4.1. This discrepancy (5%) from the heat loss was treated as an additional elemental uncertainty sources for the heating power estimation. Moreover, it was found that irrevocable dryout and actual damage of the heater occurred at heat fluxes a few percent higher than that ascribed to be CHF by the detecting method used in this study as explained in the following Chapter 5.1. Therefore, the error due to the CHF detection method was estimated marginally 10% for estimating the heating power at CHF moment.

Wall heat flux The procedures to calculate the wall heat flux in a rectangular channel include an iteration process to calculate the heat transfer coefficient and the fin efficiency, that is:

$$q_w = \frac{q_b(W_{ch} + W_f)}{(W_{ch} + 2\eta H_f)} = f(\bar{q}, \bar{\eta}) \quad (3.21)$$

where the fin efficiency, η , is replaced again with measurable basic parameters.

$$q_w = f(\bar{q}, \bar{T}_{in}, \bar{p}_{in}, \bar{p}_o, \bar{M}, \bar{T}_w) \quad (3.22)$$

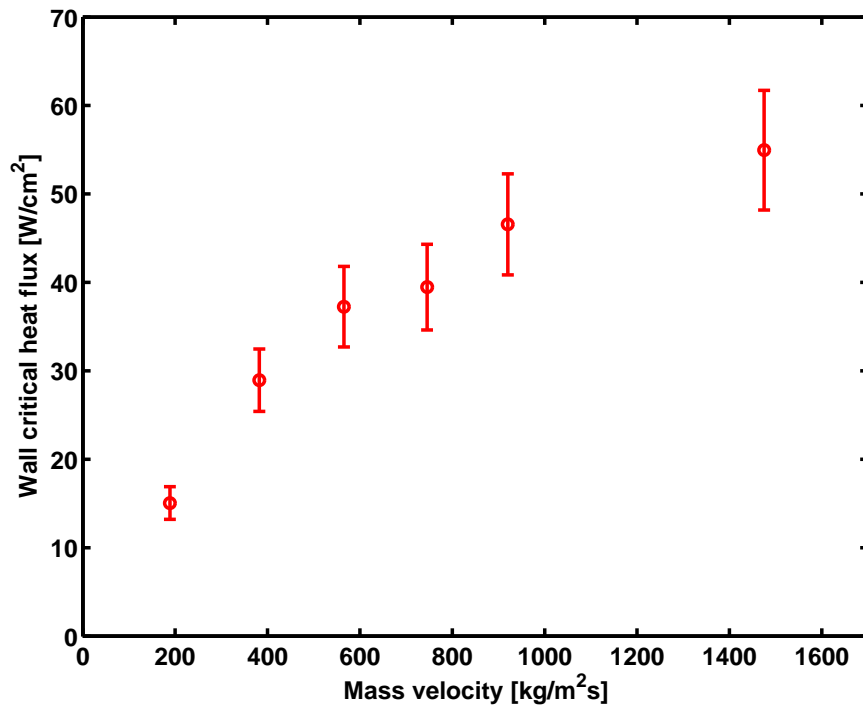
This is described in detail in Chapter 3.2.2.

To compute the propagation of the parameter errors in the results, the contribution of each parameter should be identified. This contribution can be expressed with the ratio of the change in a result to a unit change of a parameter. Comparing the amount of each contribution enables one to identify the main sources of error. In this analysis, the systematic error of heating power estimation at the moment of CHF and the systematic error of the heating area were revealed to be the main source of error for the wall CHF. Although the dimension of channel and the wall temperature measurement are known to have significant impact on the local heat transfer coefficient, the main source of error for CHF estimation was attributed to the error from the heat flux estimation. This result justifies the current measurement techniques for the measurement of CHF.

Table 3.5 summarized the total uncertainty of each result after the propagation of errors. In the current condition, the wall CHF has an uncertainty of 12% while the mass velocity and subcooling have less than 2% and 3%, respectively. Figure 3.9 shows an example of CHF results with their error bands. The flow condition was at $T_{sat} = 25^\circ\text{C}$ with R236fa in $H = 756 \mu\text{m}$ channels.

Table 3.5: Uncertainty of the results

Parameter	Mean value (\bar{X})	Systematic Uncertainty, $B_R =$ $[\sum_{i=1}^J (\theta_i B_{\bar{P}_i})^2]^{\frac{1}{2}}$	Random Uncertainty, $S_R =$ $[\sum_{i=1}^J (\theta_i S_{\bar{P}_i})^2]^{\frac{1}{2}}$	Uncertainty, U_{R95}
Local wall CHF	54.9 W/cm ²	6.8	0.04	6.8 (12%)
Mass velocity	1475 kg/m ² s	25.2	1.4	25.3 (1.7%)
Subcooling	5.02°C	0.15	0.005	0.15 (3%)

Figure 3.9: Wall CHF data for R236fa at $T_{\text{sat}} = 25^\circ\text{C}$ in $H = 756 \mu\text{m}$.

3.3.3 Additional uncertainty considerations

The propagation of the systematic uncertainty assume that the systematic uncertainties of the measured parameters are all independent of each other. If systematic errors for some of the parameters in a result are not independent, the systematic errors are said to be correlated and these nonindependent errors must be considered in the determination of the systematic uncertainty of the result.

It was revealed that the error due to the CHF detection method and the error in estimating the actual heating area were the main sources of error for the CHF estimation. However, these systematic errors for the CHF data obtained from a same method with a same facility are correlated to each other. Therefore, it is reasonable to neglect those systematic uncertainties for the relative comparison of those CHF data.

In Figure 3.10, the local wall CHF was plotted versus the mass velocity with its error band without including the systematic error due to the CHF detection method and the error in estimating the actual heating area. At $T_{\text{sat}} = 25^\circ\text{C}$ with R134a, the CHF data with a large and small subcooling are depicted for the $H = 4052 \mu\text{m}$ test section, showing some positive effect of subcooling. Figure 3.11 shows the results from the same flow conditions in the $H = 756 \mu\text{m}$ test section. In this case, the subcooling seems to have no effect on CHF.

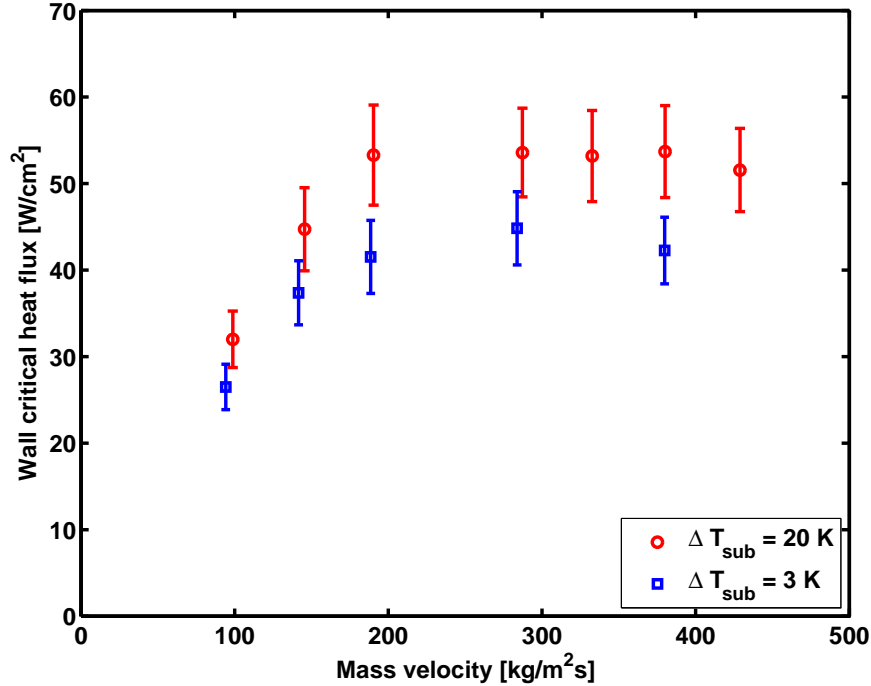


Figure 3.10: Wall CHF data for R134a at $T_{\text{sat}} = 25^\circ\text{C}$ in $H = 4052 \mu\text{m}$ ignoring the systematic error due to the CHF detection method and the error in estimating the actual heating area.

3.3.4 Conclusions

To calculate the propagation of errors in the results, the step by step procedure of ASME PTC 19.1 [4] was implemented. First of all, the uncertainty of each measurement was researched. The Coriolis mass flow meter has an uncertainty of $\pm 0.1\%$. The thermocouples and pressure transducers were calibrated with the data acquisition cards connected and have an uncertainty of $\pm 0.1^\circ\text{C}$ and $\pm 10 \text{ mbar}$, respectively. The input

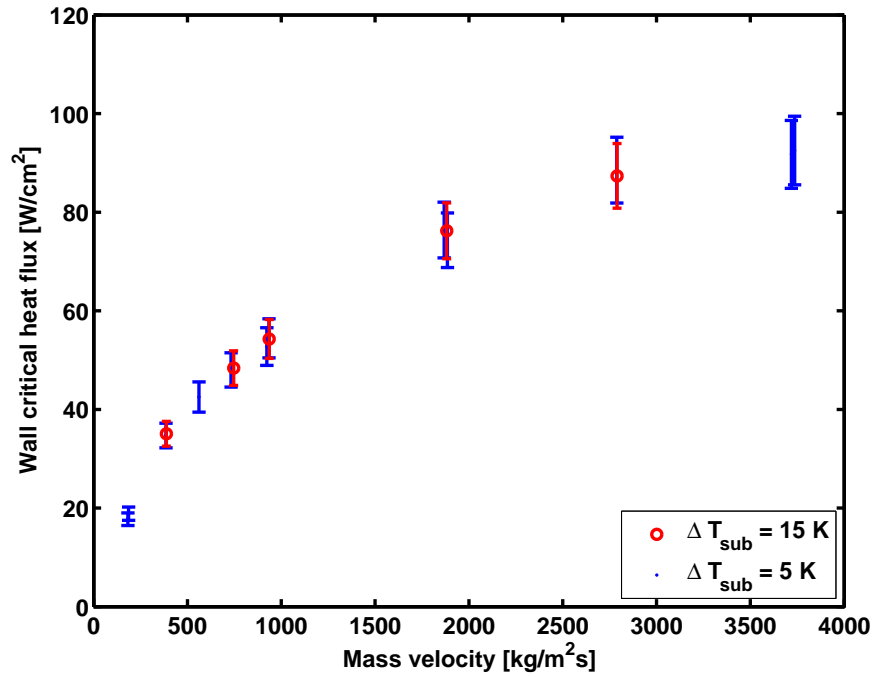


Figure 3.11: Wall CHF data for R134a at $T_{\text{sat}} = 25^\circ\text{C}$ in $H = 756 \mu\text{m}$ ignoring the systematic error due to the CHF detection method and the error in estimating the actual heating area.

heating power from the voltage and current measurement has an uncertainty of ± 0.02 W. The following uncertainty was estimated for each parameter and result: mass velocity $\pm 2\%$, inlet fluid temperature ± 0.1 K, inlet subcooling ± 0.2 K, base CHF $\pm 12\%$ and wall CHF $\pm 12\%$. The main contribution to the errors comes from the uncertainty of the heat flux estimation and the uncertainty of the geometrical dimensions of the microchannels. The main sources of the error for the heat flux estimation were revealed to be the error due to the method to determine the actual moment CHF occurs from the flow boiling curves, the heat loss to the ambient and the error in estimating the actual heating area. Therefore, from the uncertainty of wall CHF, only $\pm 5\%$ was the experimental measurement error while $\pm 10\%$ was the uncertainty of defining the point at which CHF occurs in the analysis of the boiling curve.

Chapter 4

Validation

Prior to the CHF experimental campaign, a series of preliminary tests were conducted to validate the test loop and measurement techniques. First, heat loss to the ambient was calculated for an accurate estimation of the heat flux. The energy balance between the electric heater and the single phase subcooled liquid flow was used to determine the amount of heat loss to the ambient prior to two-phase tests. Next, pressure loss through the inlet port and the orifice were calculated. By comparing with the well-known pressure drop models for single phase subcooled liquids, the contributions of the inlet port and the orifice were determined. These were again used in calculating the local pressure along the channel.

4.1 Energy Balance

To estimate heat loss to the surroundings, a series of single phase experiments were conducted with different mass velocities, heat fluxes and inlet fluid temperatures.

Objective

Most of the heat generated by the electric heater is expected to be absorbed by the flow boiling of the refrigerant in the multi-microchannels. However, a portion of the energy is inevitably conducted through the copper body of the test section and is thus eventually dissipated by natural convection to the ambient air surrounding the external surface. On the contrary, when a part of the test section is cooled below the ambient temperature, possibly by the low temperature of the highly sub-cooled fluid at the inlet, it is also possible to gain heat from the outside. Either a heat loss or gain by the test section with respect to the ambient causes the Joule heat input to differ from the actual heat delivered to the fluid. Therefore, it is important to estimate the discrepancy to see if the system is suitable for the designated CHF experiments with respect to the estimation of heat flux.

Method

In single phase flow, heat loss ΔQ can be determined by balancing the measured Joule heat input and the heat absorbed by the fluid as:

$$\Delta Q = V \cdot I - \dot{M} \cdot c_{pl} \cdot (T_o - T_{in}) \quad (4.1)$$

Since CHF occurs only at very high heat fluxes, heat loss rather than heat gain is expected to play the dominant role for the bias of the heat flux measurements. To minimize the interference of heat gain from outside, the inlet fluid temperature was set to the ambient. To improve the measurement accuracy in these single phase energy balance tests, a large temperature difference and heat flux are generally preferred. Therefore, the system pressure was set to the maximum maintainable by the system to delay any phase change at high temperatures. R245fa was used, as opposed to R134a and R236fa, since it gives a larger temperature difference over the given pressure range. The saturation temperature at the inlet was about 65°C. Then, the heat flux was increased to the maximum within the range while avoiding a phase change. When the flow temperature reached a steady state, the measurements were recorded. The same procedure was then repeated at different mass velocities and inlet temperatures.

Results and analysis

Figure 4.1 and Figure 4.2 show the heat loss ratio versus the base heat flux for each heat sink. As can be seen, the heat loss decreases with increasing heat flux and inlet fluid subcooling. The data along the curve were collected by increasing the mass velocity. Therefore, the decrease of heat loss is likely due to the enhancement of the convective heat transfer coefficient at higher mass flow rates. Since the heat transfer coefficient in two phase flow is generally much higher than that of single phase flow, less heat loss is expected during flow boiling experiments. On the other hand, when the temperature of the inlet fluid is 20°C and 10°C, the amount of the heat loss is reduced as expected due to the heat gain from ambient. Therefore, heat losses in two phase experiments were estimated to be less than 5% of the heat input.

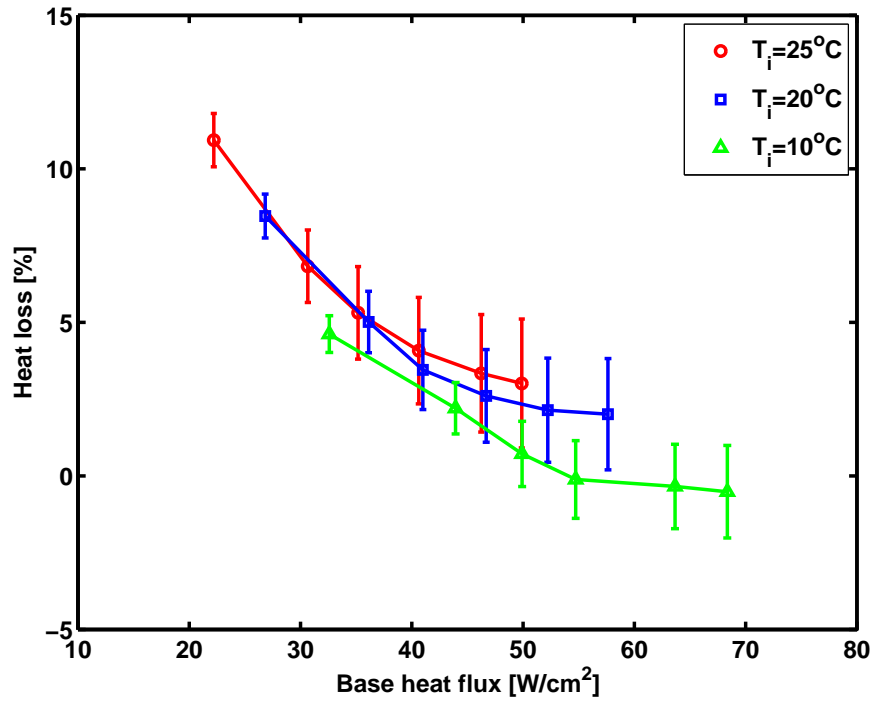


Figure 4.1: Energy loss measured in single phase experiments for R245fa in the $H = 4052 \mu\text{m}$ test section showing the error band.

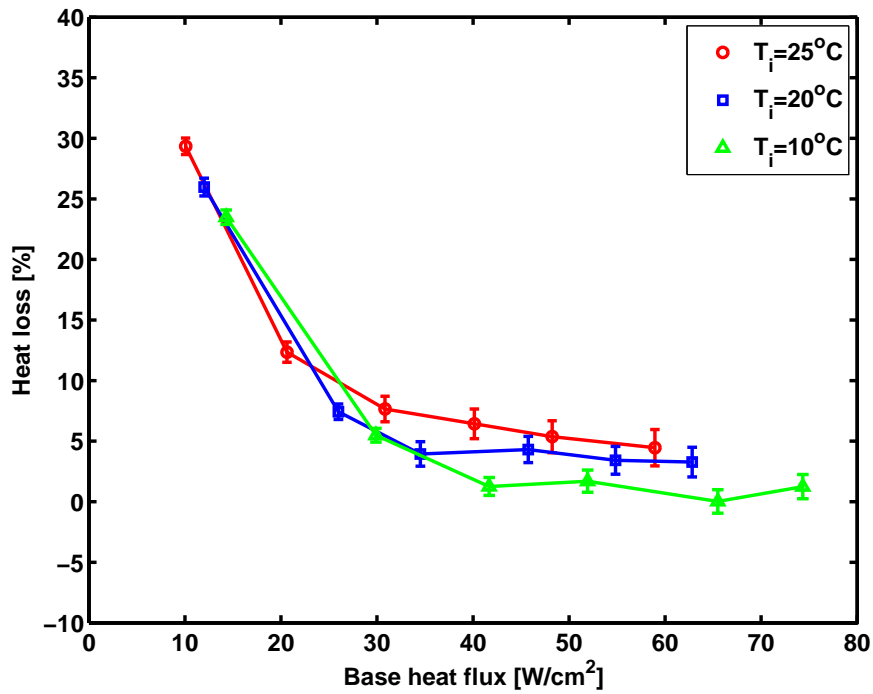


Figure 4.2: Energy loss measured in single phase experiments for R245fa in the $H = 756 \mu\text{m}$ test section showing the error band.

4.2 Single Phase Pressure Drop Measurement

Objective

To validate the pressure measurement along the test section, a series of single phase experiments were conducted and compared with theoretical predictions. In addition, the singular pressure drop across the inlet port and orifice was identified. Since the flow boiling tests use sub-cooled inlet conditions, the same singular pressure drop can be subtracted from the inlet pressure to compute the local pressure after the orifice and thus determine the local saturated fluid temperature in the channel.

Method

Due to the small size of the microchannel and the glass cover plate, the local pressure cannot be easily measured directly within the channel. Instead, it is measured upstream and downstream of the test section. Consequently, the measurement is affected by the inlet and outlet losses. Their combined loss can be expressed using the singular pressure drop coefficient, ξ , while the channel pressure drop is expressed with the Fanning friction factor, f . Therefore, the total pressure drop can be expressed by modifying the expressions in White [45] and Incropera [17] as follows:

$$\Delta p_{total} = \Delta p_{fric} + \Delta p_{singular} \quad (4.2)$$

$$\Delta p_{fric} = \frac{G^2}{2\rho_l} \cdot 4f \cdot \frac{\Delta z}{D_h} \quad (4.3)$$

$$\Delta p_{singular} = \Delta p_{in} + \Delta p_{orifice} + \Delta p_o = \frac{\xi}{2\rho_l} G^2 \quad (4.4)$$

In these expressions, G is the mass velocity, ρ_l is the refrigerant density of the liquid phase, Δz is a length in flow direction, and D_h is the hydraulic diameter of the rectangular channel. The effect of gravity is neglected due to the horizontal orientation of the channels. The Fanning friction factors were estimated by the following correlations from literature:

For turbulent flow from Blasius [45]

$$4f = 0.316 \cdot \text{Re}^{-1/4}, \text{ for } 2000 < \text{Re} < 10^5 \quad (4.5)$$

For hydrodynamic developing laminar flow from Shah and London [40]

$$f \cdot \text{Re} = 3.44(z^+)^{-0.5} + \frac{K(\infty)/(4z^+) + f_d \text{Re} - 3.44(z^+)^{-0.5}}{1 + C(z^+)^{-2}}, \text{ for } \text{Re} < 2000 \quad (4.6)$$

where, the dimensionless z^+ is defined as:

$$z^+ = z/\text{Re}D_h \quad (4.7)$$

Table 4.1: Rectangular ducts $K(\infty)$, $f_d \cdot \text{Re}$ and C to be used in Equation 4.6 from Shah and London [40]

β	$K(\infty)$	$f_d \cdot \text{Re}$	C	% error
1.00	1.43	14.227	0.00029	± 2.3
0.50	1.28	15.548	0.00021	± 1.9
0.20	0.931	19.071	0.000076	± 1.7
0.00	0.674	24.000	0.000029	± 2.4

$K(\infty)$ and f_d are the incremental pressure drop number and Fanning friction factor for fully developed flow. C is a constant dependent on the channel geometry. These constants can be interpolated from Table 4.1 while $f\text{Re}$ may be alternatively approximated by the following equation from Shah and London [40] :

$$f_d \cdot \text{Re} = 24[1 - 1.3553\beta + 1.9467\beta^2 - 1.7012\beta^3 + 0.9564\beta^4 - 0.2537\beta^5] \quad (4.8)$$

where, β is the aspect ratio ranging from 0 to 1.

On the other hand, the singular pressure loss is usually expressed as a function of the configuration and not of the flow condition. The singular pressure drop coefficient can be estimated by fitting a polynomial curve to the measured pressure drop minus the pressure drop along the channels. Alternatively, the singular pressure losses through the combination of contraction and expansion geometries can be calculated individually. From Collier and Thome [13], the pressure losses through a sudden enlargement or contraction are expressed as below:

$$\Delta p_e = (G_1)^2 \sigma (1 - \sigma) v_1 \left[1 + \left(\frac{v_{lv}}{v_1} \right) x \right] \quad (4.9)$$

$$\Delta p_c = \frac{(G_2)^2 v_1}{2} \left[\left(\frac{1}{C_c} - 1 \right)^2 + \left(1 - \frac{1}{\sigma^2} \right) \right] \left[1 + \left(\frac{v_{lv}}{v_1} \right) x \right] \quad (4.10)$$

To evaluate these expressions, a homogeneous flow condition is assumed. σ is the ratio of the cross sectional area at the upstream to that downstream. G_1 and G_2 denotes the upstream and downstream mass velocities and each of the formulae uses the mass velocity at the smaller cross sectional area. v_1 and v_v are the specific volume at the liquid and vapor state, and v_{lv} is the difference between the two states. x is the vapor quality, but in these single phase tests it was always kept at zero. The coefficient of contraction C_c is a function of σ and was interpolated from the table in Collier and Thome [13].

For our single phase pressure drop experiments, mass velocity was increased from a nominal minimum to a maximum with a constant inlet fluid temperature. No heating was used to maintain adiabatic conditions. The flow reached a steady state within a few minutes. At each condition, 60 data points were gathered and averaged. Some of the test conditions were repeated several times to prove the repeatability.

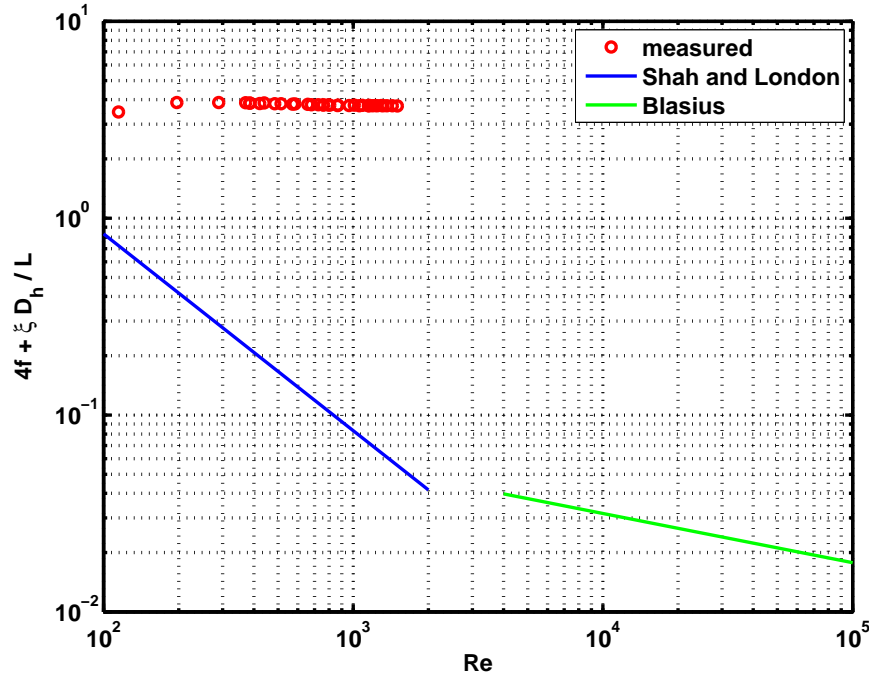


Figure 4.3: Friction factors computed from the single phase pressure drop measurements at different Reynolds numbers in the $H = 4052 \mu\text{m}$ test section without an orifice.

Results

Since the measured pressure difference is the combination of the frictional pressure drop and the singular pressure losses, it is necessary to investigate each contribution. In general, when the singular pressure losses are small compared to the frictional pressure drop, the portion of singular pressure drop is calculated individually and subtracted from the total pressure drop. This is then compared with the theoretical frictional pressure drop. On the contrary, when the portion of the singular pressure drop is larger than the frictional pressure drop, the singular loss can be determined accurately from the measurements by subtracting the frictional pressure drop estimation.

First, single phase pressure drops were measured in the test section with $H = 4052 \mu\text{m}$ channels without any restriction at the inlet. Figure 4.3 shows the friction factors calculated from the measured pressure drops assuming no singular pressure drop. The continuous curves show the predicted friction factors from Shah and London [40] for hydrodynamic developing laminar flow and Blasius [45] for fully developed turbulent flow. An order of magnitude difference implies that the singular pressure loss dominates the overall pressure drop and thus makes it possible to accurately determine the singular loss from the measurements.

Figure 4.4 shows the singular pressure drop which was calculated by subtracting the theoretical frictional pressure drop (Equation 4.3 and 4.6) from the total pressure drop. This pressure drop shows a parabolic profile with respect to the mass velocity. By fitting the curve with a second order parabolic curve, the singularity constant was computed.

Figure 4.5 shows the singular pressure drops measured with an orifice at the inlet of each channel. The difference of this pressure drop to that without the orifice is the amount of pressure loss caused by the orifice.

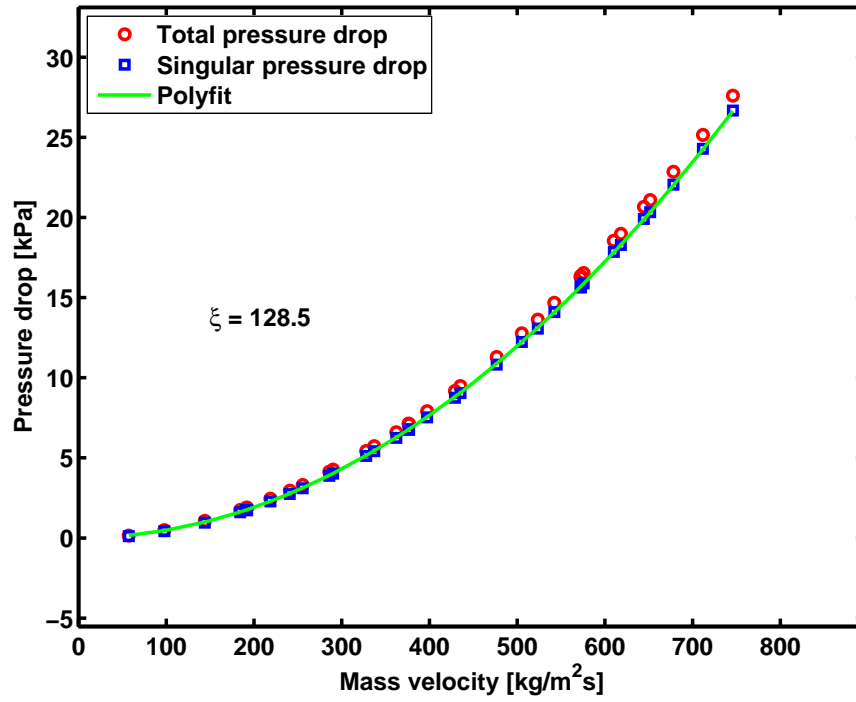


Figure 4.4: Total and singular pressure drops measured at different mass velocities at adiabatic conditions, and their second order curve fit for the singularity constant, in the $H = 4052 \mu\text{m}$ test section without an orifice.

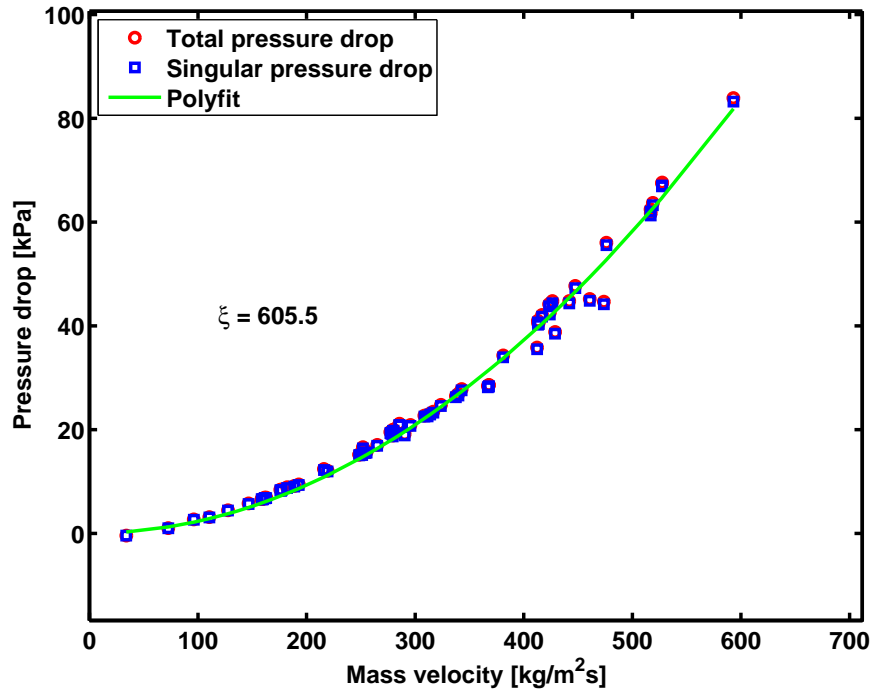


Figure 4.5: Total and singular pressure drops measured at different mass velocities at adiabatic conditions, and their second order curve fit for the singularity constant, in the $H = 4052 \mu\text{m}$ test section with a $300 \mu\text{m}$ circular orifice at the entrance of each channel.

Table 4.2 summarizes the estimated contribution of the entrance and exit geometries on the singular pressure losses. The contraction and expansion pressure drops were alternatively computed in index (6) and (7) with Equations 4.10 and 4.9. They were proved comparable with the current results, in index (4) and (5). Finally, the singular pressure drop coefficient for the combination of inlet and orifice was estimated as index (8) in the Table 4.2 to compute the local pressure after the orifice, and thus to determine the local saturated fluid temperature in the channel.

Table 4.2: Contribution of inlet and outlet configuration on the singular pressure loss coefficient in the $H = 4052 \mu\text{m}$ test section.

Estimation method	singular factors	singularity constant	index
Experiment	$\Sigma\xi_{\text{in}} + \Sigma\xi_{\text{o}}$	128.5	(1)
Experiment	$\Sigma\xi_{\text{in}} + \Sigma\xi_{\text{ori}} + \Sigma\xi_{\text{o}}$	605.5	(2)
(2) - (1)	$\Sigma\xi_{\text{ori}}$	477	(3)
(1) / 2	$\Sigma\xi_{\text{in}}$	64	(4)
(1) / 2	$\Sigma\xi_{\text{o}}$	64.5	(5)
Equation 4.10	$\Sigma\xi_{\text{in}}$	60.2	(6)
Equation 4.9	$\Sigma\xi_{\text{o}}$	64.1	(7)
(4) + (3)	$\Sigma\xi_{\text{in}} + \Sigma\xi_{\text{ori}}$	541	(8)

The same tests were repeated for the second test section of $H = 756 \mu\text{m}$. An orifice was realized by blocking the inlet of the channel except for a $200 \mu\text{m}$ height at its bottom, as shown in Figure 3.6 (c). Unlike the $H = 4052 \mu\text{m}$ channels, since the configuration of the connecting ports was improved and the hydraulic diameter of the channels was much smaller, the singular pressure drop coefficient of the inlet and outlet connectors was relatively negligible when the orifice insert was removed. Therefore, the singular pressure loss through the orifice could be estimated by determining difference in the pressure drop measurements with and without the orifice insert. Figure 4.6 shows the total pressure drop measured for the two configurations. It is noticeable that the ratio of the singular pressure drop to the frictional pressure drop ranged from near zero up to unity. The resulting singular pressure drop coefficient of the orifice was 1.8. Furthermore, by subtracting the singular pressure drop portion, the frictional pressure drop could be estimated. Figure 4.7 shows the friction factors compared with the theoretical pressure drop. The discrepancies of the data at low Reynolds number are attributed to the error of the frictional pressure drop estimation and the uncertainty at the low pressure measurements. The estimated singular pressure drop coefficient from this single phase tests will be used for the data reduction process to determine the local fluid properties in the channel.

4.3 Conclusion

Single phase energy balance tests on the two test sections showed that the heat losses at the highest base heat fluxes were less than 5%, diminishing with increasing heat flux. Since the CHF in terms of the base heat

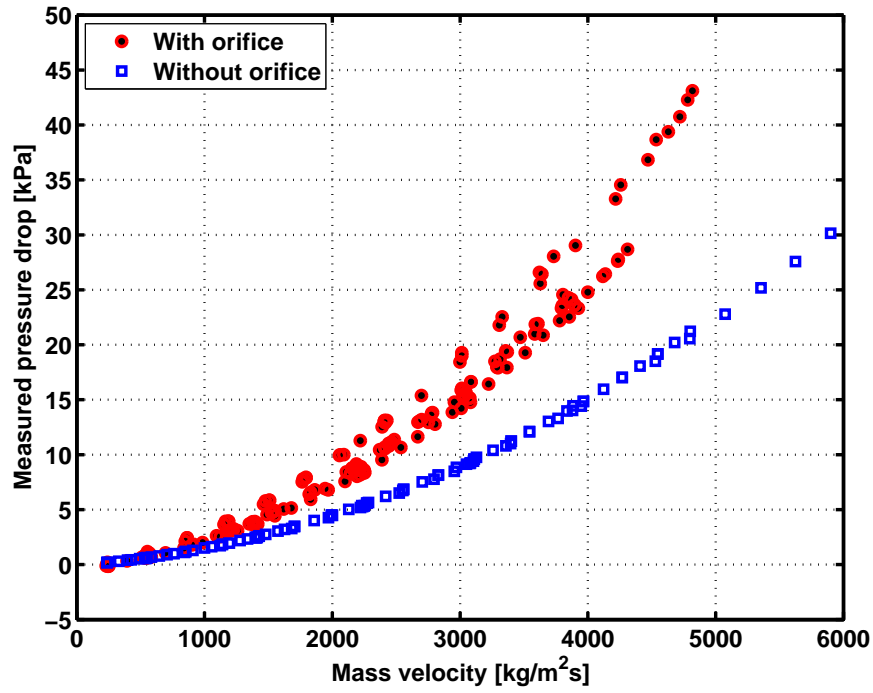


Figure 4.6: Comparison of total pressure drop in the $H = 756 \mu\text{m}$ test section with and without $200 \mu\text{m}$ rectangular slit orifices at the entrance of each channel.

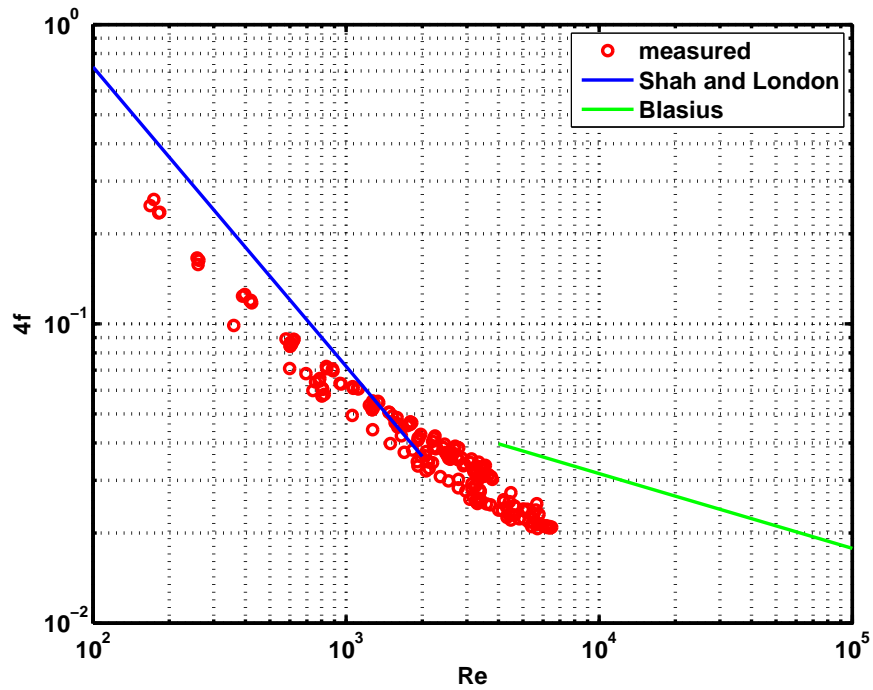


Figure 4.7: Friction factors computed from the single phase pressure drop measurements at different Reynolds numbers in the $H = 756 \mu\text{m}$ test section with $200 \mu\text{m}$ rectangular slit orifices at the entrance of each channel.

flux measured in the study ranged from about 50 to 350 W/cm², it can be concluded that the heat losses during CHF tests were always 5% or less. This was treated as an additional error term in the uncertainty of the heat flux estimation.

In addition, an investigation into the validity of the implemented pressure measurements techniques was conducted and an estimation of the singular pressure loss through the inlet port and orifice was obtained for both test sections. For the $H = 4052 \mu\text{m}$ test section, the contribution of the singular pressure drop through the inlet and outlet was much larger than the frictional pressure drop inside the microchannel. Consequently, the singular pressure drop was determined in two ways and compared to each other. In the first method, the theoretical frictional pressure drop inside the channel, determined from the Shah and London model for hydrodynamically developing flows, was subtracted from the measured pressure drop. In the second method, the contribution and expansion losses were calculated individually by considering their complex geometries. The singular pressure drops calculated from both of the methods matched very well, which reflects on the validity of the current pressure measurement methods. The contribution of the inlet configuration has been identified from the total pressure drop. For $H = 4052 \mu\text{m}$ test section, the singular pressure drop coefficient corresponding to the pressure loss through the inlet port and the $300 \mu\text{m}$ circular orifice was estimated to be 541.

On the other hand, for the $H = 756 \mu\text{m}$ test section, the singular pressure drop component was smaller than that of the frictional pressure drop, primarily since this test section had a significantly smaller hydraulic diameter than the other. Therefore, by subtracting the singular loss estimation from the measured pressure drop, the friction factors were compared with those predicted by Shah and London for the laminar flow regime and Blasius for the turbulent flow regime. The singular pressure drop coefficient for the inlet configuration was estimated to be 1.8 with the $200 \mu\text{m}$ rectangular slit orifice. These singular pressure loss coefficients were used to calculate the local pressure after the orifice and thus to determine the local saturation fluid temperature in the channel as described earlier.

Chapter 5

Experimental results

From the experimental campaign, new saturated CHF data in two multi-microchannel test sections were obtained. Three low pressure refrigerants, R134a, R236fa and R245fa, were tested in test sections of $H = 4052 \mu\text{m}$ and $756 \mu\text{m}$ with aspect ratios of 8.7 and 3.8, respectively. A large range of test conditions were tested, targeting computer chip cooling applications. All the tests were conducted with orifices at the inlet of individual channels to suppress any back flow or instabilities. Some of the conditions were repeated to check the reproducibility of the data. These repeated data fell within the uncertainty range of the data. In this chapter, the major experimental results are presented in graphs to discuss on the characteristics of the CHF data. All the database acquired in this research are available in Appendix A with their test conditions.

5.1 Flow boiling curves

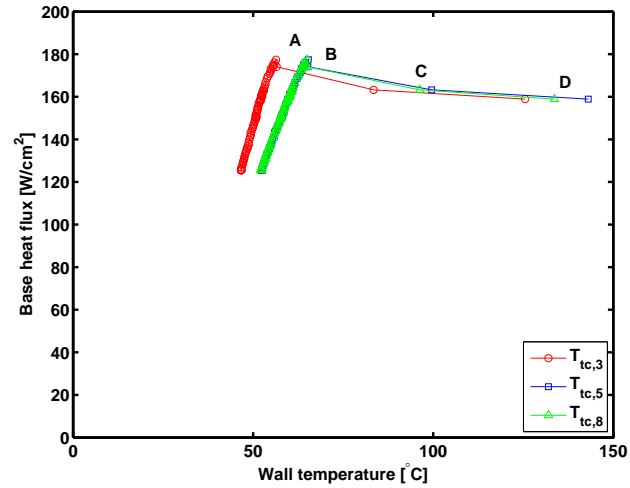
Critical heat flux is known as the heat flux at which the liquid adjacent to the heating surface is replaced by vapor and the surface temperature experiences a sharp excursion. However, detecting and defining of the actual instant CHF occurs requires a rather complicated process in actual experiments. Below, three “types” of CHF thresholds observed in the present study are described:

Figure 5.1 (a) depicts the first type of flow boiling curve found in our CHF tests. Flow conditions were kept constant at $G = 250 \text{ kg/m}^2\text{s}$, $T_{\text{sat}} = 35^\circ\text{C}$ and $\Delta T_{\text{sub}} = 10 \text{ K}$ with R236fa in $H = 4052 \mu\text{m}$ channels while the heat flux was increased in small steps. As the heating power increases, the wall temperature rises steadily until a sudden jump of the wall temperature occurs at point A. The security function cuts off the heating power when the wall temperature was detected to surpass 110°C at point D. The increase in wall temperature from around 60°C at point A to over 110°C at point D happens in less than one second. During that time, all the relevant parameters, including the local heat flux, experience a dramatic change. Table 5.1 shows the variation of each parameter when the temperature diverges. The base heat flux decreases because the electrical resistance of the heater increases as a function of its temperature while the voltage input is kept constant. That is, the Joule heating Q is equal to the multiply of the voltage and the current, and since the measured current falls while the input voltage remains constant, this decreases the value of q_b during this process. Although the base heat flux decreases less than 10%, the heat transfer coefficient decreases dramatically so that the fin efficiency after the onset of dryout increases to use more of the actual surface area for dissipating heat. Consequently, the wall heat flux based on the effective area related to the fin

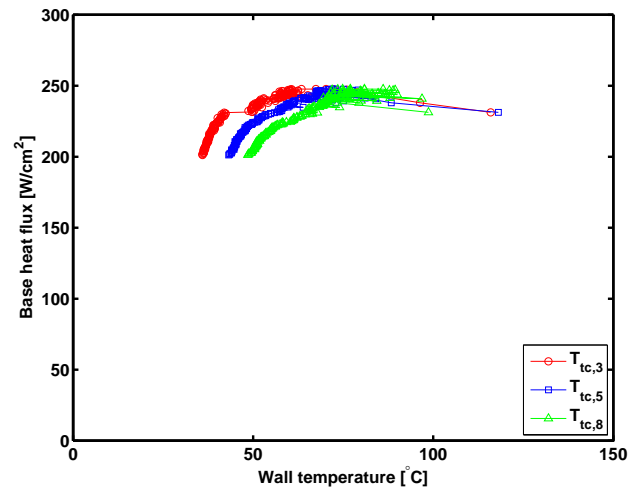
efficiency decreases to 30%. In this research, the maximum heat flux inducing a significant rise of the wall temperature, point A, was treated as the location of CHF.

Figure 5.1 (b) shows the second type of flow boiling curve acquired at $G = 150 \text{ kg/m}^2\text{s}$, $T_{\text{sat}} = 15^\circ\text{C}$ and $\Delta T_{\text{sub}} = 15 \text{ K}$ with R134a in $H = 4052 \text{ }\mu\text{m}$. During the increase of heat flux, a sudden but small jump of wall temperature happens first at 230 W/cm^2 . Since the maximum wall temperature remains below the threshold of 110°C , the heating power was maintained and the wall temperature decreases again instead of rising. Above that heat flux, sudden jumps of the wall temperature happen frequently at medium amplitudes until a distinct excursion occurs at 243 W/cm^2 . This is treated as the point of CHF here, i.e. 5% higher than the first temperature jump. Similar phenomena have been reported in Oh and Englert [32] and Kosar et al. [26], where the first observation of unstable fluctuation is treated as the Onset of Unstable Boiling (OUB).

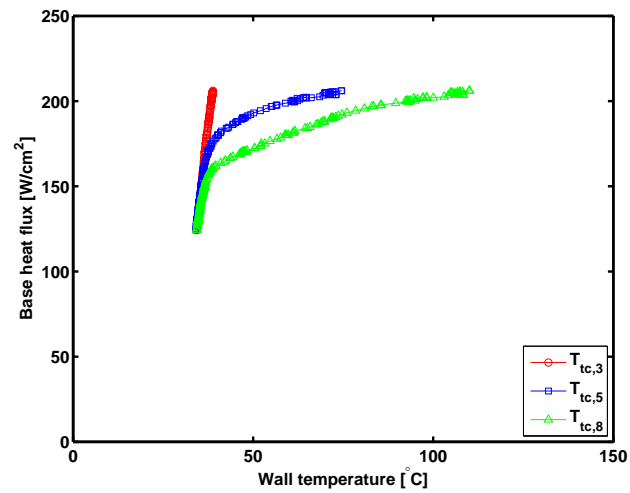
Figure 5.1 (c) shows the third type of flow boiling curve acquired at $G = 3000 \text{ kg/m}^2\text{s}$, $T_{\text{sat}} = 25^\circ\text{C}$ and $\Delta T_{\text{sub}} = 3 \text{ K}$ with R134a in $H = 756 \text{ }\mu\text{m}$. No sudden spike of wall temperature was observed. The wall temperature goes up steadily to reach the maximum limit and the power was shut off to avoid burn out of the heater. The heat transfer coefficient at the location of the eighth thermocouple was reduced significantly, indicating that partial dry out had occurred at that location. This dry out zone then grows upstream with increasing heat flux. Figure 5.2 shows the local wall temperature and corresponding heat flux at the moment of CHF at that flow condition. Therefore, although the electrical heater provides a uniform base heat flux, the local wall heat flux can vary depending on the local heat transfer coefficient, the fin efficiency at that location, and the local heater resistance. This implies also that detecting CHF by measuring temperature at one location in the middle of the channel can lead to discrepancies in the results. On the other hand, no instability is necessarily observed here. Since the threshold was determined according to the safety design of the working system rather than any physical basis of the process itself, the heat flux could be cut at less or more than the current threshold. In this study, 110°C was used to cut off the heating power during the whole experiments to be consistent and to preserve the test section. As described also in Hall and Mudawar [16], the validation of this detection method was confirmed by increasing the heat flux over the limit of 110°C . It was found that irrevocable dryout and actual damage of the heater occurred at heat fluxes only a few percent higher than that ascribed to be CHF by the current method. Thus, the measured values are expected to be within a few percent of the real CHF values, which represents incurring only a small error to save the test section from burnout.



(a) Type 1



(b) Type 2



(c) Type 3

Figure 5.1: Three types of flow boiling curve measured by the 3rd(red circle), 5th(blue square) and 8th(green triangle) thermocouples located at 5 mm, 9 mm and 15 mm downstream from the front edge of the heater, respectively (See Figure 3.4).

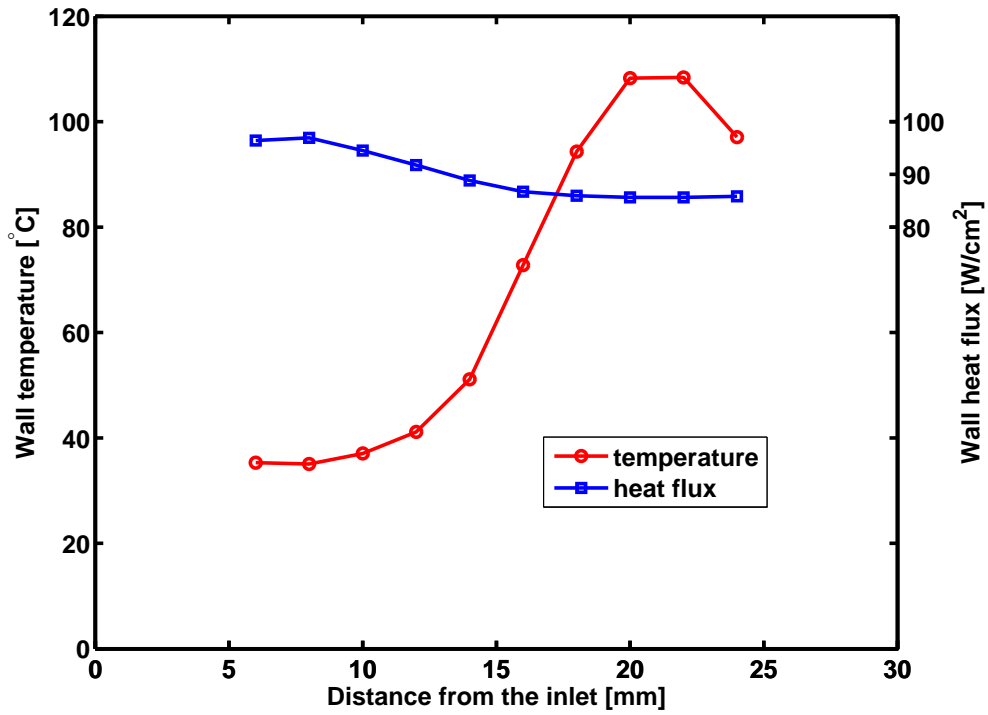


Figure 5.2: Local wall temperature and local wall heat flux at $G = 3000 \text{ kg/m}^2\text{s}$, $T_{\text{sat}} = 25 \text{ }^\circ\text{C}$, and $\Delta T_{\text{sub}} = 3 \text{ K}$ and $q_b = 206 \text{ W/cm}^2$ with R134a.

Table 5.1: Changes of parameters during the wall temperature excursion in Figure 5.1 (a)

Parameter	Units	A	B	C	D	Change (A to D)
q_b	W/cm^2	177	174	163	159	-10%
T_w	$^\circ\text{C}$	63	63	95	132	+110%
h	$\text{W/m}^2\text{K}$	9780	9560	3650	2060	-79%
η	-	0.69	0.70	0.85	0.91	+32%
q_w	W/cm^2	30	29	23	21	-30%

5.2 Effect of parameters

For each test section and refrigerant, the test matrix covered quite a wide range of flow conditions to investigate the effect of the following parameters on CHF: mass velocity G , inlet saturated fluid temperature T_{sat} , and inlet fluid subcooling ΔT_{sub} . In the present study, mass velocity is defined and reported as the mass flow rate per flow area, i.e. with respect to the total cross sectional area of the channels. The inlet pressure is measured upstream of the test section and used to calculate its saturation temperature with the NIST REFPROP software (version 8). At that location, the fluid temperature is also measured and subtracted from the saturation temperature to obtain the subcooling.

Figure 5.3 presents the characteristics of the experimentally obtained base CHF versus mass velocity. In $H = 4052 \mu\text{m}$ channels, R134a was tested at a 25°C saturation temperature with different subcoolings in the mass velocity range of $100\text{--}400 \text{ kg/m}^2\text{s}$. While CHF increased with mass velocity, its rate of rise was less at higher mass velocities. On the other hand, CHF were found to increase moderately with increasing inlet subcooling. At 20 K subcooling conditions, CHF occurred at $10\text{--}20\%$ higher heat flux of 3 K subcooling conditions. Consequently, the highest base heat flux reached 342 W/cm^2 at $400 \text{ kg/m}^2\text{s}$ with 20 K subcooling. This was the highest value reached in the present study. This value however should not be taken as the maximum that can be obtained with this fluid, as the test geometry was in no way optimized to find this limit.

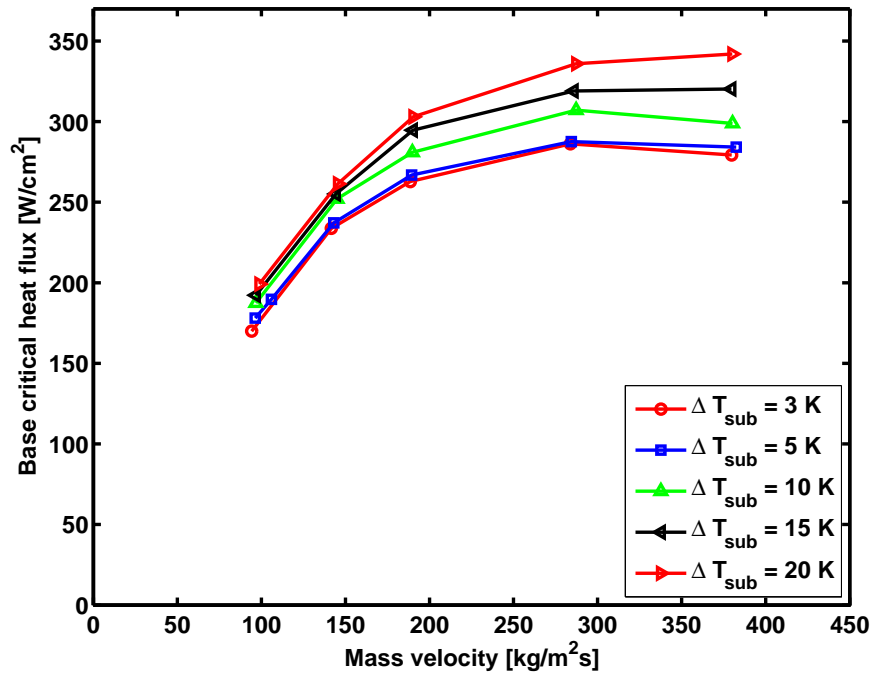


Figure 5.3: CHF data for R134a at $T_{\text{sat}} = 25^\circ\text{C}$ in $H = 4052 \mu\text{m}$ channels.

Figure 5.4 shows the experimental results for the same inlet pressure and temperature conducted in the $H = 756 \mu\text{m}$ test section. As the mass velocity increased, CHF also increased showing the same trend as before. However, no significant subcooling effect was observed; as has been similarly reported in another stable flow microchannel study by Wojtan et al. [46] and Agostini et al. [3].

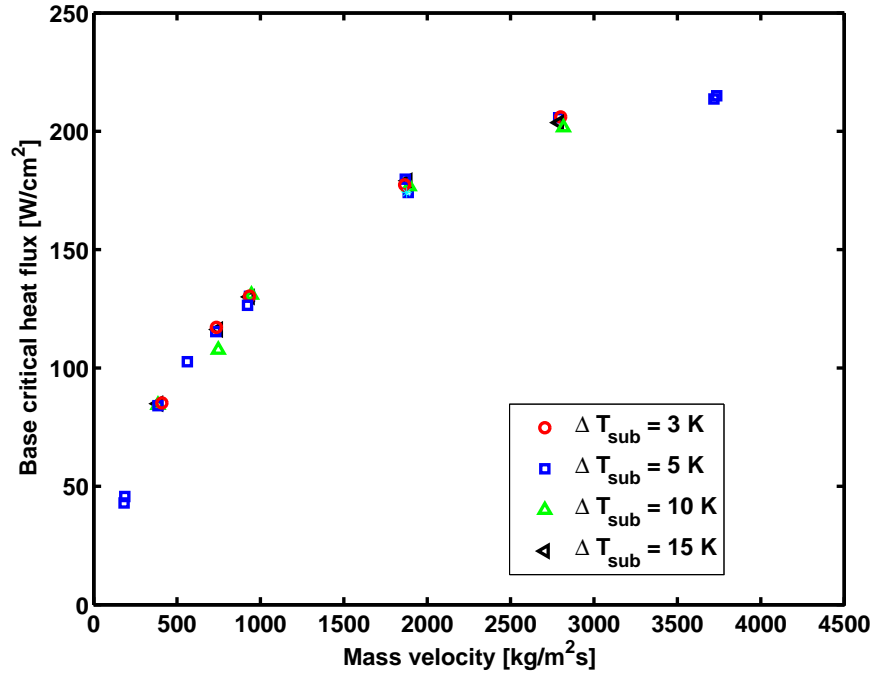


Figure 5.4: CHF data for R134a at $T_{\text{sat}} = 25^\circ\text{C}$ in $H = 756 \mu\text{m}$ channels.

In Figure 5.5, wall CHF instead of base CHF is plotted versus mass velocity. While the base CHF is useful to evaluate the overall cooling performance of different heat sinks, the wall CHF represents the actual effective heat flux on the channel perimeter. Since the fin efficiency varies locally along the channel in rectangular high aspect ratio channels, the average local heat flux along the channel is shown here. The log scale is used to cover the wide range of mass velocities tested. The test section of $H = 756 \mu\text{m}$ channels has $1/9$ the cross sectional area and $1/4$ the wetted wall perimeter of the $H = 4052 \mu\text{m}$ test section. Although the maximum cooling power was higher in the $H = 4052 \mu\text{m}$ test section, as shown in Figures 5.3 and 5.4, the maximum wall heat flux was higher in the smaller channels due to the higher mass velocity.

The different refrigerants are compared in Figure 5.6. For the tested conditions, all the fluids showed similar values while R236fa has slightly lower values. Since R134a has a lower frictional pressure drop than the others, R134a was able to be tested up to a larger mass velocity in the same test loop and thus recorded higher heat flux. Accordingly, R134a appears to be better as a cooling fluid than R236fa and R245fa with respect to CHF and the pressure drop.

Figure 5.7 presents the experimental CHF data versus inlet saturation temperature of the fluid; it shows curves obtained from different channel sizes, fluids and mass velocities. The CHF in $H = 4052 \mu\text{m}$ channels with a lower mass velocity increased with inlet saturation temperature, while the CHF in $H = 756 \mu\text{m}$ channels with high mass velocities decreased. The reversed tendency of the curves can be attributed to the adverse effects of other key parameters related to the system pressure. As the pressure increases, the liquid to vapor density ratio decreases, which has an effect of increasing CHF. However, decreasing the surface tension and the latent heat of vaporization tend to decrease CHF. Since those parameters work adversely with increasing system pressure, it is deducible that CHF can either increase or decrease depending on the flow condition and the channel size. Similarly, Kosar and Peles [27] observed that CHF increased with

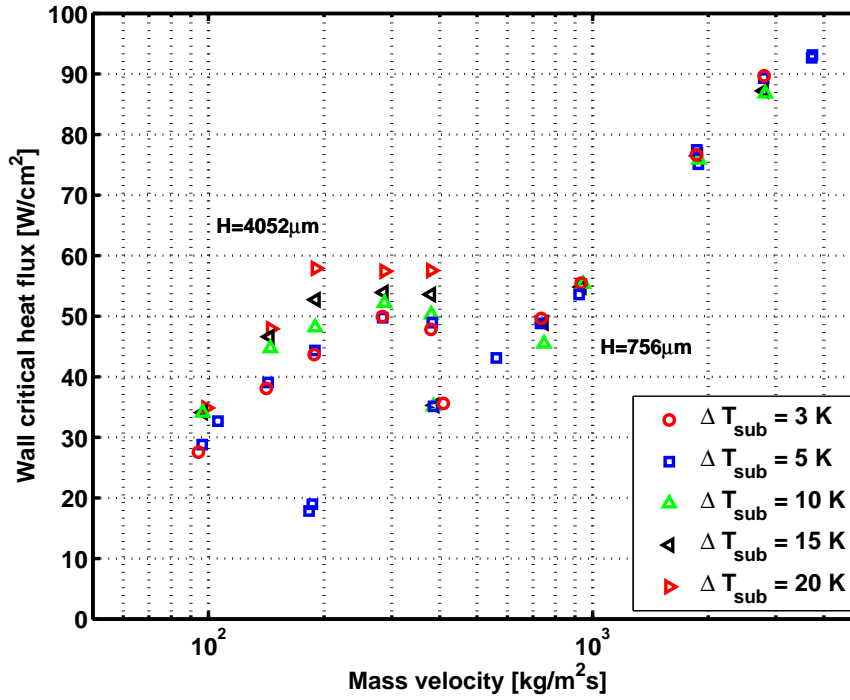


Figure 5.5: Effect of channel size with R134fa at $T_{\text{sat}} = 20^\circ\text{C}$.

increasing pressure up to a certain value but decreased beyond the maximum due to the adverse effects of other parameters altered with increasing system pressure.

5.3 Conclusions

All together, 323 new saturated CHF data in two multi-microchannel test sections have been obtained. Three low pressure refrigerants, R134a, R236fa and R245fa, were tested in test sections of $H = 4052 \mu\text{m}$ and $756 \mu\text{m}$ with aspect ratios of 8.7 and 3.8, respectively. A large range of test conditions were tested, targeting computer chip cooling applications. All the tests were conducted with orifices at the inlet of individual channels to suppress any back flow or instabilities. Different trends of the flow boiling curves were found and analyzed to choose the proper CHF. With increasing mass velocity, CHF increased but the rate of increase was smaller at high velocities. CHF increased moderately with large subcooling in the $H = 4052 \mu\text{m}$ channel. However, subcooling seemed to play less of a role as the channel size decreased. Among the refrigerants tested, R134fa showed higher performance than R236fa and R245fa as a cooling fluid with respect to CHF and pressure drop. The saturation temperature had a moderate effect on CHF.

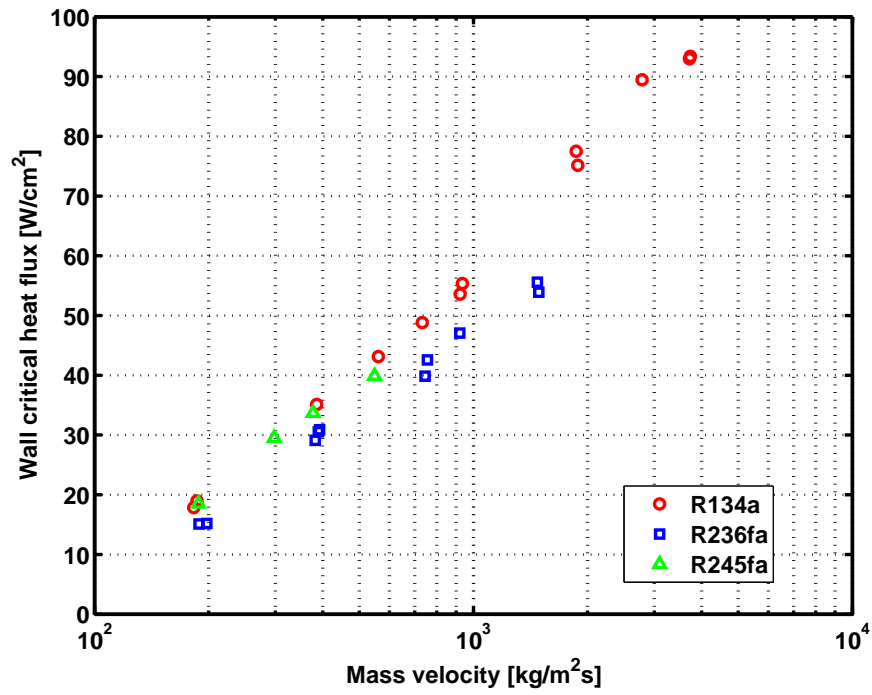


Figure 5.6: CHF data for different refrigerants at $T_{\text{sat}} = 25^\circ\text{C}$ and $\Delta T_{\text{sub}} = 5 \text{ K}$ in $H = 756 \mu\text{m}$ channels.

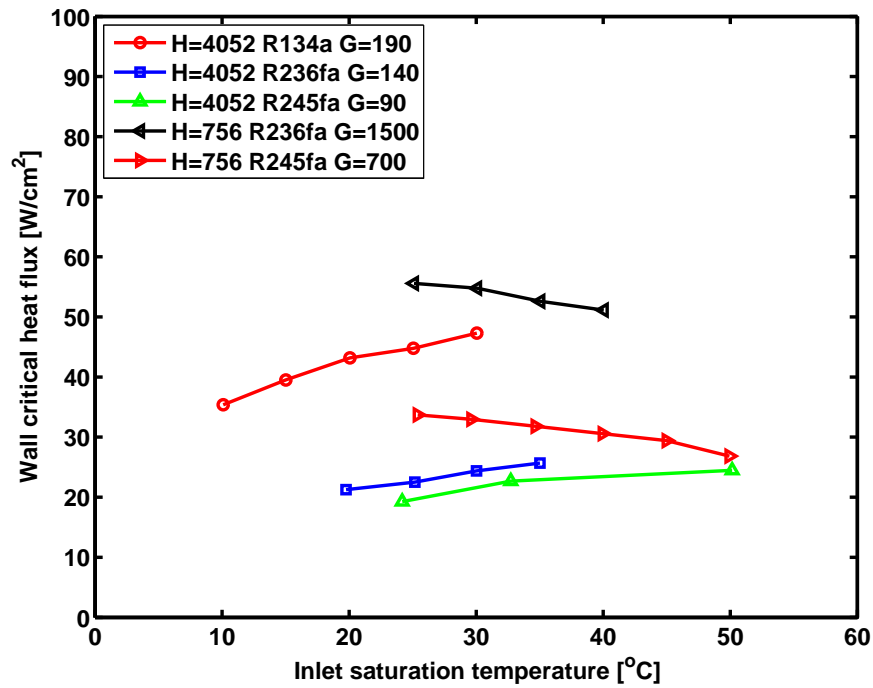


Figure 5.7: CHF data for different inlet saturation temperatures at fixed inlet subcooling of 5 K.

Chapter 6

CHF prediction methods and their comparison to the database

6.1 CHF prediction methods

The experimental results have been compared to the CHF correlations of Katto and Ohno [22], Katto [20], Qu and Mudawar [34], Wojtan et al. [46], and the theoretical 1-d numerical model of Revellin and Thome [37]. Simplified forms of the first four empirical methods are summarized in Table 6.1 and the reader is referred to their articles for full details. The correlations from Katto's research group was originally developed from single circular tube data in a mini/macro scale and is derived from a wide range of test conditions and fluids. In this study, an improved version by Katto and Ohno [22] was employed as well as the version for rectangular channels by Katto [20]. The Qu and Mudawar correlation [34] is a modified version of the Katto-Ohno correlation [22] based on their water CHF data in rectangular microchannels and R-113 data in heat sinks with multiple circular mini- and micro-channels. Meanwhile, the Wojtan et al. correlation [46] is based on their R134a and R245fa data in single circular tubes with diameters of 0.5 mm and 0.8 mm. For the last two methods, no inlet subcooling effect was considered. The fluid properties in the methods were calculated at the corresponding saturation temperature of the inlet measured pressure. Instead, only for the Qu-Mudawar correlation [34], the outlet pressure was used for the saturation temperature and property calculation as they used when developing their correlation. For the other models, using the outlet pressure instead of the inlet pressure changed the predictions less than 5% and caused no change in the trends for the current data.

Before presenting the results of this comparison, some comments on the definition of the equivalent diameter and mass velocity are needed, as these are important parameters in such correlations. To implement circular channel correlations for rectangular channels, some characteristic diameter has to be chosen. The following different definitions may be adopted:

1. Hydraulic diameter, D_h , based on the wetted perimeter.
2. Heated diameter, D_{he} , based on the heated perimeter only. This diameter was proposed in Katto [20] and used in Qu and Mudawar [34].

Table 6.1: Correlations for saturated CHF

Reference	Basic form of CHF correlation
	$q_c = q_{c0} \left(1 + K \frac{\Delta h_{in}}{h_{lv}} \right)$
Katto and Ohno [22] Katto [20]	$\frac{q_{c0}}{G \cdot h_{lv}} = \text{fn} \left(\frac{\rho_v}{\rho_l}, \text{We}, \frac{L}{D} \right)$
	$\text{We} = \frac{G^2 L}{\sigma \rho_l}$
Qu and Mudawar [34]	$q_c = 33.43 \cdot G \cdot h_{lv} \cdot \text{We}^{-0.21} \left(\frac{\rho_v}{\rho_l} \right)^{1.11} \left(\frac{L}{D} \right)^{-0.36}$
Wojtan et al. [46]	$q_c = 0.437 \cdot G \cdot h_{lv} \cdot \text{We}^{-0.24} \left(\frac{\rho_v}{\rho_l} \right)^{0.073} \left(\frac{L}{D} \right)^{-0.72}$

3. Area equivalent diameter, D_{eq} , based on the cross-sectional area of the channel. This is a diameter of a circular tube with the same cross-sectional area as the rectangular channel.

Since the hydraulic diameter D_h approximates to twice the channel width ($2 W_{ch}$) for the case when the channel height is much larger than the channel width ($H_f \gg W_{ch}$), this definition responds little to changes in the channel height H_f . Furthermore, the first two definitions give quite similar values for the present high aspect ratio channels whose top (short face) is adiabatic. Similarly, the mass velocity can take vastly different values in high aspect ratio rectangular channels, depending on the chosen definition. It can potentially be calculated using any of the above three diameters (assuming the mass flow rate passes through a channel of that diameter) or be based on the actual value from the channel's actual cross-sectional area, i.e. which is the same as G_{eq} .

Table 6.2 presents the definition of each of these diameters and mass velocities as well as their variation in the current test sections. For example, in the $H = 4052 \mu\text{m}$ channel, choosing the hydraulic mass velocity based on the hydraulic diameter results in a value 3.4 times the actual area equivalent mass velocity. Since the circular tube methods do not suggest which particular combination of definitions should be used, the current database has been used to determine the best set for non-circular channels.

Table 6.2: Definition of diameters and values

Parameter	Definition	H = 4052 μm	H = 756 μm
D_h	$\frac{4W \cdot H}{2W + 2H}$	0.84 mm	0.32 mm
D_{he}	$\frac{4W \cdot H}{W + 2H}$	0.88 mm	0.35 mm
D_{eq}	$\sqrt{\frac{4W \cdot H}{\pi}}$	1.55 mm	0.44 mm
G_h	$\frac{\dot{M}}{\pi D_h^2/4}$	3.4 G_{eq}	1.9 G_{eq}
G_{he}	$\frac{\dot{M}}{\pi D_{he}^2/4}$	3.1 G_{eq}	1.5 G_{eq}
G_{eq}	$\frac{\dot{M}}{W \cdot H}$	-	-

6.2 Comparison results

6.2.1 Comparison for each geometrical definition

Comparing the present results to the prediction methods, for the reader's reference, the mean absolute errors (MAE) when using different definitions for the diameter and mass velocity are summarized in Table 6.3. The best combination for predicting the data are D_{he} and G_{eq} , where the first reflects the actual heat transfer conditions, i.e. three sides heated, while the second is the actual mass velocity. Notably, using the traditional hydraulic diameter always gives the worst results. In this study, all experimental results in graphs and tables are presented based on the heated equivalent diameter D_{he} and the actual mass velocity G_{eq} , which was also employed by Qu and Mudawar [34] and Agostini et al. [3]. Moreover, the use of these definitions is consistent with the discussion of Lienhart [29] about using the true cross-sectional area for the mass flow rate and the bulk velocity of turbulent flow in non-circular ducts when the hydraulic diameter replaces the diameter from the circular tube formulas. The comparison between the predictions and experiments are discussed in further detail in the following sections using predictions based on D_{he} and G_{eq} .

Table 6.3: Mean absolute error (MAE) of experimental data to the prediction

Method	$D_{eq} \& G_{eq}$	$D_h \& G_h$	$D_{he} \& G_{he}$	$D_h \& G_{eq}$	$D_{he} \& G_{eq}$
H = 4052 μm	MAE = $\frac{1}{N} \sum \frac{ q_{c,m} - q_{c,p} }{q_{c,m}} \times 100(\%)$				
Katto-Ohno	38	115	107	21	18
Katto	52	147	137	21	19
Qu-Mudawar	365	662	630	272	280
Wojtan et al.	80	119	115	20	23
Revellin-Thome	33	82	78	21	18
H = 756 μm					
Katto-Ohno	27	60	45	23	23
Katto	35	68	54	26	26
Qu-Mudawar	510	693	626	442	463
Wojtan et al.	19	32	28	12	11
Revellin-Thome	12	19	16	23	19

6.2.2 Comparison for each test section

Figure 6.1 shows the ratio of the predictions of the Katto-Ohno correlation to the experimental data plotted versus mass velocity. The CHF data were generally well predicted, showing MAE's of 18.5% and 23.0% for $H = 4052 \mu\text{m}$ and $H = 756 \mu\text{m}$ channels, respectively. However, the CHF data in the smaller channels are significantly over predicted and the influence of mass velocity is not captured well as can be seen by the trend in the errors versus mass velocity. The Katto correlation for rectangular channels showed very similar results with the circular tube correlation. The reason is because most of the current test conditions fall into the same regime (low pressure and low mass velocity) where both of the methods provide an identical correlation. The Qu-Mudawar correlation failed to predict the present experimental data, yielding an order of magnitude difference with a resulting MAE over 280%.

Figure 6.2 shows the prediction of Wojtan et al. [46] correlation. This correlation yielded MAE values of only 22.6% and 10.5% for the two channel sizes. Especially for the smaller channels, this method shows excellent agreement. It is reasonable since the correlation is developed from the Katto and Ohno correlation [22] based on their 0.5 mm and 0.8 mm tube data.

Figure 6.3 compared the data with the numerical method of Revellin and Thome [37] using their interfacial wave height equation (Equation 2.3). It predicted the experimental trends well for all the fluids and geometries. The MAE values were 18.4% and 18.5% for each channel size, showing a good agreement for both of the test sections regardless of the aspect ratio.

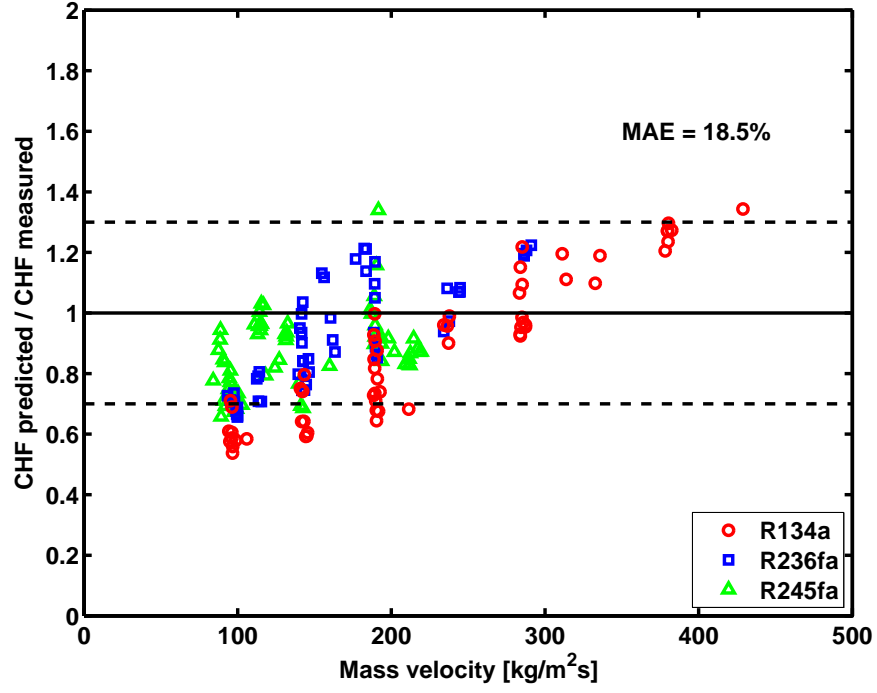
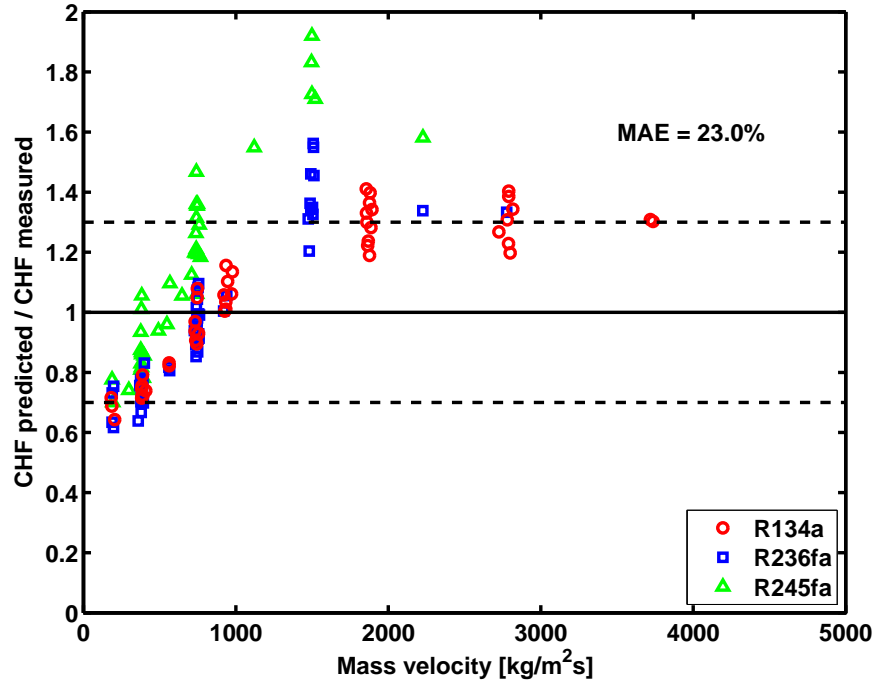
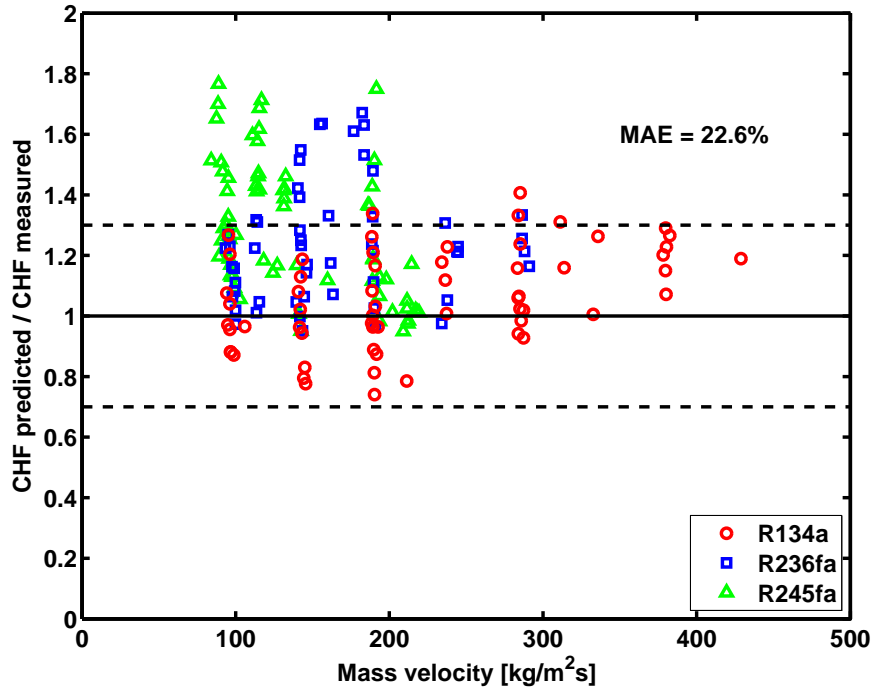
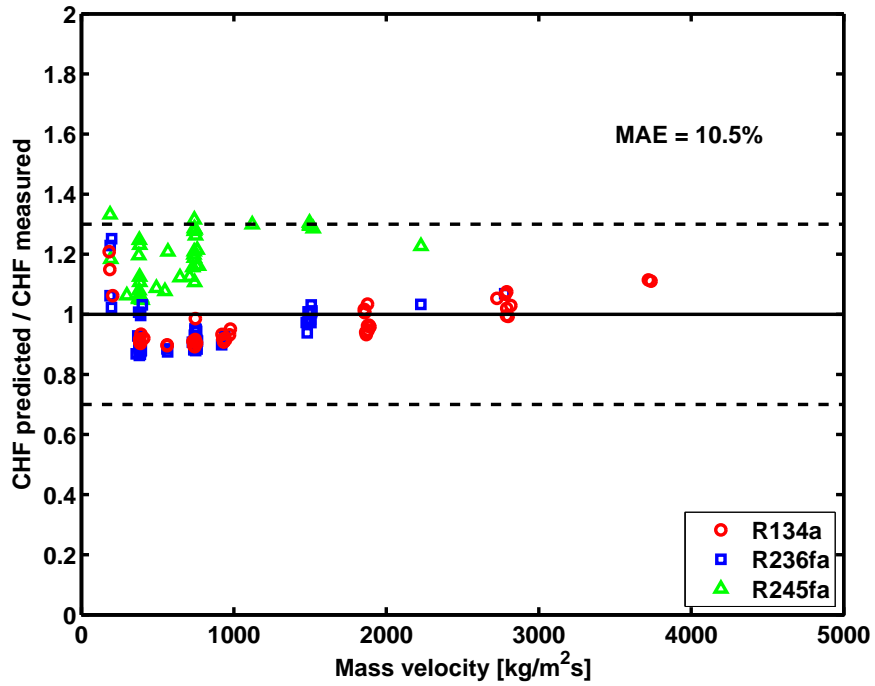

(a) $H = 4052 \mu\text{m}$ channels

(b) $H = 756 \mu\text{m}$ channels

Figure 6.1: Comparison of all data with the Katto-Ohno [22] correlation using D_{he} and G_{eq} .



(a) H = 4052 μm channels



(b) H = 756 μm channels

Figure 6.2: Comparison of all data with the Wojtan et al. [46] correlation using D_{he} and G_{eq} .

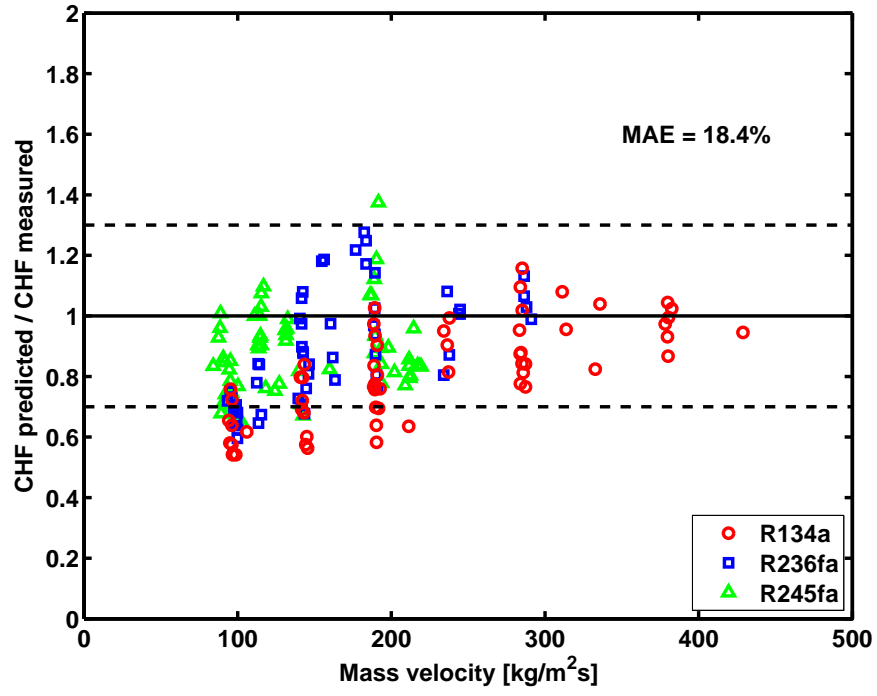
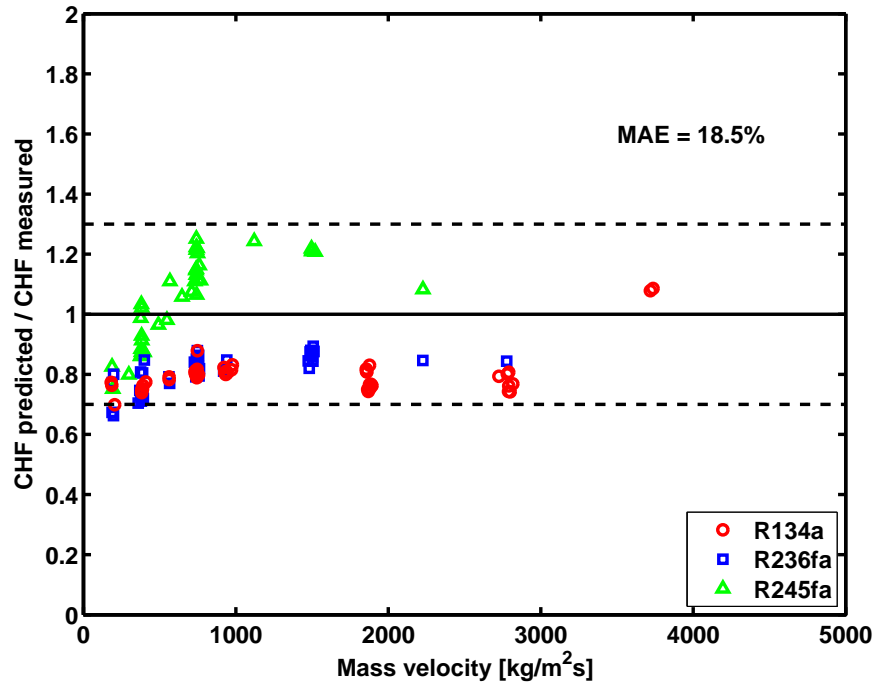

(a) $H = 4052 \mu\text{m}$ channels

(b) $H = 756 \mu\text{m}$ channels

Figure 6.3: Comparison of all data with the Revellin-Thome [37] numerical method using D_{he} and G_{eq} .

6.2.3 Detailed analysis of each prediction method

For the thermal design and optimization of micro-evaporation coolers with respect to CHF, it is interesting to see if the prediction methods correctly mimic the effect of the design parameters. The best design method should not only be accurate but also be parametrically correct. In Figure 6.4 (a)-(d), the ratio of the predictions of the Katto-Ohno correlation [22] to the experimental CHF was plotted versus various flow parameters for the two test sections and the three fluids. In Figure 6.4 (a), the x-axis is shown in log scale to cover the wide range of the mass velocities for the two different test sections. With the Katto-Ohno correlation, CHF was generally under-predicted in low mass velocities and over-predicted in high mass velocities. Figure 6.4 (b) and (c) show the ratio versus inlet saturation temperature and inlet subcooling, respectively. The correlation, in particular, over-predicted CHF of R245fa at high inlet saturation temperatures regardless of the inlet subcooling. In Figure 6.4 (d), the ratio of Katto-Ohno prediction to experimental CHF is observed to decrease consistently with increasing vapor quality. The correlation seems to fail to capture the effect of vapor quality on the current multi-microchannel CHF. Figure 6.4 (e) shows the quantitative comparison of the predicted CHF to the experimental CHF. For the two test sections and three fluids, 78% of the data were predicted within $\pm 30\%$, yielding an overall MAE of 20.4%.

The correlation of Wojtan et al. [46] is analyzed in Figure 6.5. Previously, the correlation was shown to predict CHF better in smaller channels (showing MAE of 10.5% for $H = 756 \mu\text{m}$ channels and 22.6% for $H = 4052 \mu\text{m}$ channels in Figure 6.2). However, no particular tendency was found along the other parameters although the data were scattered widely. For the two test sections and the three fluids, the correlation of Wojtan et al. predicted 84% of the data within $\pm 30\%$ and yielded an overall MAE of 18.3%.

In Figure 6.6, the prediction of the Revellin and Thome's numerical method was analyzed. Few data were significantly over- or under-predicted showing a highly concentrated distribution regardless of the test parameters. Only with the outlet vapor quality, the ratio has a slightly decreasing tendency with increasing vapor quality as shown in Figure 6.6 (d). For two test sections and three fluids, the overall MAE was 18.4% which is comparable to the 17.4% of the Wojtan et al. correlation. However, 88% of the data were predicted within $\pm 30\%$, which is the highest percentage among the analyzed prediction methods.

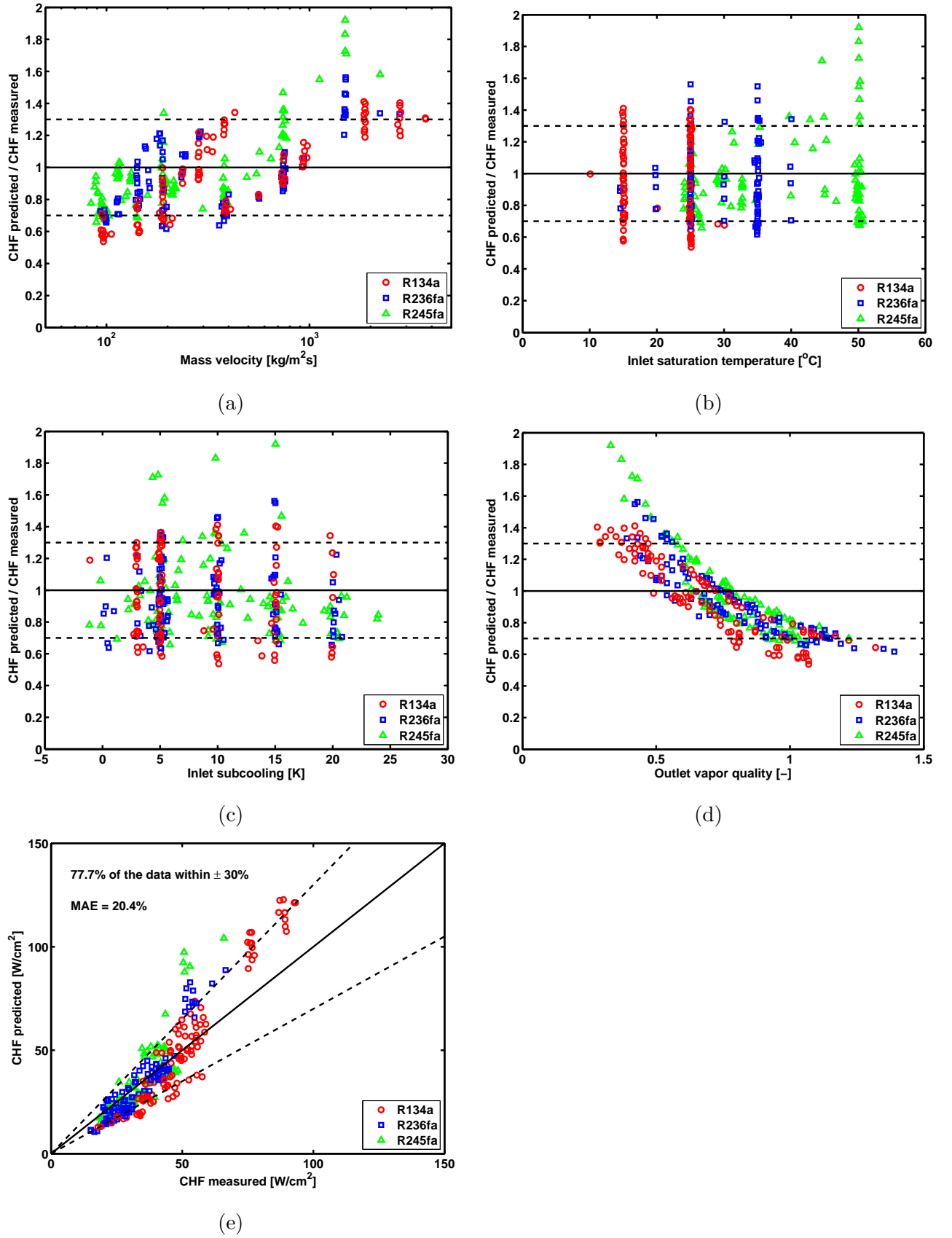
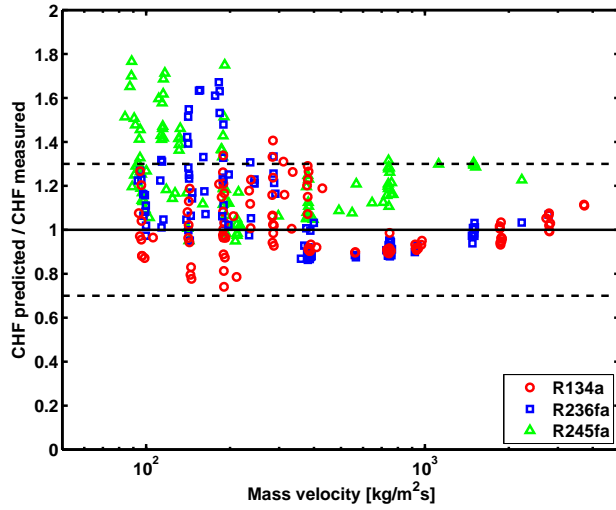
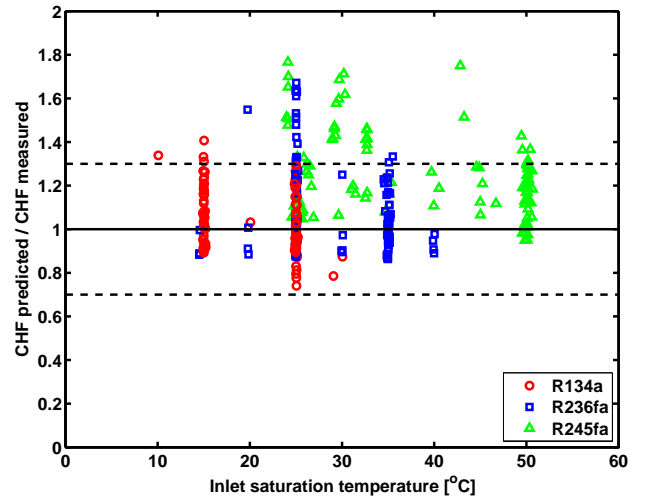


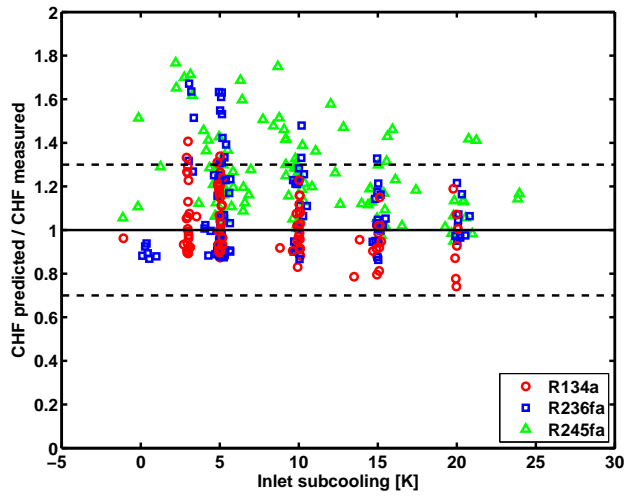
Figure 6.4: Katto-Ohno prediction to measured CHF versus test parameters.



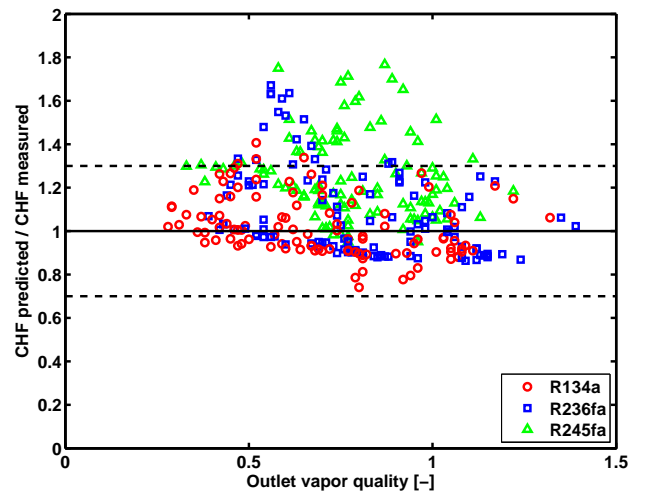
(a)



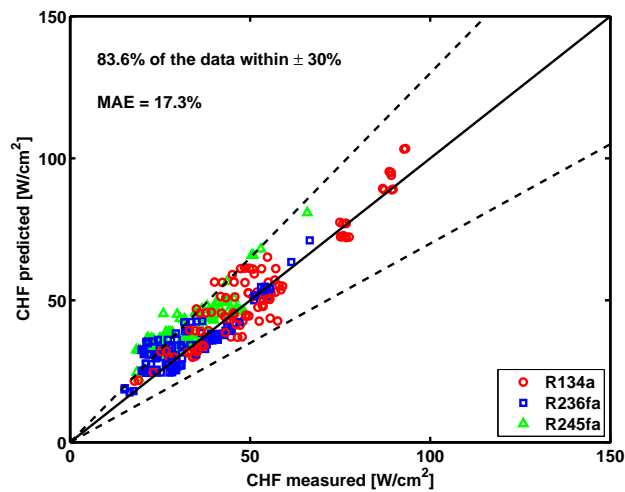
(b)



(c)



(d)



(e)

Figure 6.5: Wojtan et al. prediction to measured CHF versus test parameters.

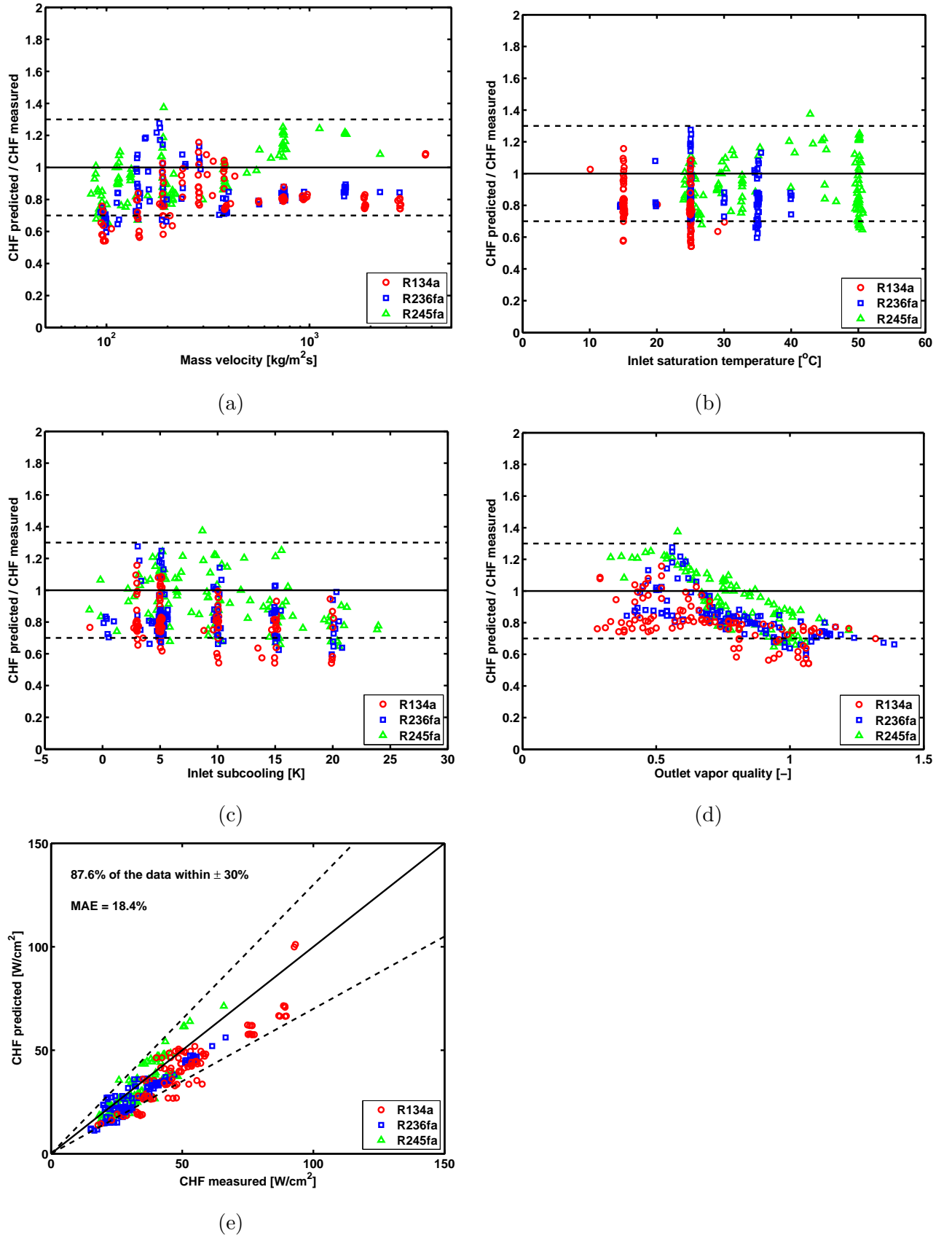


Figure 6.6: Revellin-Thome prediction to measured CHF versus test parameters.

6.3 Conclusions

The experimental data were compared with five prediction methods, including one numerical method. To implement the circular channel correlations for the current rectangular channel data, the use of different forms of an equivalent diameter and a mass velocity were examined. Using the heated equivalent diameter D_{he} and the actual mass velocity G_{eq} , the data generally matched well with the predictions of Katto and Ohno [22], Wojtan et al. [46] and Revellin and Thome [37]. The data from the smaller channel, $H = 756 \mu\text{m}$, matched extremely well with the predictions of Wojtan et al. [46]. The numerical method of Revellin and Thome [37], considering the evolution of film thickness and wave height, also seems very promising to predict microchannel CHF as well as the mini channel data, regardless of the aspect ratio.

Chapter 7

Effect of inlet orifice and flow visualization

Instability in multi-microchannel flow boiling needs to be treated carefully since it can cause a significant change on the results. Bergles and Kandlikar [5] questioned the validity of Qu and Mudawar's CHF results [34] since their tests were conducted with unstable conditions. Therefore, several researchers, such as Kandlikar et al. [19] and Kosar et al. [26] tried to prove the effectiveness of inlet restrictions to reduce flow instabilities. Since these experiments were conducted on silicon channels, these inlet restrictions were fabricated during the etching process of the channels. Here in this study, instead, the inlet restriction was realized by inserting a separate piece with orifice holes in the inlet plenum of the heat sink. By removing the insert, the same flow conditions could be repeated in the exact same test section to prove the effectiveness of the orifice.

Imaging technology has advanced considerably in recent decades, with the rise of optical and digital photographic technology. This enables researchers to overcome certain difficulties associated with visualization studies of complex boiling phenomena. In this study, a high speed camera, a Photron Fastcam-ultima APX with a maximum recording speed of 120'000 frames per second, was used to analyze flow behaviors in the microchannel heat sink.

Visualization confirmed the existence of instability, back flow and non-uniform distribution of flow along and among the channels when the orifice insert was removed. Flow patterns in the microchannels and their evolution with increasing heat flux were observed. Flow boiling curves and CHF results in both configurations were compared for a quantitative analysis.

7.1 Flow characteristics without the inlet orifice insert

Overall flow distribution and patterns

The test section shown in Figure 7.1 consists of an inlet port, an inlet plenum, multi-microchannels, an outlet plenum, and an outlet port. The flow enters from the inlet port located at the top left. The fluid in the inlet plenum is distributed into the multi-channels and flows from left to right. The flow out of the

channels merge again in the outlet plenum before leaving through the outlet port at the bottom right. The inlet and outlet plenums were designed to prevent recirculation at its corners and to minimize the plenum's pressure drop. The cross-sectional area of the plenum is 0.9 cm^2 while that of all the channels is 0.38 cm^2 for the $H = 4052 \text{ }\mu\text{m}$ section and 0.04 cm^2 for the $H = 756 \text{ }\mu\text{m}$ section. One should also remember that the $2 \text{ cm} \times 2 \text{ cm}$ heater leaves an adiabatic zone of 0.5 cm at the entrance and the exit of each channel.

Figure 7.1 (a) shows the flow behaviors of R245fa in the $H = 4052 \text{ }\mu\text{m}$ test section without the orifice at a mass velocity of $240 \text{ kg/m}^2\text{s}$, saturation temperature of 50°C , subcooling of 20 K and heat flux of 212 W/cm^2 , which is very close to CHF. The dark area in the middle of the channels represents a mixture of bubbles. Upstream of the bubble mixture region, the bright area in some channels represents single phase subcooled liquid. Downstream of the bubble mixture region, the less bright area represents an annular flow pattern.

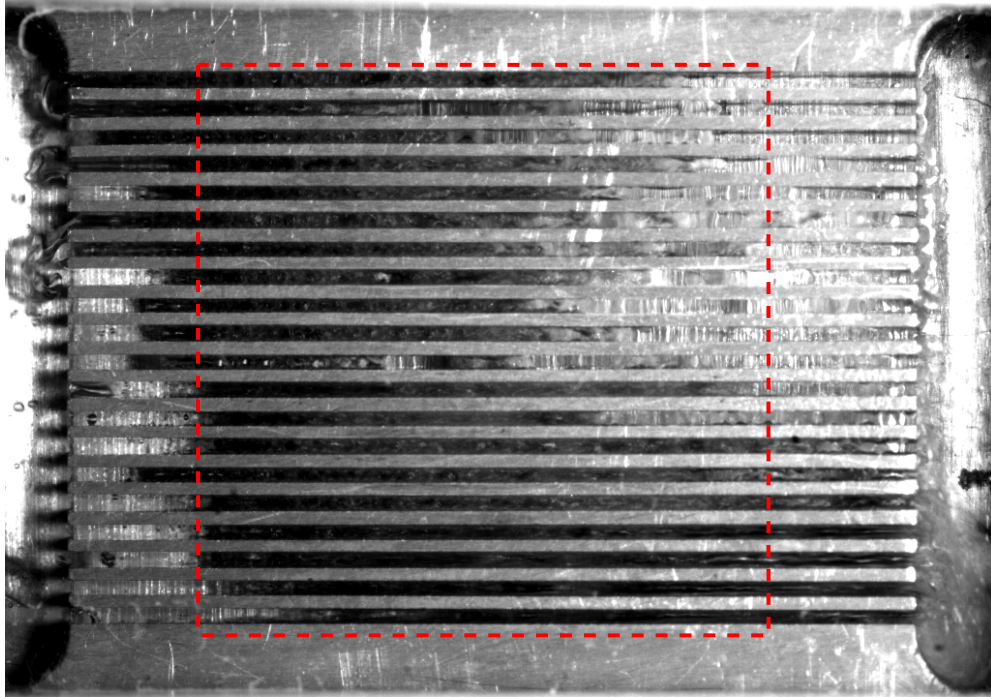
When boiling occurs and a bubble is generated and grows, the bubble pushes the adjacent fluid outward regardless of the direction. Since there is no restriction at the inlet of the channels, the flow may easily go back into the inlet plenum. Therefore, a few bubbles were observed in the inlet plenum, which merged, moved and broke again to flow back into the channels. Moreover, the front edges of the bubble mixture region thus were not uniform among the channels.

In the first few channels from the top in Figure 7.1 (a), the bubble mixture region occurs from the entrance of the channel. The entrances of those channels are located close to the inlet port. Then, the flow pattern in these channels became an annular flow and dried out at or near the end of the channel. On the other hand, a different type of flow was observed for the channels located far from the inlet port (at the bottom of the image). In these channels, the bubble mixture region was followed after a certain length of single phase liquid. Moreover, the flow came out of the channel without experiencing dry out and merged together in the outlet plenum. It can be concluded that these nonuniform flow patterns among the channels implies mal-distribution of the flow among the channels.

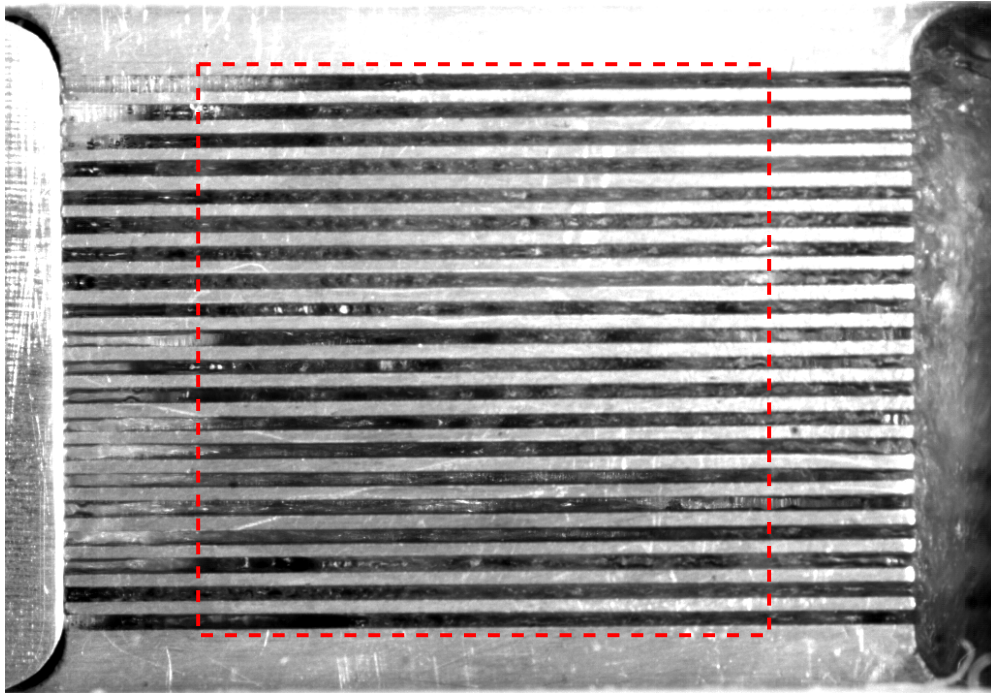
Figure 7.1 (b) shows the same test section at a similar test condition, but with the orifice insert installed for comparison. The mass velocity was $211 \text{ kg/m}^2\text{s}$ at a saturation temperature of 51°C , a subcooling of 20 K with a heat flux of 213 W/cm^2 . Unlike the previous case, reversed flow from the boiling incipient position is blocked by the inlet orifice, thus suppressing the multi-channel instability. Moreover, the flow patterns seem more uniform across the channels. In the outlet plenum, all the channels were observed to still have liquid in the outflow thus implying no local upstream dry out had occurred at the same condition.

The uniformity of the flow distribution is one of the important issues encountered in multi-microchannel heat sinks. If the flow is not well distributed among the channels, the mass velocity estimated by dividing the total mass flow rate by the cross sectional area of all the channels differs from the actual mass velocity in a channel. In addition, since the flow behavior in one channel differs from that in the other channel, it makes the phenomena more complicated for interpretation.

Figure 7.2 (a) and (b) shows another comparison at a lower mass velocity of $G = 80 \text{ kg/m}^2\text{s}$. Similar flow behaviors were observed with stronger back flow motion without the orifice in Figure 7.2 (a), resulting in flow mal-distribution as well as a large local dry out area in the upper channels. In Figure 7.2 (b), with the orifice, all the channels show very similar flow patterns and the bubble mixture region length. Moreover, the uniform flow coming out of the channel exits implies that the flow were well distributed.

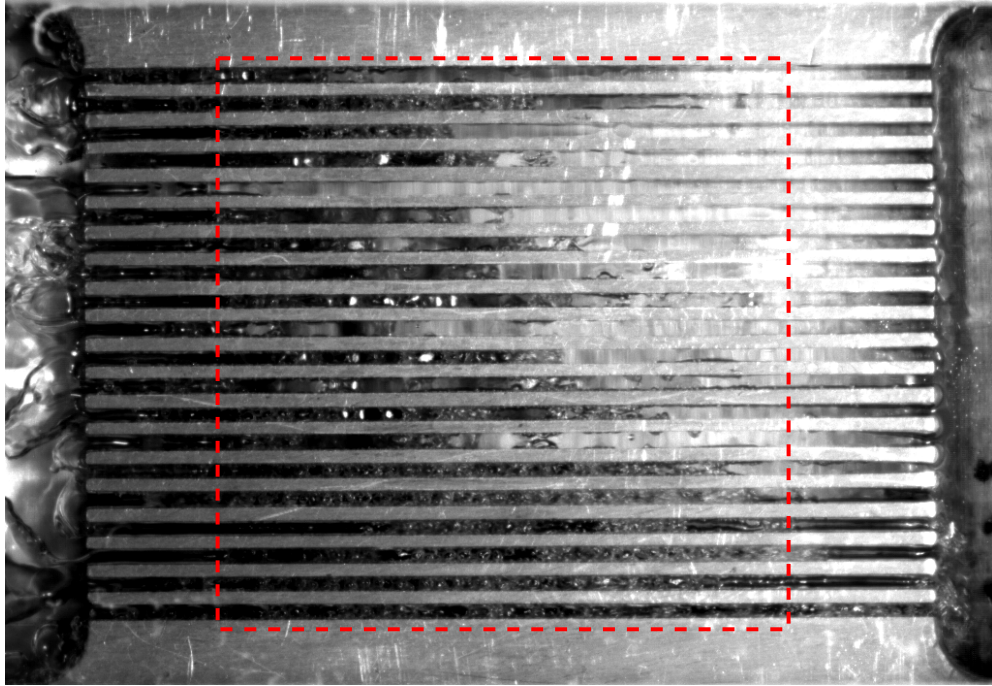


(a) Without orifice

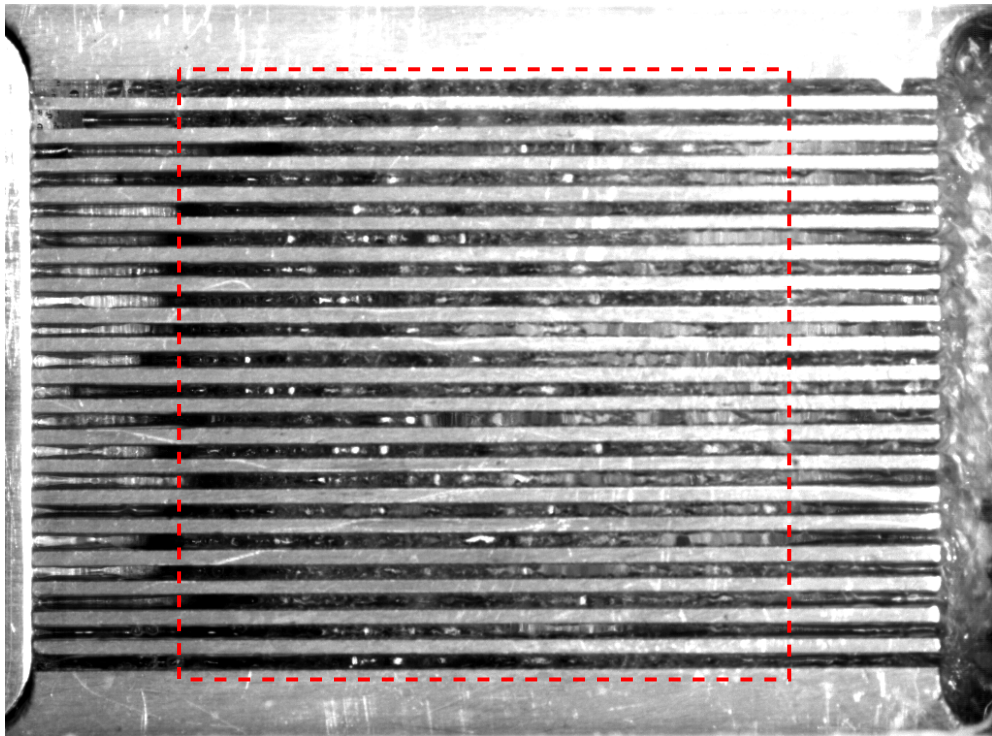


(b) With orifice

Figure 7.1: Visualization of the $H = 4052 \mu\text{m}$ test section at a high mass velocity (a) without and (b) with the orifice insert. Flow direction is from left to right. Red dashed line shows the heating area. Bright area in the channels represents single phase liquid (near inlet) or annular flow (near outlet) while dark area represents two phase bubble mixture.



(a) Without orifice



(b) With orifice

Figure 7.2: Visualization of the $H = 4052 \mu\text{m}$ test section at a low mass velocity (a) without and (b) with the orifice insert. $G = 80 \text{ kg/m}^2\text{s}$, $T_{\text{sat}} = 40^\circ\text{C}$, $\Delta T_{\text{sub}} = 20 \text{ K}$ and $q_b = 115 \text{ W/cm}^2$. Flow direction is from left to right. Red dashed line shows the heating area. Bright area in the channels represents single phase liquid (near inlet) or annular flow (near outlet) while dark area represents two phase bubble mixture. Very bright area represents dryout zone in top image.

Backflow and multi-channel instability

Figure 7.3 shows a sequence of video images to demonstrate the back flow motion when the orifice insert is not installed. A slug bubble was observed at the inlet of the channel in (a). When the flow in the channel is pushed upstream due to a bubble growth downstream, the bubble goes back into the inlet plenum in (b), since there is no restriction at the inlet of the channel. The reversed bubble moves quickly to one of the adjacent channels, (c), and breaks down into smaller parts before going into these channels, (d). The inserted bubble becomes stagnant depending on its location, (e) and (f), before moving again forwards or backwards. Furthermore, some of the bubbles in the inlet plenum recirculate for a moment before they re-enter the channels. While the flow inside the channel oscillates forwards and backwards, coalescence of the smaller bubbles was also observed. A similar multi-channel instability was previously reported by Qu and Mudawar [34]. Flow recirculation in the inlet plenum implies the instability of inlet fluid condition.

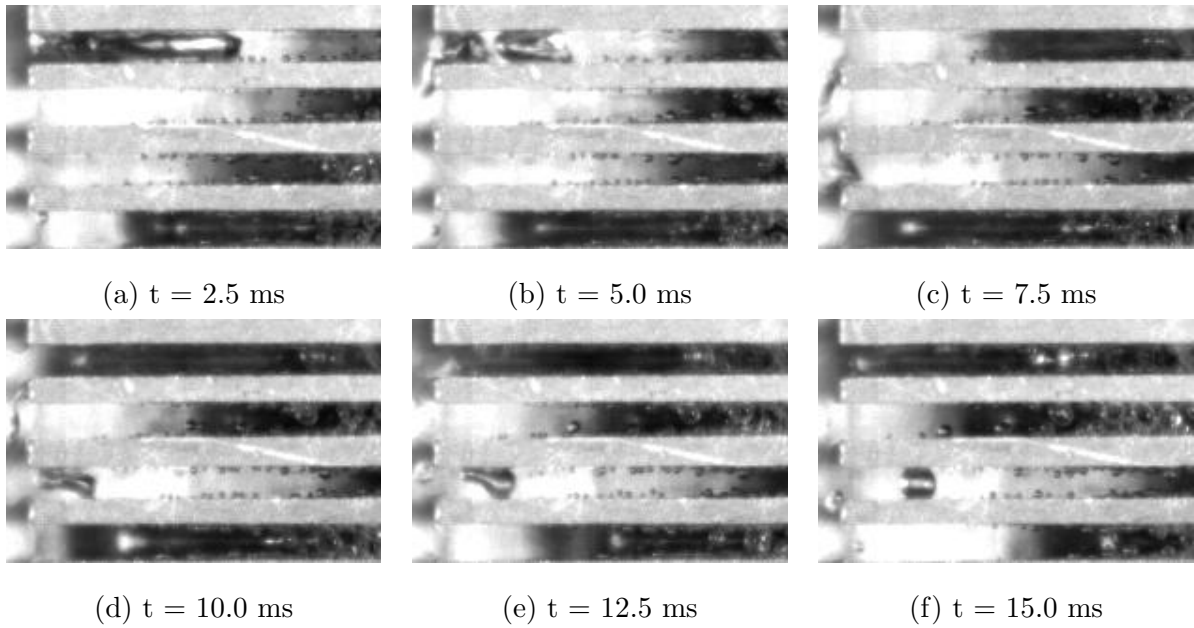


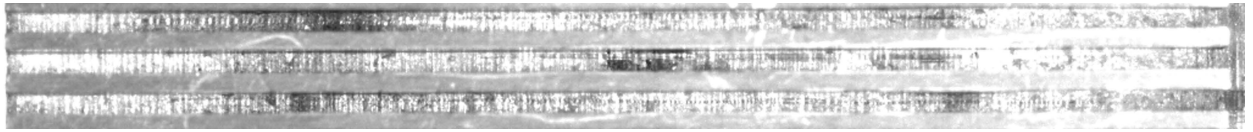
Figure 7.3: Sequence of images with time near the inlet of channels showing back flow and parallel channel instability in a case with no orifice insert. The main flow direction is from left to right at $G = 240$ kg/m²s, $T_{\text{sat}} = 50^\circ\text{C}$, $\Delta T_{\text{sub}} = 20$ K and $q_b = 212$ W/cm² in the $H = 4052$ μm test section.

7.2 Flow characteristics with the inlet orifice insert

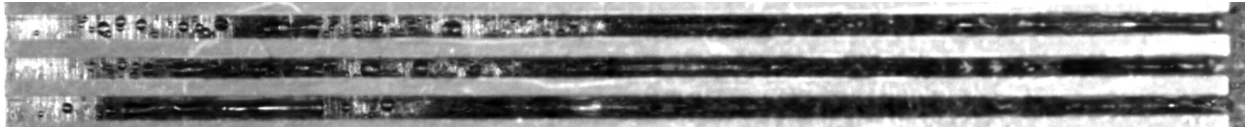
Flow patterns in the multi-microchannels when using the orifice inserts are analyzed in more detail here. A general overview of flow pattern at different heat fluxes is shown first. Sequences of images from videos are used to demonstrate a few selected observations, also by means of schematics.

Evolution with increasing heat flux

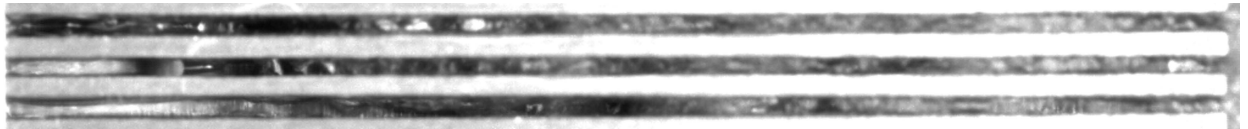
Flow patterns were observed with increasing heat flux in Figure 7.4 (a)-(d). Without any heat flux, the channel inside shows only single phase liquid as in (a). At a low heat flux in (b), bubbly flow was observed near the inlet. Further downstream, vigorous boiling occurs and easily forms confined bubbles. It is noticeable that as a bubble grows at the boiling incipient position, it pushes the adjacent fluid in the forward, backward and upward directions. The upward flow separates again, going either forward or backward. The backward flow which might have entered into the inlet plenum without the inlet orifice, was blocked by the orifice and reverses direction to join with the inlet flow, making a recirculation loop in this high aspect ratio rectangular channel. The bubbles recirculating near the inlet form an elongated bubble zone as the heat flux increases. At a higher heat flux in (c), mixture of elongated bubbles were observed near the inlet of the channel. Since the inlet fluid is highly subcooled in this condition, the flow out of the orifice takes a form of a liquid jet without flashing to pass through the elongated bubble zone near the inlet. Figure 7.4 (d) shows a flow pattern at $q_b = 250 \text{ W/cm}^2$, a few percent below CHF. The liquid jet stream takes a brighter color implying that the vapor zone has only a very thin liquid film along the channel wall near the inlet. Downstream of the channel, the very bright area in the channels represents an annular flow pattern, i.e. that assumed to occur at CHF in the Revellin and Thome [37]. Some particular phenomena will be explained in detail in the next sections.



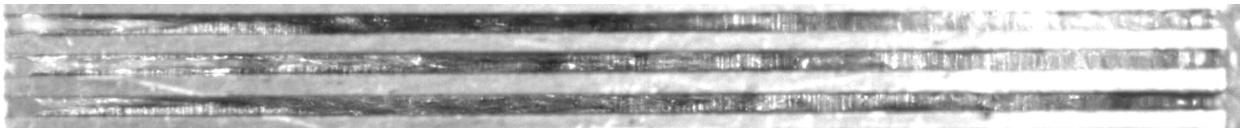
(a) $q_b = 0 \text{ W/cm}^2$ before heating



(b) $q_b = 45 \text{ W/cm}^2$ after boiling starts



(c) $q_b = 200 \text{ W/cm}^2$ at higher heat flux



(d) $q_b = 250 \text{ W/cm}^2$ approaching to CHF

Figure 7.4: Flow patterns at different heat fluxes at $T_{\text{sat}} = 50^\circ\text{C}$, $\Delta T_{\text{sub}} = 20 \text{ K}$, $G = 200 \text{ kg/m}^2\text{s}$ with R245fa in the $H = 4052 \mu\text{m}$ test section.

Flow Recirculation

Due to the inlet orifice, instability such as back flow was successfully prevented. However, it made the flow inside the channels to behave differently. Figure 7.5 shows sequential images at the inlet part of one channel with different time steps. The video was taken at a shutter speed of $1/8000$ sec. To demonstrate the behavior clearly, only a few images are shown in this zoomed view. The time step between the images was 0.25 msec. With the 25 images, they represent the flow motion in 6.25 msec. The diameter of the circular orifices was $300\text{ }\mu\text{m}$.

Since the inlet flow was sufficiently subcooled, the flow comes into the channel as a single liquid phase. Passing through the channel, with the heat flux coming from the bottom and the side walls, the flow starts to boil in a position somewhere near in the middle of the channel length. When boiling starts, the bubble generated pushes the neighboring fluid away in all directions. Since the channel has a high aspect ratio, the flow and bubbles easily reach the top of the channel, which was kept adiabatic because of the transparent glass cover. While a part of the flow goes downstream, the other part of the flow goes toward the inlet of the channel, showing a behavior similar to a natural convection cell. When they reach to the inlet, the existence of the inlet orifice blocks the back flow so that the backward flow merges to the newly incoming liquid jet at the bottom of the channel. When the stream from the inlet encounters an upward flow from the boiling incipient position, part of the stream was taken upward again making a recirculation loop. Similar flow behavior at a different flow condition is illustrated in Figure 7.6 with a schematic of flow direction. For observations at this lower mass velocity, the movement of recirculation slowed down. The sequential images were taken in 80 msec.

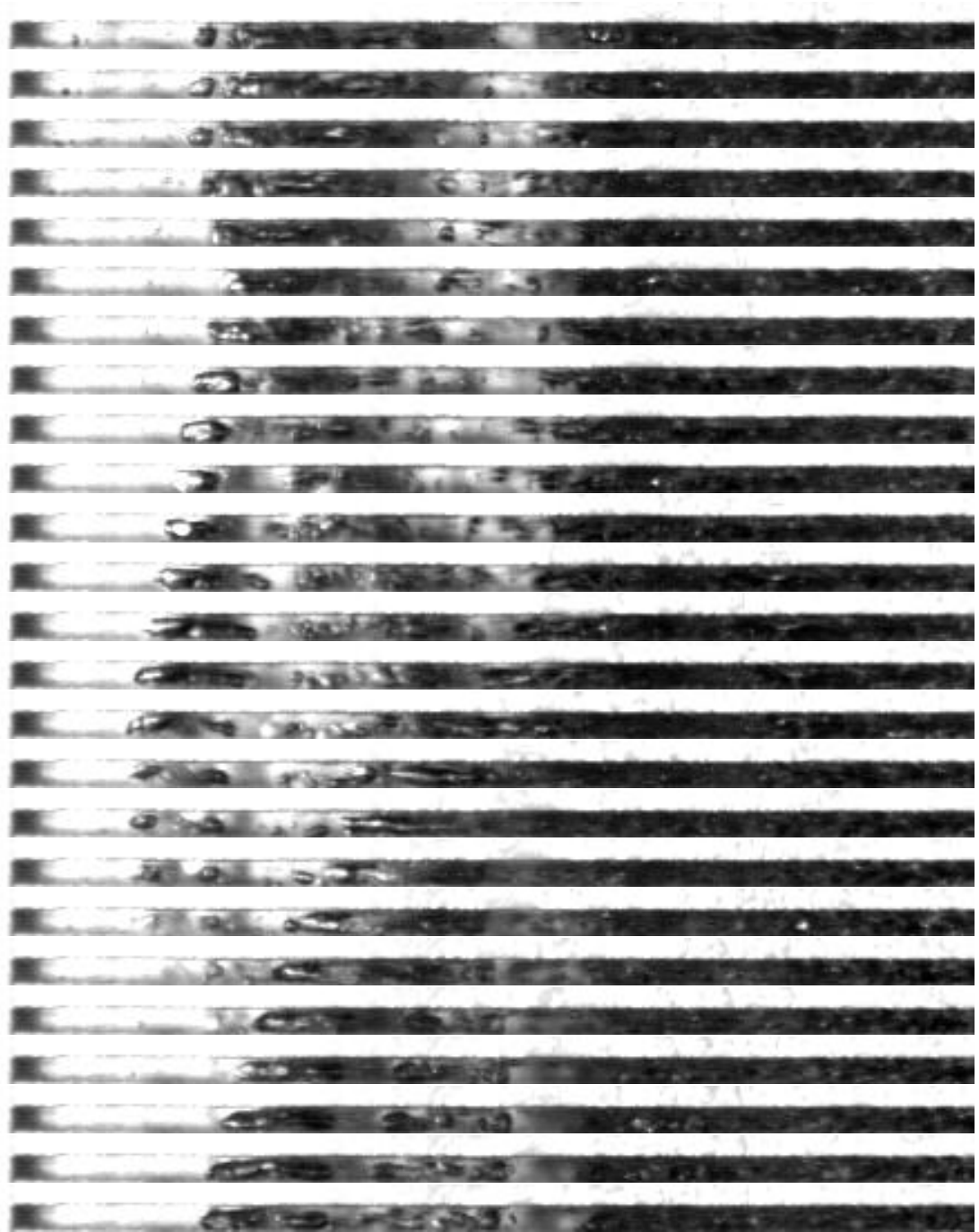


Figure 7.5: Visualization of recirculating flow near the inlet with the orifice insert installed. Sequence of images on one channel at the frame rate of 4000 image/sec (every 5 msec) during 6.25 msec. Images are for R134a at $T_{\text{sat}} = 21^\circ\text{C}$, $\Delta T_{\text{sub}} = 11\text{ K}$, $G = 680\text{ kg/m}^2\text{s}$ and $q_b = 100\text{ W/cm}^2$ in the $H = 4052\text{ }\mu\text{m}$ test section. Bright area represents single phase liquid while dark area represents bubble mixture.

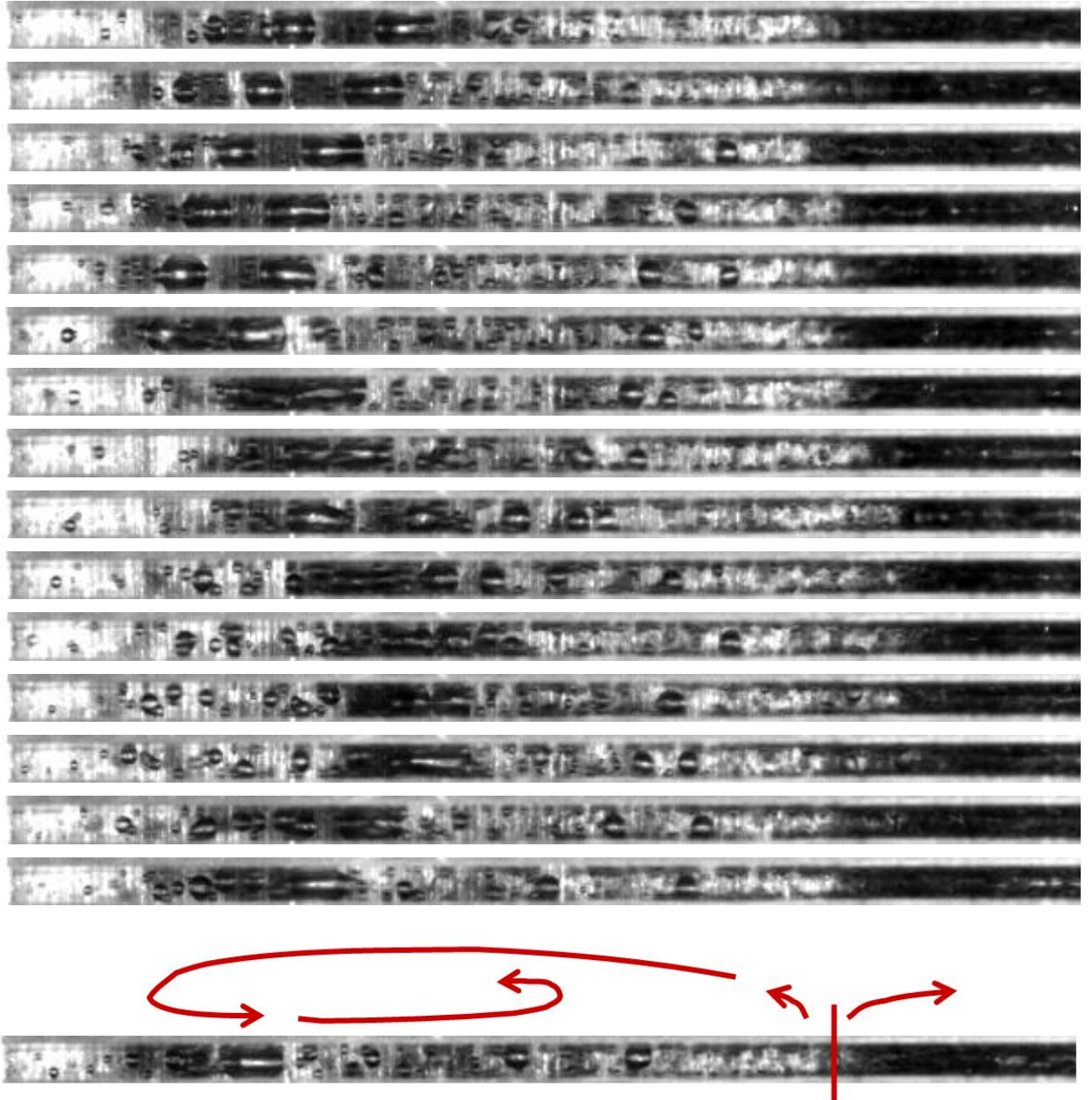


Figure 7.6: Visualization of recirculating flow near the inlet with the orifice insert installed. Sequence of images on one channel taken every 5 msec during 80 msec. Images are for R245fa at $T_{\text{sat}} = 50^\circ\text{C}$, $\Delta T_{\text{sub}} = 30\text{ K}$, $G = 200\text{ kg/m}^2\text{s}$ and $q_b = 45\text{ W/cm}^2$ in the $H = 4052\text{ }\mu\text{m}$ test section.

Inlet liquid jet stream

With increasing heat flux, the recirculated bubbles at the inlet of channels began to merge together to form elongated bubbles. Since the inlet flow was highly subcooled, the inlet flow through the orifice formed a liquid jet at a higher heat flux. Figures 7.7 (a) and (b) illustrate the liquid jet stream passing through what appears to be a vapor trapping zone near the inlet of the channels. The liquid jet broke down downstream and merged together with the liquid-vapor mixture near the boiling incipient position. One must remember that this is occurring in the unheated entrance length of 0.5 cm of the channels.

Similar observations have been reported in the literature: Schneider et al. [38] investigated hydrodynamic characteristics in microchannel flow with an inlet orifice. In their flow visualization, they reported that a liquid jet stream was generated at the inlet orifice with vapor twin bubbles beside. On the other hand, Kuan [28] also reported similar observations in their CHF tests in multi-microchannel heat sinks describing it as a non-contacting liquid stream. However, their non-contacting liquid stream was preferably observed downstream at high heat flux, therefore implying an effect on the CHF. The vapor layer around the liquid core is prone to dryout, therefore dryout can occur further upstream than for cases without inlet orifice.

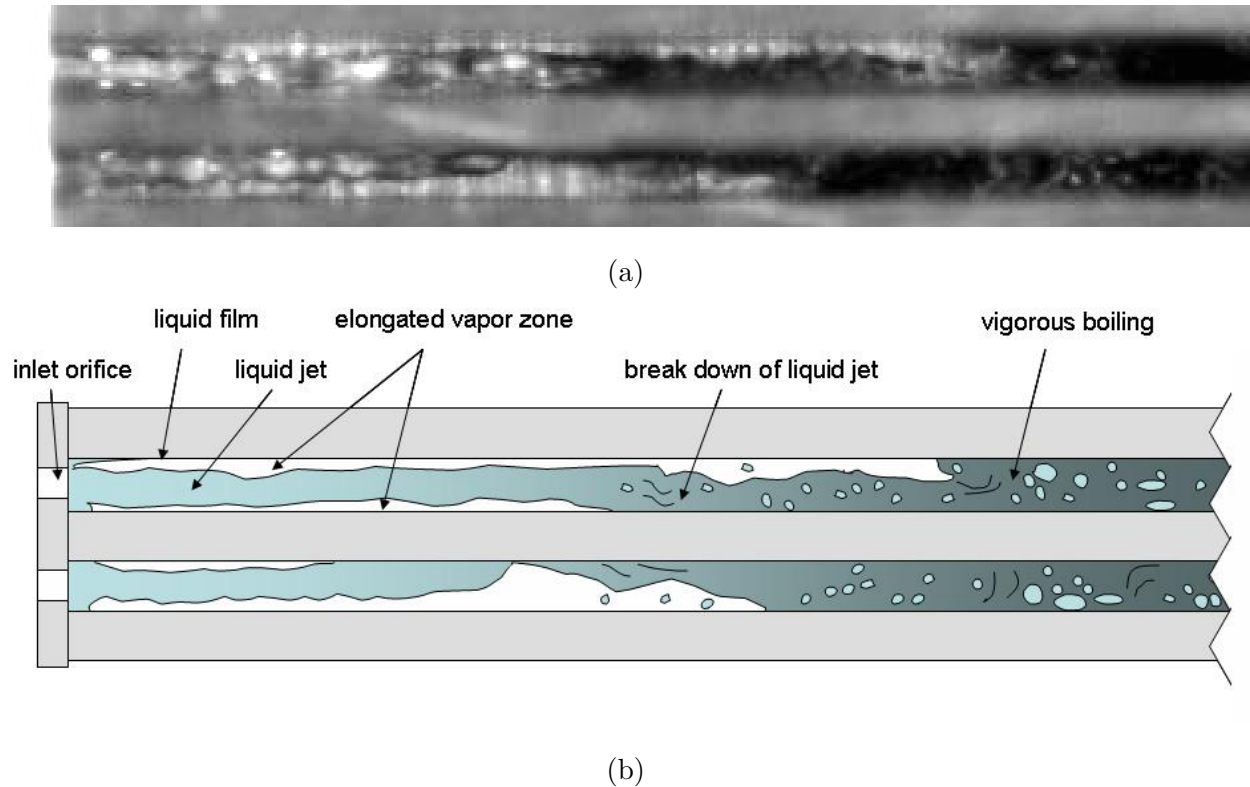


Figure 7.7: (a) Visualization of inlet jet stream near the inlet with the orifice insert installed and (b) a schematic diagram of the video image. Images are for R245fa at $T_{\text{sat}} = 50^\circ\text{C}$, $\Delta T_{\text{sub}} = 17\text{ K}$, $G = 106\text{ kg/m}^2\text{s}$ and $q_b = 172\text{ W/cm}^2$ in the $H = 4052\text{ }\mu\text{m}$ test section.

Flashing effect

When inlet flow has a very low subcooling, the fluid can be evaporated by pressure drop through the orifice. In this case, the inlet flow enters the channel as bubble mixture. Figures 7.8 (a) and (b) illustrate the flow boiling initiated by the flashing effect through the orifice. The flow enters the channels at a saturated flow condition from the left at a mass velocity of $280 \text{ kg/m}^2\text{s}$ and an inlet fluid temperature of 17°C . The fluid was R134a and heated at 20 W/cm^2 . The video was taken at a shutter speed of $1/120'000 \text{ sec}$ using a long duration flash system. Generally, without significant pressure drop, the fluid should be superheated over its corresponding saturated temperature to initiate boiling. However, by the flashing effect, bubbles were already generated in the incoming flow through the orifice. Therefore, flow boiling is also observed in the unheated entrance length of 0.5 cm of the channels. Since the orifice was located at the bottom of the channel, the outlines of the incoming bubbles are not seen clearly. The high aspect ratio of the channel allows forming to form several layers of fluid moving differently. On the other hand, due to the unheated transparent top glass, several bubbles became stagnant on the top, which is shown in the schematic diagram. Along the channel, the flow became more complicated showing vigorous flow movement on different layers. This flashing effect through the orifice has an advantage of reducing unnecessary overshoot of wall temperature as well as providing a more uniform wall temperature distribution spatially along the channel.

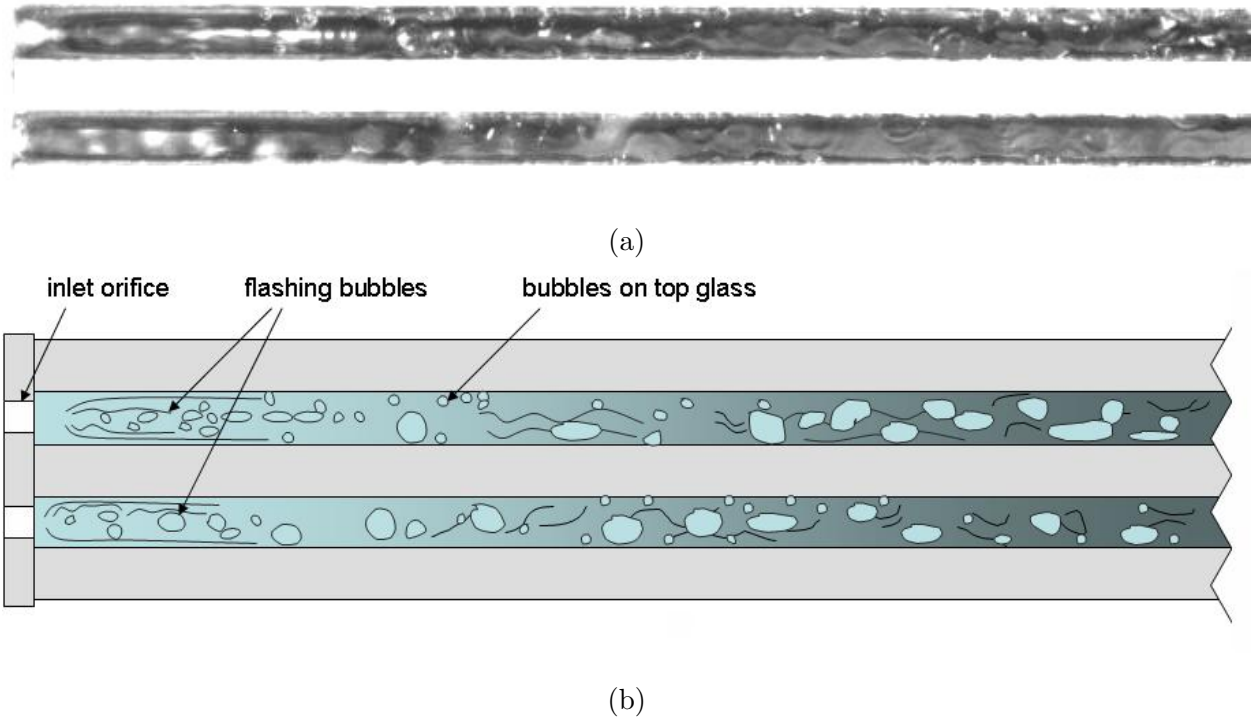


Figure 7.8: (a) Visualization of flashing effect through the orifice insert installed and (b) a schematic diagram of the video image. Images are for R134a at $T_{\text{sat}} = 17^\circ\text{C}$, $\Delta T_{\text{sub}} = 0 \text{ K}$, $G = 280 \text{ kg/m}^2\text{s}$ and $q_b = 20 \text{ W/cm}^2$ in the $H = 4052 \text{ }\mu\text{m}$ test section.

7.3 Comparison of flow boiling curves and CHF results

Flow boiling curves

For a quantitative analysis, flow boiling curves obtained with and without the orifice inserts were compared. Figure 7.9 shows the base heat flux versus the measured wall temperature at $G = 2000 \text{ kg/m}^2\text{s}$, $T_{\text{sat}} = 25 \text{ }^\circ\text{C}$ and $\Delta T_{\text{sub}} = 10 \text{ K}$ with R134a in the $H = 756 \text{ }\mu\text{m}$ test section with and without the orifice insert. Among ten thermocouples, only two measurements at 5 mm and 15 mm from the front edge of the heater are shown for clarity. Empty symbols are for the values measured without the orifice while filled symbols are for the values measured with the orifice. As the heat flux was increased, the wall temperature increased more or less linearly until it had a sufficient superheating to initiate boiling. When boiling occurred at around 25 W/cm^2 , the wall temperature dropped due to the higher heat transfer mechanism of two phase flow boiling. Since the orifice caused an additional pressure drop, the subcooling of the fluid was reduced at the actual inlet of the channel in the case with the orifice. Consequently, boiling incipience occurred at a lower heat flux. This has an advantage of reducing unnecessary overshoot of wall temperature in a two phase cooling device. The high heat transfer coefficient began to decrease at a heat flux of 80 W/cm^2 in the case without the orifices and at 100 W/cm^2 with the orifices. The flatter trend in the boiling curves can be attributed to local intermittent dry out in the channels. At a higher heat flux of 140 W/cm^2 , the wall temperature increased over $100 \text{ }^\circ\text{C}$ without the orifices while the wall temperature was only $60 \text{ }^\circ\text{C}$ in the case with the orifices.

The flow boiling curves suggest that in the case without the orifices, the flow is easily subjected to instability and mal-distribution, and can cause CHF to occur earlier than what it would with the orifices.

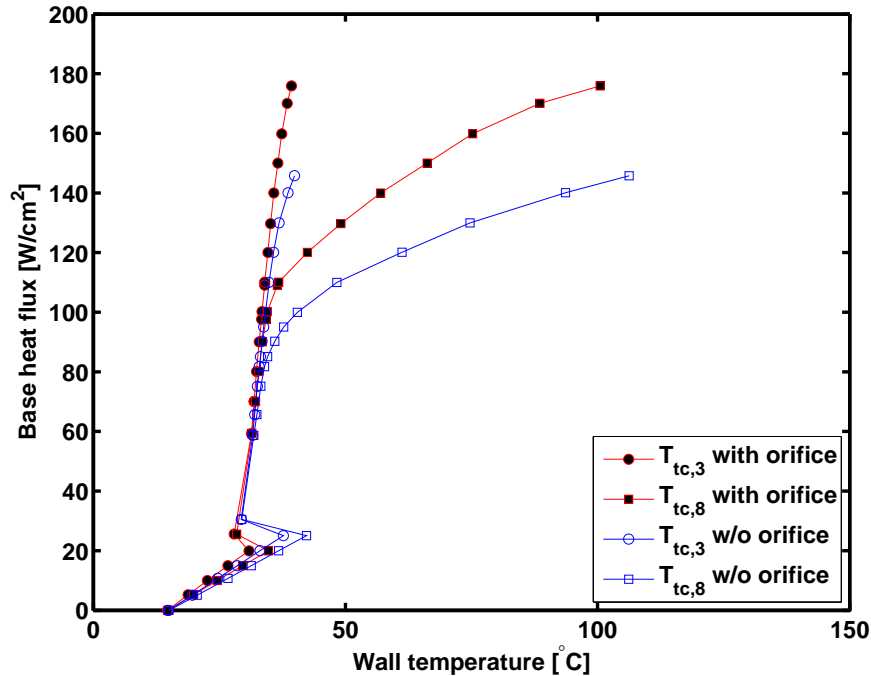


Figure 7.9: Flow boiling curves at $G = 2000 \text{ kg/m}^2\text{s}$, $T_{\text{sat}} = 25 \text{ }^\circ\text{C}$ and $\Delta T_{\text{sub}} = 10 \text{ K}$ with R134a in $H = 756 \text{ }\mu\text{m}$ channels with and without the orifice.

Comparison of CHF results

Figure 7.10 shows wall CHF versus subcooling at $T_{\text{sat}} = 50^\circ\text{C}$ with R245fa in the $H = 4052\ \mu\text{m}$ test section. Again, the empty symbols are the values measured without the orifices while the filled symbols are with the orifices. At a mass velocity of $215\ \text{kg/m}^2\text{s}$, wall CHF was observed to increase with increasing subcooling when using the orifices, as explained also in the previous parameter study. On the contrary, wall CHF decreased with increasing subcooling in the case of removing the orifice insert. At a lower mass velocity, the subcooling had no effect. Except for the case of $5\ \text{K}$ subcooling at $215\ \text{kg/m}^2\text{s}$, the wall CHF values measured with orifices were always higher than those without the orifices.

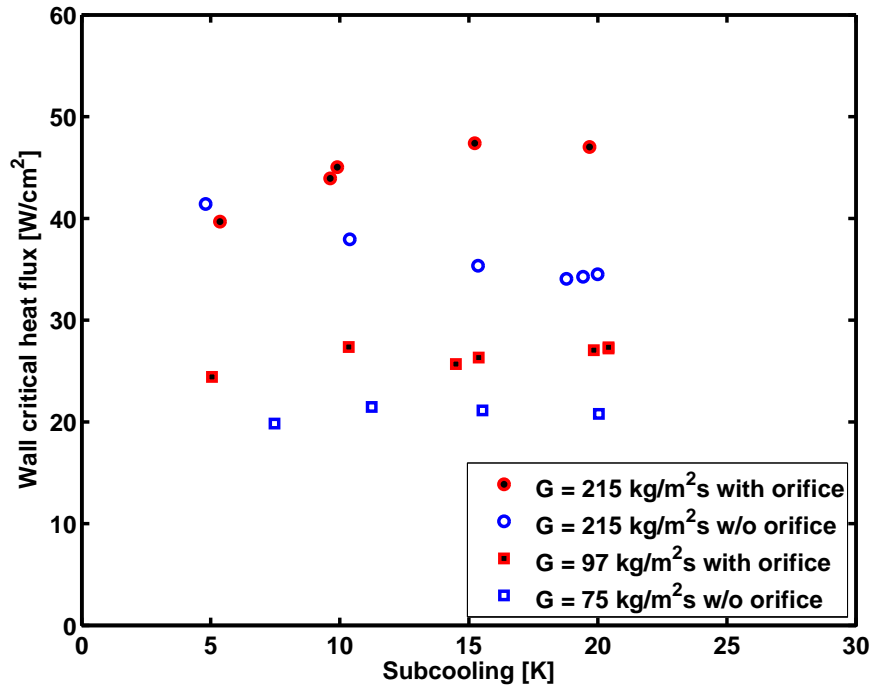


Figure 7.10: Wall CHF versus subcooling at $T_{\text{sat}} = 50^\circ\text{C}$ with R245fa in $H = 4052\ \mu\text{m}$ channels with and without the orifice.

Figure 7.11 compares the effect of inlet orifices on wall CHF measured at $T_{\text{sat}} = 25^\circ\text{C}$ with R134a in the $H = 756\ \mu\text{m}$ test section. In both cases measured with and without the orifices, the wall CHF was observed not to be affected by the level of subcooling. However, at the mass velocity of $1880\ \text{kg/m}^2\text{s}$, the wall CHF measured with the orifices was almost 20% higher than that measured without the orifices at the same flow condition. On the other hand, at a mass velocity of $390\ \text{kg/m}^2\text{s}$, no evident difference was observed between the two cases.

In Figure 7.12, the wall CHF is plotted versus the mass velocity at $T_{\text{sat}} = 25^\circ\text{C}$ and $\Delta T_{\text{sub}} = 5\ \text{K}$ with R134a in $H = 756\ \mu\text{m}$ channels. Generally, the wall CHF measured with orifices was higher than that measured without orifices. While no enhancement of the wall CHF occurs at low mass velocities, the difference between the two cases increases at higher mass velocities.

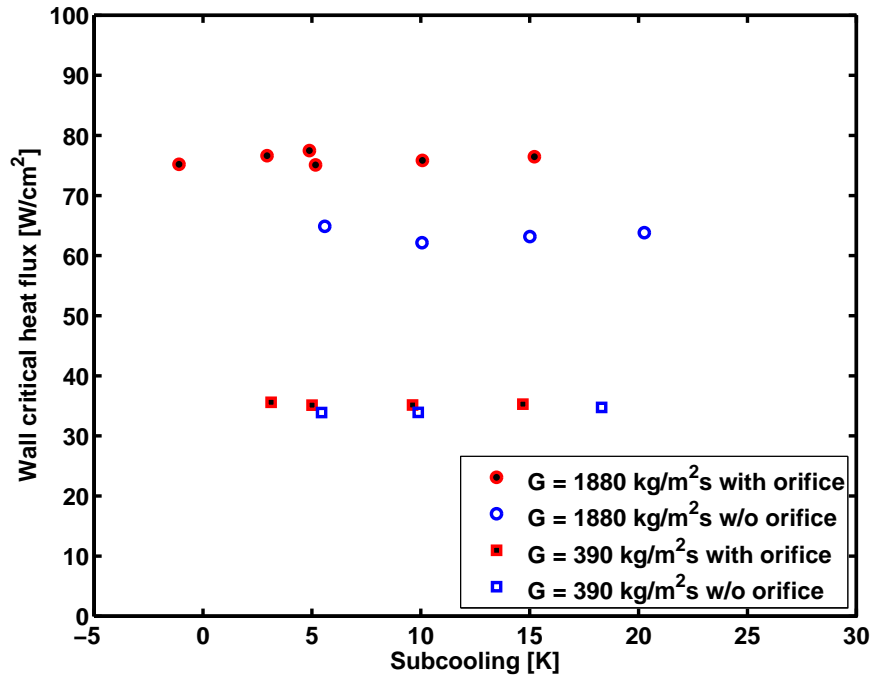


Figure 7.11: Wall CHF versus subcooling at $T_{\text{sat}} = 25 \text{ }^\circ\text{C}$ with R134a in $H = 756 \text{ }\mu\text{m}$ channels with and without the orifice.

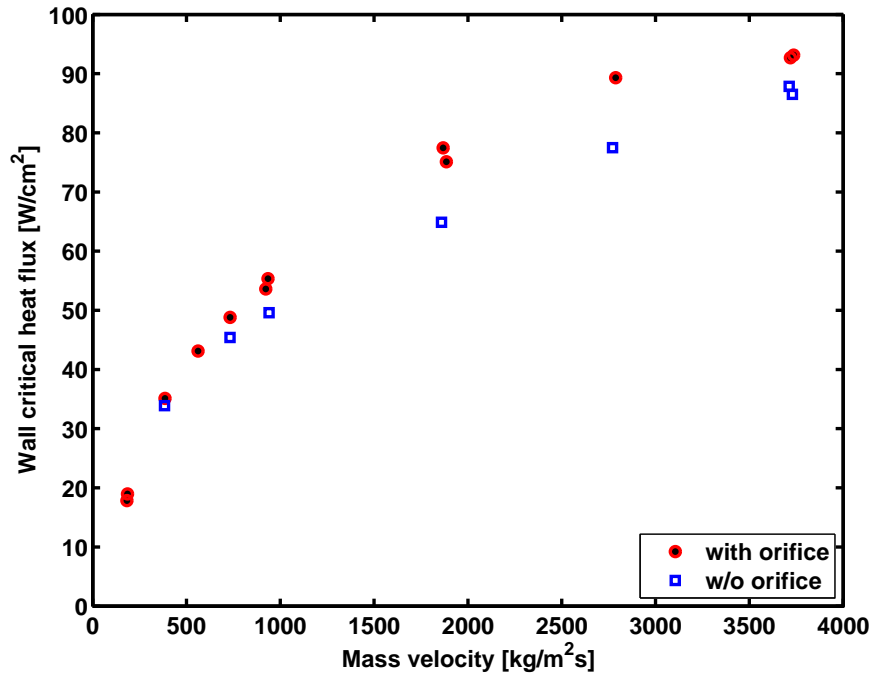


Figure 7.12: Wall CHF versus mass velocity at $T_{\text{sat}} = 25 \text{ }^\circ\text{C}$ and $\Delta T_{\text{sub}} = 5 \text{ K}$ with R134a in $H = 756 \text{ }\mu\text{m}$ channels with and without the orifice.

7.4 Conclusions

Flow visualizations were conducted with a high speed video for the two multi-microchannel heat sinks tested in the present study. Visualization confirmed the existence of flow instability, back flow and non-uniform distribution of flow along the channels when no inlet orifices were used. On the other hand, when the inlet orifice insert was installed, all the channels showed similar flow patterns, bubble mixture region lengths and apparently uniform flow coming out of the channel, implying that the flow was uniformly distributed.

However, due to the existence of the inlet orifices, the flow inside the channels behaved differently. Flow recirculation was observed at the inlet of the channels, which resulted from blocking the back flow in these high aspect ratio channels. With increasing heat flux, this recirculation flow forms an elongated vapor zone in the adiabatic zone of the test section so that the highly subcooled inlet flow forms a liquid jet stream to pass through the vapor trapping zone.

Flow boiling curves and CHF results in both the configurations were compared in a quantitative analysis. Since the orifices caused an additional pressure drop and consequent reduction of subcooling, flow boiling occurred at a lower heat flux. This has an advantage of reducing the unnecessary overshoot of wall temperature in a two phase cooling device. In the case of removing the orifice insert, the flow was easily subjected to instability and caused CHF to occur earlier than with inlet orifices except at very low mass velocities.

Chapter 8

General Conclusions

A new versatile test facility was built for multi-microchannel CHF tests in this study. A large range of test conditions were investigated, targeting computer chip cooling applications. Three low pressure refrigerants, R134a, R236fa and R245fa, were tested as coolants in test sections of height of 4052 μm and 756 μm with aspect ratios of 8.7 and 3.8, respectively. The new database, comprised of 323 new saturated CHF data points, provided the following key findings:

1. Different trends of flow boiling curves were found and analyzed in order to choose the proper CHF distinguishing criterion. The first type of flow boiling curves depicted a steady rise in the wall temperature with heating power, until a sudden temperature jump occurs. In the second type, a sudden but small temperature jump occurs frequently at medium heat fluxes until a distinct excursion takes place over a cut-off threshold at higher temperature values. The third type of flow boiling curves depicted no spike in the wall temperature, but rose steadily to the maximum imposed limit, thus the power was shut off to avoid burn out of the heater. The heat transfer coefficient was reduced significantly at stable heat fluxes just prior to CHF, indicating the occurrence of partial and intermittent dry out.
2. The effect of input parameters was analyzed from the acquired database. CHF increased with increasing mass velocity but the rate of rise lessened at higher mass velocities. CHF increased moderately with large subcooling in the $H = 4052 \mu\text{m}$ channels. However, subcooling appeared to play less of a role as the channel size decreased. Among the refrigerants tested, R134a showed higher performance than R236fa and R245fa as a cooling fluid with respect to CHF and pressure drop. CHF showed reversed tendency with increasing system pressure for the two test section, which is attributed to the adverse effects of other key parameters related to the system pressure.
3. The experimental data were compared to prediction methods in the literature. Since many of the prediction methods were based on circular channel data, defining an equivalent diameter and a mass velocity was necessary to implement these methods for the current rectangular channels. Comparing the present results to the prediction methods, the mean absolute errors (MAE) using different definitions for the diameter and mass velocity were computed. The best outcome resulted when using the combination of the heated equivalent diameter D_{he} , which reflects the actual heat transfer conditions of three heated sides, and the actual mass velocity G_{eq} . Notably, using the traditional hydraulic diameter D_h and mass flux calculated using this diameter's cross-sectional area always gave the worst results.

4. Five prediction methods, including one theoretical numerical method, were compared with the experimental data. Using the heated equivalent diameter D_{he} and the actual mass velocity G_{eq} , the data generally matched well with the predictions of Katto and Ohno [22], Wojtan et al. [46] and Revellin and Thome [37]. The data for the smaller channel, $H = 756 \mu\text{m}$, matched extremely well with the predictions of Wojtan et al. [46]. The numerical method [37], which considers the evolution of film thickness and wave height, also showed very promising results for microchannel CHF regardless of the aspect ratio and for all three fluids.
5. Flow visualization was conducted with a high speed video. The effect of inlet orifices was investigated using a removable metal piece with holes for each channel inlet. Visualizations confirmed the existence of flow instability, back flow and non-uniform flow among the channels when the orifice insert was removed. On the other hand, when adopting the inlet orifice insert, all the channels showed similar flow patterns and a uniform exiting flow implying a good distribution.
6. In the case of using the orifice insert, the flow inside the channels behaves differently due to the existence of the inlet orifice. Since the orifice blocks back flow, flow recirculation was observed near the inlet in the high aspect ratio case. With increasing heat flux, the recirculating bubbles merged to form an elongated vapor bubble and the highly subcooled inlet flow became a liquid jet stream to cutting through a volume occupied by the vapor phase.
7. Flow boiling curves and CHF data in the case with and without orifices were compared for a quantitative analysis. Since the orifice caused additional pressure drop, the subcooling of the fluid was reduced at the inlet to the channels. Consequently, boiling incipience occurred at a lower heat flux, yielding a reduction in the wall temperature overshoot. When the orifice insert was removed, the flow was easily subjected to instability, presenting lower values of CHF than those with the orifice insert in place.

The new extensive CHF database and visual understanding obtained in this thesis are particularly valuable for designing of high heat flux, two-phase cooling devices.

From the results of the current research, a new method can be sought to reach higher CHF. One example is to connect the flow inlet to the middle of the channels for a split flow configuration. This would decrease the heated length by a half and an equivalent CHF may be reached at lower mass velocities. Experimentation in such a configuration is currently under way in the same laboratory in another Ph.D thesis. Further study is also recommended to investigate the effect of different aspect ratio channels, as well as the effect of different orifice sizes and shape.

Appendix A

CHF database

For the reader's reference, all the CHF data acquired are presented in this appendix. All the basic parameters are listed so that they can be used to calculate the other parameters for further analysis. The summary of the test conditions and the number of data acquired were listed in Table A.1.

Table A.1: Range of test conditions and the number of data points acquired

Channel geometry $W \times H(\mu\text{m})$	Fluid	Saturation temperature (°C)	Mass velocity (kg/m ² s)	Inlet subcooling (K)	No. of data
467×4052	R245fa	25-50	90-230	0-24	68
	R236fa	20-35	100-300	3-20	54
	R134a	10-30	100-450	3-20	60
199×756	R245fa	25-50	200-2400	0-15	38
	R236fa	15-40	200-3000	0-15	57
	R134a	15-25	200-4000	0-15	46

No.	Test section H[μ m]	Fluid	$T_{\text{sat,in}}$ [C]	G [kg/m ² s]	ΔT_{sub} [K]	CHF,b [W/cm ²]	CHF,w [W/cm ²]
1	756	245	25.2	188.1	5.1	44.8	18.5
2	756	245	25.0	298.0	4.7	71.4	29.5
3	756	245	26.9	376.0	15.0	80.7	33.4
4	756	245	25.7	397.5	10.1	83.8	34.7
5	756	245	25.4	377.3	5.4	81.3	33.7
6	756	245	24.6	393.3	-1.1	82.9	34.4
7	756	245	25.7	491.7	6.5	89.9	37.3
8	756	245	25.6	548.2	5.2	95.9	39.9
9	756	245	25.1	646.9	3.7	100.3	41.8
10	756	245	25.1	730.7	9.4	103.9	43.2
11	756	245	25.4	709.7	6.6	105.0	43.7
12	756	245	24.8	743.0	-0.2	109.3	45.6
13	756	245	50.7	192.7	5.2	46.2	19.1
14	756	245	50.1	382.9	16.1	63.4	26.3
15	756	245	50.1	380.5	9.9	62.3	25.9
16	756	245	49.9	376.2	6.5	64.5	26.8
17	756	245	50.2	567.6	5.0	78.4	32.9
18	756	245	50.2	740.6	15.5	83.2	34.7
19	756	245	50.2	740.9	9.7	84.7	35.5
20	756	245	50.1	741.0	7.0	85.2	35.7
21	756	245	50.1	1120.3	5.2	103.2	43.6
22	756	245	50.1	1499.0	15.0	120.5	50.7
23	756	245	50.1	1496.5	9.8	119.4	50.4
24	756	245	50.1	1498.5	4.8	120.0	50.9
25	756	245	50.3	2226.9	5.4	154.4	65.9
26	756	245	29.6	380.5	4.7	79.5	33.0
27	756	245	34.7	377.9	5.2	76.7	31.8
28	756	245	39.9	382.6	5.7	73.6	30.6
29	756	245	45.0	381.6	4.8	70.8	29.4
30	756	245	31.5	755.8	6.8	102.8	42.9
31	756	245	35.1	768.4	5.2	102.1	42.7
32	756	245	40.5	740.2	5.4	95.7	40.1
33	756	245	45.2	739.5	4.6	91.9	38.6
34	756	245	31.2	738.1	10.8	98.8	41.1
35	756	245	35.4	759.5	10.4	97.3	40.5
36	756	245	39.7	748.1	12.3	91.3	38.1
37	756	245	44.9	745.9	9.8	87.7	36.6
38	756	245	44.6	1520.8	4.4	125.2	52.9
39	756	236	24.9	197.9	4.6	36.8	15.2
40	756	236	25.0	188.7	5.4	36.5	15.1
41	756	236	25.0	389.6	15.0	74.6	30.9
42	756	236	25.0	369.5	9.9	68.5	28.4
43	756	236	25.0	382.2	4.8	70.2	29.1
44	756	236	25.0	392.6	5.0	74.6	30.9
45	756	236	25.0	379.4	0.4	72.1	29.9
46	756	236	25.0	389.7	5.3	73.8	30.6
47	756	236	24.9	399.8	5.6	64.0	26.6
48	756	236	25.0	565.4	5.2	90.3	37.5
49	756	236	25.1	751.9	14.9	96.6	40.1
50	756	236	25.1	746.7	9.7	101.1	42.1

No.	Test section H[μm]	Fluid	$T_{\text{sat,in}}$ [C]	G [kg/m ² s]	ΔT_{sub} [K]	CHF,b [W/cm ²]	CHF,w [W/cm ²]
51	756	236	25.0	745.4	5.0	95.3	39.8
52	756	236	25.1	743.9	0.3	97.8	40.9
53	756	236	25.1	746.5	14.7	96.6	40.1
54	756	236	25.0	756.0	9.8	100.3	41.7
55	756	236	25.1	756.2	5.3	102.1	42.6
56	756	236	25.0	738.9	0.1	102.5	42.8
57	756	236	25.1	920.2	5.1	112.4	47.1
58	756	236	25.0	1507.4	14.9	127.0	53.0
59	756	236	25.1	1512.3	10.0	129.2	54.1
60	756	236	25.1	1475.1	5.0	132.2	55.5
61	756	236	25.0	1487.1	5.0	128.1	53.9
62	756	236	34.9	197.3	4.1	42.8	17.6
63	756	236	35.0	187.5	5.1	40.0	16.5
64	756	236	35.0	380.2	15.0	70.9	29.3
65	756	236	35.0	386.5	10.0	71.1	29.5
66	756	236	35.0	379.7	5.2	68.8	28.5
67	756	236	34.9	359.4	0.5	68.3	28.3
68	756	236	35.0	560.7	5.0	84.0	35.0
69	756	236	35.0	755.5	15.0	92.3	38.4
70	756	236	35.1	741.3	9.9	92.4	38.5
71	756	236	35.0	743.1	5.6	94.8	39.6
72	756	236	34.8	749.1	1.0	97.9	41.0
73	756	236	35.0	745.8	4.9	94.2	39.4
74	756	236	35.1	940.6	5.1	104.0	43.7
75	756	236	35.0	1508.8	15.0	123.1	51.6
76	756	236	35.0	1491.7	10.0	121.7	51.2
77	756	236	35.1	1502.6	5.1	124.6	52.6
78	756	236	35.2	1481.5	0.4	129.1	54.7
79	756	236	35.0	2226.0	5.1	145.0	61.4
80	756	236	35.3	2776.8	5.3	156.8	66.5
81	756	236	14.6	388.3	4.4	68.5	28.4
82	756	236	19.8	375.5	4.0	65.1	27.0
83	756	236	25.0	380.5	4.8	70.2	29.1
84	756	236	30.0	378.1	5.0	70.1	29.0
85	756	236	40.0	379.9	4.7	66.5	27.6
86	756	236	14.5	737.1	4.3	107.4	44.7
87	756	236	19.9	759.0	5.3	106.3	44.3
88	756	236	29.9	739.1	5.7	97.8	40.8
89	756	236	39.9	727.5	5.4	90.7	38.0
90	756	236	14.5	752.7	4.9	107.8	44.9
91	756	236	19.8	761.7	10.1	103.8	43.1
92	756	236	30.0	748.1	9.7	98.4	41.0
93	756	236	39.9	747.2	9.7	88.3	36.9
94	756	236	30.1	1505.4	5.0	130.0	54.7
95	756	236	40.0	1491.1	5.0	120.8	51.1
96	756	134	15.0	205.8	3.5	56.2	23.1
97	756	134	15.2	383.2	8.8	88.8	36.9
98	756	134	15.1	381.9	5.1	89.3	37.2
99	756	134	15.2	390.0	2.7	88.0	36.6
100	756	134	15.0	563.1	5.0	110.0	46.1

No.	Test section H[μ m]	Fluid	$T_{\text{sat,in}}$ [C]	G [kg/m ² s]	ΔT_{sub} [K]	CHF,b [W/cm ²]	CHF,w [W/cm ²]
101	756	134	15.0	732.2	10.0	124.4	52.2
102	756	134	15.1	755.4	5.0	126.7	53.4
103	756	134	15.0	743.5	3.0	127.1	53.6
104	756	134	14.9	976.5	9.9	137.7	58.0
105	756	134	15.0	970.9	5.2	139.3	59.0
106	756	134	15.0	927.2	3.0	138.3	58.5
107	756	134	15.0	1855.4	10.0	177.9	75.7
108	756	134	15.0	1857.0	5.0	178.9	76.5
109	756	134	15.0	1859.8	3.0	179.1	76.7
110	756	134	15.0	1876.6	5.1	175.3	74.9
111	756	134	14.9	2790.2	9.8	207.0	88.6
112	756	134	15.0	2781.5	5.0	207.2	89.1
113	756	134	15.1	2725.0	2.9	207.0	89.2
114	756	134	24.9	186.5	5.0	45.7	19.0
115	756	134	24.8	182.7	4.8	43.0	17.9
116	756	134	24.9	387.7	14.7	84.9	35.3
117	756	134	24.9	385.2	9.6	84.4	35.1
118	756	134	24.9	385.6	5.0	84.1	35.1
119	756	134	25.0	408.8	3.1	85.2	35.6
120	756	134	25.0	561.5	5.0	102.7	43.1
121	756	134	25.0	746.0	14.9	116.2	48.9
122	756	134	25.0	747.7	10.1	107.7	45.5
123	756	134	25.0	732.4	5.0	115.4	48.8
124	756	134	25.0	735.8	2.9	117.1	49.6
125	756	134	25.0	934.7	5.0	130.3	55.3
126	756	134	25.0	935.9	15.1	130.0	54.8
127	756	134	25.0	946.4	10.1	130.9	55.4
128	756	134	25.0	934.3	2.9	130.4	55.5
129	756	134	25.0	923.1	5.2	126.5	53.6
130	756	134	25.2	1885.9	5.2	174.2	75.1
131	756	134	25.1	1881.7	15.2	179.1	76.5
132	756	134	24.9	1892.5	10.1	176.7	75.9
133	756	134	24.9	1868.4	4.9	179.8	77.5
134	756	134	25.0	1864.7	2.9	177.4	76.6
135	756	134	25.0	1876.9	-1.1	174.1	75.2
136	756	134	25.0	2788.4	5.0	205.8	89.3
137	756	134	25.0	2800.0	3.0	206.1	89.7
138	756	134	25.0	2789.6	15.1	203.7	87.2
139	756	134	25.1	2816.6	10.1	201.7	86.8
140	756	134	25.0	3718.9	5.2	213.6	92.7
141	756	134	25.1	3736.1	5.1	215.0	93.1
142	4052	245	26.2	95.3	10.0	159.4	26.5
143	4052	245	25.8	95.1	9.8	153.2	25.2
144	4052	245	24.0	84.0	-0.1	147.0	20.9
145	4052	245	24.2	87.5	2.3	141.3	19.5
146	4052	245	24.2	88.6	2.8	139.3	19.1
147	4052	245	24.1	88.8	2.2	135.2	18.4
148	4052	245	24.1	91.5	8.4	140.0	22.4
149	4052	245	24.1	90.6	7.7	142.4	21.8
150	4052	245	26.2	94.0	9.2	160.6	25.6

No.	Test section H[μm]	Fluid	$T_{\text{sat,in}}$ [C]	G [kg/m ² s]	ΔT_{sub} [K]	CHF,b [W/cm ²]	CHF,w [W/cm ²]
151	4052	245	26.4	90.9	9.2	172.2	26.2
152	4052	245	26.5	92.0	1.3	159.1	25.5
153	4052	245	26.7	89.2	5.9	166.6	27.0
154	4052	245	50.1	96.1	5.0	165.2	24.4
155	4052	245	50.6	100.2	5.8	166.4	24.6
156	4052	245	50.1	97.7	20.4	183.7	27.3
157	4052	245	50.3	96.6	19.8	179.2	27.0
158	4052	245	50.1	97.9	20.4	182.0	27.2
159	4052	245	50.0	96.9	15.4	178.0	26.3
160	4052	245	50.2	95.8	14.5	176.9	25.7
161	4052	245	50.6	102.8	20.5	184.4	30.0
162	4052	245	50.2	99.2	15.4	185.4	28.5
163	4052	245	50.2	97.8	10.3	182.8	27.4
164	4052	245	46.7	159.8	12.6	229.1	36.2
165	4052	245	50.1	142.5	15.1	250.2	39.5
166	4052	245	49.9	141.2	9.9	227.8	37.2
167	4052	245	50.1	139.7	5.0	200.0	31.8
168	4052	245	49.5	193.6	21.0	272.1	45.0
169	4052	245	49.7	202.0	19.3	269.1	44.5
170	4052	245	49.6	189.4	14.5	236.3	36.7
171	4052	245	50.2	212.1	15.2	290.3	47.4
172	4052	245	50.1	211.6	9.9	275.4	45.0
173	4052	245	50.1	211.6	9.6	273.1	43.9
174	4052	245	49.8	209.0	19.8	297.9	48.4
175	4052	245	49.8	212.4	19.7	295.8	47.0
176	4052	245	50.0	214.5	5.4	253.5	39.7
177	4052	245	50.2	219.4	15.5	277.8	46.5
178	4052	245	50.1	218.4	15.4	277.5	46.3
179	4052	245	49.9	217.1	16.5	282.3	46.0
180	4052	245	50.5	198.1	14.0	247.0	39.7
181	4052	245	49.8	193.5	14.6	244.2	39.1
182	4052	245	49.9	189.0	14.4	244.4	39.1
183	4052	245	50.1	189.5	10.2	229.2	36.7
184	4052	245	49.6	187.1	4.1	198.2	31.8
185	4052	245	49.5	188.8	5.0	192.7	30.6
186	4052	245	50.4	186.2	5.5	197.1	31.6
187	4052	245	32.6	94.5	4.3	161.2	23.1
188	4052	245	32.7	95.3	4.0	159.4	22.5
189	4052	245	29.3	113.1	15.6	165.2	25.4
190	4052	245	29.2	114.6	15.9	164.1	25.0
191	4052	245	29.4	114.2	12.0	161.5	23.1
192	4052	245	29.2	114.8	12.8	160.0	24.8
193	4052	245	29.6	111.0	6.4	156.9	22.5
194	4052	245	29.7	115.4	6.3	154.1	21.7
195	4052	245	29.0	115.4	20.8	169.9	25.9
196	4052	245	28.9	113.6	21.2	169.9	25.8
197	4052	245	30.3	115.2	3.3	158.6	22.5
198	4052	245	30.2	116.8	3.1	153.9	21.5
199	4052	245	31.0	118.2	17.4	184.9	31.2
200	4052	245	32.6	124.3	23.9	197.2	33.0

No.	Test section H[μ m]	Fluid	$T_{\text{sat,in}}$ [C]	G [kg/m ² s]	ΔT_{sub} [K]	CHF,b [W/cm ²]	CHF,w [W/cm ²]
201	4052	245	32.7	127.1	24.0	194.3	32.6
202	4052	245	32.7	131.5	10.2	166.0	27.9
203	4052	245	32.7	131.9	9.2	162.6	27.4
204	4052	245	32.7	132.6	9.1	160.2	26.6
205	4052	245	32.7	130.9	9.2	165.5	27.3
206	4052	245	32.7	131.3	11.1	168.0	28.4
207	4052	245	43.2	190.3	8.8	199.3	29.8
208	4052	245	42.8	191.6	8.7	191.2	25.9
209	4052	245	45.0	193.5	19.8	250.8	42.3
210	4052	236	25.2	95.2	3.3	121.4	19.9
211	4052	236	25.1	96.2	5.1	124.9	20.6
212	4052	236	25.2	93.4	10.0	135.6	20.4
213	4052	236	25.1	97.6	15.2	143.7	22.0
214	4052	236	25.1	97.8	20.8	157.0	24.0
215	4052	236	25.0	113.6	20.1	177.6	27.4
216	4052	236	25.0	115.4	15.0	174.3	26.6
217	4052	236	25.0	112.4	10.0	153.1	22.5
218	4052	236	25.0	114.0	5.1	143.0	21.1
219	4052	236	25.0	113.4	3.0	140.5	21.0
220	4052	236	25.2	139.4	20.1	188.1	29.4
221	4052	236	25.0	146.1	14.8	160.7	27.6
222	4052	236	25.1	141.8	10.0	150.8	24.2
223	4052	236	25.0	140.4	5.2	126.8	21.7
224	4052	236	25.0	141.6	3.4	127.0	20.5
225	4052	236	25.0	163.3	20.1	197.2	31.2
226	4052	236	25.1	161.9	15.0	182.3	28.3
227	4052	236	25.1	160.4	10.2	161.2	24.9
228	4052	236	25.0	154.8	4.9	123.9	19.9
229	4052	236	25.0	156.2	3.2	130.0	20.0
230	4052	236	25.0	189.4	20.0	174.1	29.7
231	4052	236	25.0	189.2	15.0	158.8	27.1
232	4052	236	25.0	189.3	10.2	153.3	24.4
233	4052	236	25.1	183.6	5.1	142.1	21.8
234	4052	236	25.0	182.3	3.1	136.2	21.2
235	4052	236	34.9	99.8	19.9	162.7	25.2
236	4052	236	35.0	99.9	15.3	158.3	24.1
237	4052	236	34.7	99.4	10.0	148.4	22.6
238	4052	236	35.1	99.8	10.5	154.6	22.1
239	4052	236	34.8	99.0	4.9	149.1	21.1
240	4052	236	35.1	143.5	20.0	210.1	31.1
241	4052	236	35.0	141.8	15.2	199.0	29.5
242	4052	236	35.1	144.6	10.3	186.1	27.9
243	4052	236	34.8	142.6	5.7	131.5	23.9
244	4052	236	35.2	190.8	20.2	231.3	35.5
245	4052	236	35.1	190.3	15.1	217.0	33.4
246	4052	236	35.1	189.7	10.1	201.5	30.8
247	4052	236	34.9	188.6	4.9	180.0	27.6
248	4052	236	35.0	234.1	20.5	221.9	39.1
249	4052	236	35.2	237.7	15.5	201.7	36.5
250	4052	236	34.5	244.8	9.6	177.4	31.9

No.	Test section H[μm]	Fluid	$T_{\text{sat,in}}$ [C]	G [kg/m ² s]	ΔT_{sub} [K]	CHF,b [W/cm ²]	CHF,w [W/cm ²]
251	4052	236	34.6	244.0	9.8	177.9	32.2
252	4052	236	34.6	244.8	9.9	176.3	32.3
253	4052	236	35.1	236.3	5.0	192.0	29.3
254	4052	236	35.2	291.0	20.3	214.4	36.7
255	4052	236	35.0	288.0	15.0	200.4	35.1
256	4052	236	35.2	286.4	10.3	189.2	33.7
257	4052	236	35.5	286.4	5.3	173.1	31.7
258	4052	236	19.8	142.3	5.0	118.2	20.6
259	4052	236	25.2	141.6	5.4	136.2	22.3
260	4052	236	30.0	142.5	5.1	161.8	24.3
261	4052	236	35.0	146.5	5.6	167.6	25.6
262	4052	236	25.0	176.7	5.1	144.7	21.6
263	4052	236	25.0	183.6	5.1	151.9	23.2
264	4052	134	15.0	96.2	13.8	196.7	33.6
265	4052	134	15.0	94.9	10.0	184.1	32.8
266	4052	134	15.0	96.2	5.0	174.3	26.6
267	4052	134	14.9	95.3	2.9	166.3	25.2
268	4052	134	15.0	142.1	14.9	242.7	38.4
269	4052	134	15.0	140.8	10.0	233.8	36.2
270	4052	134	15.0	143.3	4.9	210.0	33.2
271	4052	134	15.0	142.2	3.0	198.4	34.8
272	4052	134	15.2	189.2	15.1	277.7	45.4
273	4052	134	15.2	188.8	10.1	260.5	42.0
274	4052	134	15.1	189.4	5.0	239.2	37.7
275	4052	134	15.1	188.6	3.0	225.0	36.0
276	4052	134	15.1	237.2	15.1	294.7	50.8
277	4052	134	15.0	236.4	10.0	280.1	45.8
278	4052	134	15.0	234.2	5.0	259.2	43.2
279	4052	134	15.0	237.8	3.0	252.1	41.8
280	4052	134	15.1	285.0	15.1	279.9	55.1
281	4052	134	15.1	283.4	10.1	275.7	48.5
282	4052	134	15.1	285.2	5.2	257.5	45.6
283	4052	134	15.1	285.2	3.0	250.4	40.1
284	4052	134	15.0	284.0	2.9	251.4	42.3
285	4052	134	15.0	313.7	10.0	260.6	51.1
286	4052	134	15.0	311.2	4.8	251.0	45.0
287	4052	134	15.1	335.8	5.0	239.7	48.6
288	4052	134	25.1	98.8	19.9	199.2	34.8
289	4052	134	25.1	96.7	15.0	192.3	34.1
290	4052	134	25.1	96.7	10.1	187.4	34.0
291	4052	134	25.1	96.3	5.0	178.1	28.8
292	4052	134	25.0	94.2	3.1	169.9	27.5
293	4052	134	25.0	105.9	5.2	189.7	32.6
294	4052	134	25.0	145.5	19.9	261.4	47.8
295	4052	134	25.0	144.3	14.9	255.1	46.5
296	4052	134	25.0	144.9	9.9	252.1	44.6
297	4052	134	25.0	143.1	5.0	237.1	39.0
298	4052	134	25.1	141.6	3.0	233.8	38.0
299	4052	134	25.1	190.4	20.0	303.0	57.6
300	4052	134	25.1	190.2	15.1	294.7	52.5

No.	Test section H[μ m]	Fluid	$T_{\text{sat,in}}$ [C]	G [kg/m ² s]	ΔT_{sub} [K]	CHF,b [W/cm ²]	CHF,w [W/cm ²]
301	4052	134	25.0	189.8	10.0	280.9	48.0
302	4052	134	25.1	189.4	5.0	266.9	44.2
303	4052	134	25.0	188.5	3.0	262.8	43.5
304	4052	134	25.0	287.3	20.0	335.9	57.0
305	4052	134	25.0	285.8	15.0	319.0	53.6
306	4052	134	25.1	283.9	15.1	325.9	55.8
307	4052	134	25.0	287.2	9.9	307.1	51.9
308	4052	134	25.0	284.4	5.0	287.6	49.4
309	4052	134	25.0	283.8	3.0	286.2	49.6
310	4052	134	25.0	332.6	20.1	338.8	56.8
311	4052	134	25.1	380.1	20.0	341.9	57.1
312	4052	134	25.1	379.7	15.1	320.2	53.1
313	4052	134	25.0	380.3	10.0	298.9	49.8
314	4052	134	25.0	382.5	5.0	284.2	48.5
315	4052	134	25.0	378.1	5.0	294.1	50.8
316	4052	134	25.0	379.8	3.0	279.3	47.4
317	4052	134	24.9	428.9	19.8	330.7	54.8
318	4052	134	10.1	189.1	5.0	225.9	35.1
319	4052	134	15.0	190.7	5.0	241.4	39.2
320	4052	134	20.1	190.9	5.1	253.4	42.9
321	4052	134	25.1	192.6	5.1	260.4	44.6
322	4052	134	29.1	211.2	13.5	311.2	55.6
323	4052	134	30.1	191.8	5.0	265.4	47.2

Table A.2: Presentation of CHF database

Appendix B

Step-by-step procedures for uncertainty analysis

The ASME standard [4] provides a systematic procedure for uncertainty analysis and helps to determine the most critical error source, thus reducing the total uncertainty. This standard is in harmony with the ISO Guide [18] even though they use different error classifications. The step-by-step calculation procedures from chapter 9 of ASME PTC-19.1 are listed as below:

1. Define the Measurement Process
 - Review test objectives and test duration
 - List all independent measurement parameters and their nominal levels
 - List all calibrations and instrument setups
 - Define the functional relationship between the parameters and results
2. List the Elemental Uncertainty Sources
3. Calculate the Systematic and Random standard deviation
4. Propagate the Systematic and Random standard deviation
5. Calculate the Uncertainty

1. Define the Measurement Process

- Review test objectives and test duration

The objective of this test is to analyze flow boiling heat transfer in multi-micro channels. Temperature and pressure are measured at several locations in the test section and processed to obtain test results, such as the heat transfer coefficient and CHF.

Obtaining one CHF data point at each flow condition takes typically 1-2 hours. Power was applied in small increments and the system was allowed to stabilize even though a strict steady state was not necessarily maintained. The experimental data were collected over a year with three fluids in two sections. The repeatability of the measurement was found to be acceptable during this period.

Table B.1: The main independent measurement parameters and their nominal values.

Symbol	Description	Unit	Nominal Value
T_{in}	Inlet fluid temperature	$^{\circ}\text{C}$	20.1
T_{o}	Outlet fluid temperature	$^{\circ}\text{C}$	18.5
p_{in}	Inlet pressure	bar	2.73
p_{o}	Outlet pressure	bar	2.18
Q	Heating power	W	529
\dot{M}	Mass flow rate	kg/h	23.2
T_{w}	Wall temperature	$^{\circ}\text{C}$	76.8
A_{h}	Heating area	cm^2	4
W_{ch}	Channel width	μm	199
H_{f}	Channel height	μm	756
z	Distance from heater front	mm	9

- List all independent measurement parameters and their nominal levels

The main independent measurement parameters needed to compute the local wall heat flux are listed in Table B.1. These include the fluid and wall temperature, the inlet and outlet pressure, heating power, mass flow rate and the dimensions of the geometries.

- List all calibrations and instrument setups

All the measurement systems were calibrated before installation. The thermocouples and pressure transducers were calibrated with the data acquisition cards connected and have measured uncertainties of $\pm 0.1^{\circ}\text{C}$ and ± 10 mbar, respectively. The input heating power from the voltage and current measurement has an uncertainty of ± 0.02 W. The Coriolis mass flow meter has an uncertainty of $\pm 0.1\%$.

- Define the functional relationship between the parameters and results

The wall heat flux cannot be measured directly, therefore it has to be calculated from a functional relationship of the measured parameters. In addition to such results, some parameters also have to be determined from other measured parameters for better interpretation of the test conditions. For example, mass velocity is often reported instead of the mass flow rate in internal flow experiments to include the effect of the channel size. Below are listed such parameters and their relationship to the measured parameters.

Mass velocity

$$G = \frac{\dot{M}}{A_{\text{ch}}} = \frac{\dot{M}}{W_{\text{ch}} \times H_{\text{f}} \times N_{\text{ch}}} \quad (\text{B.1})$$

where A_{ch} is the total cross sectional area of the channels.

Subcooling

$$\Delta T_{\text{sub}} = T_{\text{sat}}(p_{\text{in}}) - T_{\text{in}} \quad (\text{B.2})$$

where the corresponding T_{sat} of p_{in} is computed with the NIST REFROP software.

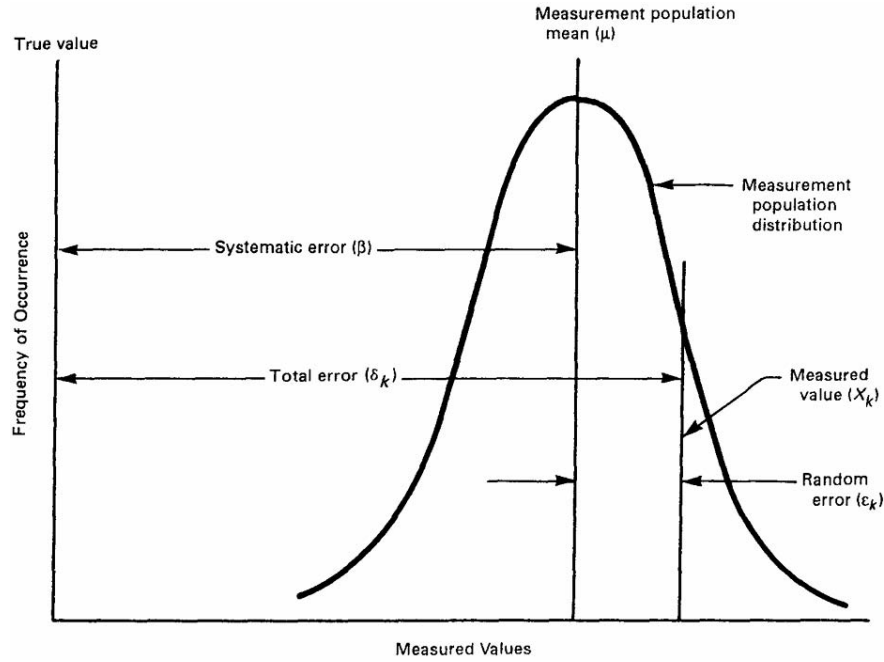


Figure B.1: Illustration of the systematic and random error [4].

Base heat flux

$$q_b = \frac{V \cdot I}{A_h} \quad (\text{B.3})$$

where V , I , A_h are the voltage, the current and the area of the heater, respectively.

Wall heat flux The procedures to calculate the wall heat flux in a rectangular channel include an iteration process to calculate the heat transfer coefficient and the fin efficiency, all together. This is described in detail in Chapter 3.2.2.

2. List Elemental Uncertainty Sources

Uncertainties can be categorized as either a systematic error or as a random error (Figure B.1). The random error can be calculated from a number of data gathered from repeated measurements. When the degrees of freedom is sufficiently large (> 30), the random error of a measurement with 95% confidence level is approximately twice its standard deviation. Table B.2 shows the summary of the standard deviation of each parameter from repeated measurements. Since the dimensions of the geometries were treated as constant, there is no deviation between the repeated experiments. The uncertainty of its measurement was counted in the systematic error.

Unlike the random error, the systematic error cannot be quantified absolutely so that the uncertainty due to systematic error must be estimated. The systematic uncertainty estimate is based on engineering judgement and analysis of elemental systematic errors, which include manufacturer's specifications, the uncertainty of the calibration and experimenter's experience. Every effort must be made to identify and account for all elemental systematic errors including the effect of ambient temperature, spatial variation and mounting

Table B.2: Random error of each parameter

Parameter	Mean value (\bar{X})	Number of Samples (N)	Sample Standard Deviation (S_X)
Inlet fluid temperature, T_{in}	20.1°C	30	0.005
Outlet fluid temperature, T_{o}	18.5°C	30	0.044
Inlet pressure, p_{in}	2.73 bar	30	0.00009
Outlet pressure, p_{o}	2.18 bar	30	0.0006
Heating power, Q	529 W	30	0.37
Mass flow rate, \dot{M}	23.2 kg/h	30	0.02
Wall temperature, T_{w}	76.8°C	30	0.16
Heating area, A_{h}	4 cm ²	1	0
Channel width, W_{ch}	199 μm	1	0
Channel height, H_{f}	756 μm	1	0
Distance from heater front, z	9 mm	1	0

location, etc. Below are listed the main elemental uncertainty sources for each measurement.

Inlet and outlet fluid temperature Fluid temperature was measured with a thermocouple inserted into the tube near the inlet port. Even though platinum thermometers of 0.03°C uncertainty were used to calibrate the thermocouples, the uncertainty of the inlet flow temperature was estimated to be 0.1°C considering a spatial variation inside the tube and ambient effect.

Heating power From the manufacturer's specifications, the current measurement from the power supply has an uncertainty of 0.09 A (0.75% of I_{max} + 1 count) while the voltage measurement from the NI data acquisition card is 0.06% of the value, i.e. maximum 0.18 V for 300 V. They yield less than 0.02 W for the uncertainty of the power input measurement. However, the actual heat delivered to the fluid differs from the heat input as shown in Chapter 4.1. This maximum discrepancy (5%) from the heat loss was treated as an additional elemental uncertainty sources for the heating power estimation. Moreover, it was found that irrevocable dryout and actual damage of the heater occurred at heat fluxes a few percent higher than that ascribed to be CHF by the current method. Therefore, the error due to the CHF detection method was estimated marginally to be 10% for estimating the heating power at the moment of CHF.

Mass flow The mass flow meter was calibrated by its provider before purchase and has an uncertainty of 0.1% of rate.

Inlet and outlet pressure The absolute pressure gage was calibrated with an oil balance, Industrial Dead-weight Tester from the Barnet Instruments Ltd.. However, considering a mounting effect as well as the tube connection from the actual location and the gage, 10 mbar was considered for its uncertainty. From

the manufacturer's specifications, the uncertainty of the pressure measurement is 0.075% of the set span for long-term use, yielding 7.5 mbar for the 10 bar range. Comparison between the measurement of the absolute pressure gage and that of the differential pressure gage confirmed the validity of 10 mbar error estimation.

Dimension of geometries Dimensions of the geometries such as the channel size were computed by averaging repeated measurements and their standard deviation yielded the measurement uncertainty. For the data reduction process, dimension values were treated as constants. However, their uncertainties contributed to the total uncertainty of the results.

Wall temperature Since the thermocouples were inserted and soldered manually, the contact resistance between the thermocouple and the copper test section are not identical for all the 10 thermocouples. Even though correction was made with one dimensional thermal conduction theory using an estimated average contact resistance, the discrepancy of the contact resistances caused some scatter between the thermocouple values. However, even though a marginal estimation 5°C was chosen, it was revealed as a result of the uncertainty analysis that the error of the wall temperature measurement influenced little on the estimation of the local heat flux.

Table B.3: Elemental systematic error sources.

Parameter	Elemental uncertainty source	Combined elemental systematic uncertainty ($B = [\sum_{i=1}^K b_i^2]^{\frac{1}{2}}$)
Inlet/Outlet fluid temperature $T_{\text{in}}, T_{\text{o}}$	Calibration Spatial variation Mounting effect Ambient temperature effect	0.1°C
Inlet/Outlet pressure $p_{\text{in}}, p_{\text{o}}$	Calibration Spatial variation Mounting effect Ambient temperature effect	10 mbar
Heating power at CHF $Q(\text{W})$	Voltage measurement Current measurement Heat loss to ambient CHF detection method	11%
Mass flow rate $\dot{M}(\text{kg/h})$	Calibration Mounting effect (Refrigerant) Ambient temperature effect	0.1%
Wall temperature T_{w}	Disturbance by the existence of thermocouple Contact resistance	5°C
Heating area $A_{\text{h}}(\text{cm}^2)$	Measurement error	5%
Channel width W_{ch}	Measurement error	3 μm
Channel height H_{f}	Measurement error	6 μm
Distance from heater front z	Measurement error	1 mm

Table B.4: Measurement uncertainty summary.

Symbol	Mean value (\bar{X})	Systematic Uncertainty ($B = [\sum_{i=1}^K b_i^2]^{\frac{1}{2}}$)	Sample Standard Deviation (S_X)	Total Uncertainty of a Measurement (U_{95})
$T_{in}(^{\circ}\text{C})$	20.1	0.1	0.005	0.1
$T_o(^{\circ}\text{C})$	18.5	0.1	0.044	0.2
$p_{in}(\text{bar})$	2.73	0.01	0.0001	0.01
$p_o(\text{bar})$	2.18	0.01	0.0006	0.01
$Q(\text{W})$	529	58.2	0.4	58.2
$\dot{M}(\text{kg/h})$	23.2	0.03	0.022	0.05
$T_w(^{\circ}\text{C})$	76.8	5	0.16	5.0
$A_h(\text{cm}^2)$	4	0.2	0	0.2
$W_{ch}(\mu\text{m})$	199	3	0	3
$H_f(\mu\text{m})$	756	6	0	6
$z(\text{mm})$	9	0.1	0	0.1

3. Calculate the Systematic and Random Standard Deviation

The mean values and uncertainty components of each measured parameter mentioned in the previous section are summarized in Table B.4.

4. Propagate the Systematic and Random Standard Deviation

The experimental results which cannot be measured directly are calculated as a function of basic parameters such as temperature and pressure.

$$R = f(\bar{P}_1, \bar{P}_2, \dots, \bar{P}_J) \quad (\text{B.4})$$

For example, the wall heat flux can be expressed in terms of the average values of the independent parameters mentioned in the data reduction process of Chapter B,

$$q_w = \frac{q_b(W_{ch} + W_f)}{(W_{ch} + 2\eta H_f)} = f(\bar{q}, \bar{\eta}) \quad (\text{B.5})$$

where the fin efficiency, η , is replaced again with measurable basic parameters.

$$q_w = f(\bar{q}, \bar{T}_{in}, \bar{p}_{in}, \bar{p}_o, \bar{\dot{M}}, \bar{T}_w) \quad (\text{B.6})$$

To compute the propagation of the parameter errors in the results, the contribution of each parameter should be identified. In the current analysis, this contribution was expressed with sensitivity coefficients.

Table B.5: Propagation of measurement uncertainties in the local wall CHF.

Parameter	Mean value (\bar{X})	Sensitivity Coefficient (θ)	θB W/cm ²	$\theta S_{\bar{X}}$ W/cm ²
Inlet fluid temperature, T_{in}	20.1°C	5.5E-04	5.5E-05	2.8E-06
Outlet fluid temperature, T_o	18.5°C	4.6E-05	4.6E-06	2.0E-06
Inlet pressure, p_{in}	2.73 bar	1.2E-01	1.2E-03	1.1E-05
Outlet pressure, p_o	2.18 bar	7.8E-02	7.8E-04	5.0E-05
Heating power, Q	529 W	1.1E-01	6.1E+00	4.0E-02
Mass flow rate, \dot{M}	23.2 kg/h	-4.5E-04	-1.0E-05	-1.0E-05
Wall temperature, T_w	76.8°C	-1.7E-02	-8.7E-02	-2.8E-03
Heating area, A_h	4 cm ²	-1.4E+01	-2.8E+00	0.0E+00
Channel width, W_{ch}	199 μ m	4.7E-02	1.4E-01	0.0E+00
Channel height, H_f	756 μ m	-6.3E-02	-3.8E-01	0.0E+00
Distance from heater front, z	9 mm	-4.4E-03	-4.4E-04	0.0E+00

The sensitivity is defined as the ratio of the change in a result to a unit change of a parameter. The sensitivity coefficient of each parameter is determined either analytically or numerically with Equation B.7:

$$\theta_i = \frac{\partial R}{\partial \bar{P}_i} = \frac{\Delta R}{\Delta \bar{P}_i} \quad (B.7)$$

In some cases with a complicated data reduction process, it is almost impossible to calculate the sensitivity coefficient analytically. In this research, a numerical approach was employed using a Matlab function. First, a Matlab function was developed to calculate the result, R using \bar{P}_i . Next, the same calculation was repeated using $(\bar{P}_i + \Delta \bar{P}_i)$ to obtain $(\bar{R}_i + \Delta \bar{R}_i)$. The sensitivity of each parameter and its contribution on the local wall heat flux at the moment of CHF is shown in Table B.5. The amount of each contribution represents the main sources of error. Only the systematic error of estimating heating power at the moment of CHF and the heating area have a contribution to the error of the local wall heat flux. Although the dimensions of channel and the wall temperature measurement are known to have a huge impact on the heat transfer coefficient, the main source of error for CHF estimation was attributed to the error from the heat flux estimation. This result justifies the use of the current thermocouple for the measurement of CHF.

Table B.6 and B.6 show the parameters that have contribution to the mass velocity and the subcooling.

5. Calculate The Uncertainty

The standard deviation and systematic uncertainty of a single test result are calculated from the propagation equation as

Table B.6: Propagation of measurement uncertainties in the mass velocity.

Parameter	Mean value (\bar{X})	Sensitivity Coefficient (θ)	θB W/cm ²	$\theta S_{\bar{X}}$ W/cm ²
Mass flow rate, \dot{M}	23.2 kg/h	63.7	1.48	1.42
Channel width, W_{ch}	199 μm	-7.41	-22.24	0
Channel height, H_{f}	756 μm	-1.95	-11.71	0

Table B.7: Propagation of measurement uncertainties in the local wall CHF.

Parameter	Mean value (\bar{X})	Sensitivity Coefficient (θ)	θB W/cm ²	$\theta S_{\bar{X}}$ W/cm ²
Inlet fluid temperature, T_{in}	20.1°C	-1	-0.1	-0.005102
Inlet pressure, p_{in}	2.73 bar	10.9	0.11	0.001

$$S_R = \left[\sum_{i=1}^J (\theta_i S_{\bar{P}_i})^2 \right]^{\frac{1}{2}} \quad (\text{B.8})$$

$$B_R = \left[\sum_{i=1}^J (\theta_i B_{\bar{P}_i})^2 \right]^{\frac{1}{2}} \quad (\text{B.9})$$

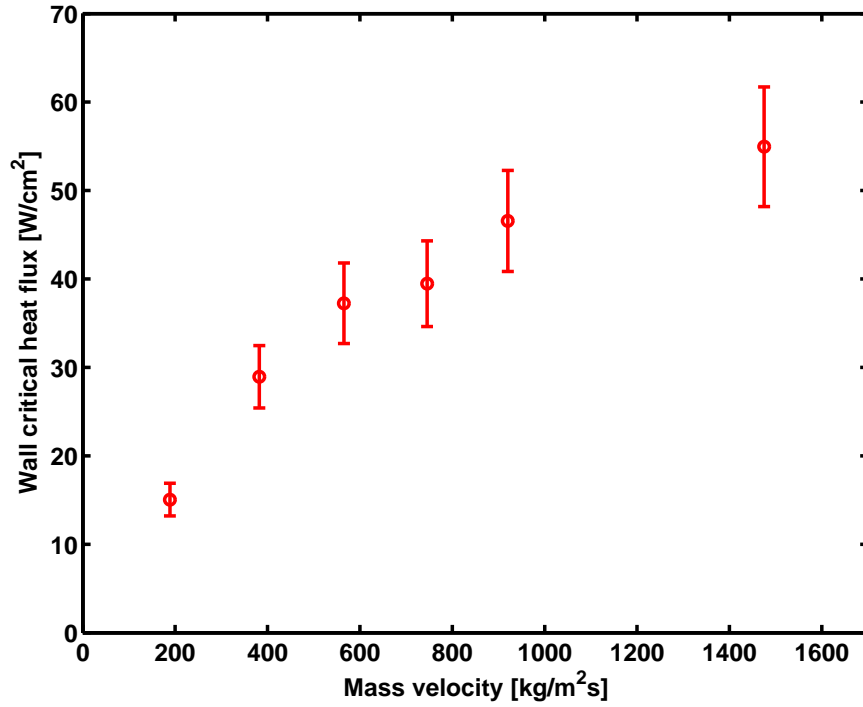
When the degree of freedom is sufficiently large (> 30), the uncertainty of a result with 95% confidence level is

$$U_{R_{95}} = 2 \left[\left(\frac{B_R}{2} \right)^2 + (S_R)^2 \right]^{\frac{1}{2}} \quad (\text{B.10})$$

Table B.8 summarizes the total uncertainty of each result after the propagation of errors. In the current condition, the wall CHF has an uncertainty of 12% while the mass velocity and subcooling are less than 2% and 3%, respectively. Figure B.2 shows an example of CHF results with their error bands. The flow condition is at $T_{\text{sat}} = 25^\circ\text{C}$ with R236fa in $H = 756 \mu\text{m}$ channels.

Table B.8: Uncertainty of the results

Parameter	Mean value (\bar{X})	Systematic Uncertainty, $B_R =$ $[\sum_{i=1}^J (\theta_i B_{\bar{P}_i})^2]^{\frac{1}{2}}$	Random Uncertainty, $S_R =$ $[\sum_{i=1}^J (\theta_i S_{\bar{P}_i})^2]^{\frac{1}{2}}$	Uncertainty, U_{R95}
Local wall CHF	54.9 W/cm ²	6.8	0.04	6.8 (12%)
Mass velocity	1475 kg/m ² s	25.2	1.4	25.3 (1.7%)
Subcooling	5.02°C	0.15	0.005	0.15 (3%)

Figure B.2: Wall CHF data for R236fa at $T_{\text{sat}} = 25^\circ\text{C}$ in $H = 756 \mu\text{m}$.

Conclusions

To calculate the propagation of errors in the results, the step by step procedure of ASME PTC 19.1 [4] was implemented. First of all, the uncertainty of each measurement was researched. The Coriolis mass flow meter has an uncertainty of $\pm 0.1\%$. The thermocouples and pressure transducers were calibrated with the data acquisition cards connected and have an uncertainty of $\pm 0.1^\circ\text{C}$ and ± 10 mbar, respectively. The input heating power from the voltage and current measurement result in an uncertainty of ± 0.02 W. The following uncertainty was estimated for each parameter and result: mass velocity $\pm 2\%$, inlet fluid temperature ± 0.1 K, inlet subcooling ± 0.2 K, base CHF $\pm 12\%$ and wall CHF $\pm 12\%$. The main contribution to the errors comes from the uncertainty of the heat flux estimation and the uncertainty of the geometrical dimensions of the microchannels. The main sources of the error for the heat flux estimation were revealed to be the error due to the method to determine the actual moment CHF occurs from the flow boiling curves, the heat loss to the ambient and the error in estimating the actual heating area.

Nomenclature

Roman letters

A	area	$[\text{m}^2]$
B	systematic uncertainty of a parameter	
b	systematic uncertainty associated with an elementary error source	
C	channel geometry dependent constant	
C_c	coefficient of contraction	
Co	confinement number	
c_{pl}	specific heat of liquid	$[\text{J}/\text{kgK}]$
D	diameter	$[\text{m}]$
D_h	hydraulic diameter	$[\text{m}]$
D_{he}	heated diameter	$[\text{m}]$
D_{eq}	area equivalent diameter	$[\text{m}]$
d	droplet deposition rate	$[\text{kg}/\text{m}^2\text{s}]$
e_B	boiling droplet entrainment rate	$[\text{kg}/\text{m}^2\text{s}]$
e_W	wave droplet entrainment rate	$[\text{kg}/\text{m}^2\text{s}]$
Fr	Froude number	
f	Fanning friction factor	
f_d	Fanning friction factor for fully developed flow	
G	mass velocity	$[\text{kg}/\text{m}^2\text{s}]$
G_1	upstream mass velocity	$[\text{kg}/\text{m}^2\text{s}]$
G_2	downstream mass velocity	$[\text{kg}/\text{m}^2\text{s}]$
G_h	mass velocity based on hydraulic diameter	$[\text{kg}/\text{m}^2\text{s}]$
G_{he}	mass velocity based on heated equivalent diameter	$[\text{kg}/\text{m}^2\text{s}]$

G_{eq}	mass velocity based on the actual cross sectional area of the channel	[kg/m ² s]
g	acceleration of gravity	[m/s ²]
H	height	[m]
H_{tc}	distance from thermocouple to microchannel bottom wall	[m]
h	heat transfer coefficient	[W/m ² K]
h	enthalpy	[J/kg]
h_{lv}	latent heat	[J/kg]
Δh_{in}	inlet subcooling enthalpy	[J/kg]
I	current	[A]
K	inlet subcooling parameter	
$K(\infty)$	incremental pressure drop number	
k_s	thermal conductivity of solid material	[W/mK]
L	length	[m]
M	pressure drop multiplier parameter	
\dot{M}	mass flow rate	[kg/s]
m	fin efficiency coefficient	
N	number of samples	
N_{ch}	number of channels	
P	fin perimeter	[m]
P	independent parameter	
Pe	Peclet number	
p	pressure	[Pa]
p_r	reduced pressure	[Pa]
Δp	pressure drop	[Pa]
Q	heating power	[W]
q	heat flux	[W/cm ²]
q_c	critical heat flux	[W/cm ²]
$q_{c,m}$	critical heat flux measured	[W/cm ²]
q_{c0}	critical heat flux for zero inlet subcooling	[W/cm ²]
$q_{c,p}$	critical heat flux predicted	[W/cm ²]

q_{OUB}	heat flux at the onset of unstable boiling	[W/cm ²]
R	internal radius of the tube	[m]
R	result	
Re	Reynolds number	
S_X	sample standard deviation	
T	temperature	[°C]
$T_{tc,i}$	wall thermocouple reading (i = 1 to 10)	[°C]
ΔT_{sub}	subcooling temperature	[K]
U_{95}	total uncertainty at a 95% confidence	
u	velocity	[m/s]
V	voltage	[V]
v	specific volume	[m ³ /kg]
We	Weber number	
W	width	[m]
\bar{X}	sample mean value	
x	vapor quality	
Y	Shah's correlating parameter	
z	distance in flow direction	[m]
z^+	dimensionless distance in flow direction	

Greek Letters

β	aspect ratio ranging from 0 to 1	
δ	film thickness	[μm]
$\Delta\delta_i$	height of the interfacial waves	[μm]
η	fin efficiency	
θ	sensitivity coefficient	
ξ	singular pressure drop coefficient	
μ	dynamic viscosity	[kg/m ² s]
ρ	density	[kg/m ³]
σ	surface tension	[N/m]

σ ratio of the cross sectional area at the upstream to that downstream

Subscripts

b base

c critical

c contraction

ch channel

e expansion

f fin

fric frictional

fl fluid bulk

h heater

in inlet

l liquid state

lv change of phase - liquid to vapor or vice versa

m measured

o outlet

ori orifice

p predicted

sat saturation

singular singular

v vapor state

w wall

Bibliography

- [1] AGOSTINI, B., BONTEMPS, A., AND THONON, B. Effects of geometrical and thermophysical parameters on heat transfer measurements in small-diameter channels. *Heat Transfer Engineering* 27 (2006), 14–24.
- [2] AGOSTINI, B., FABBRI, M., PARK, J., WOJTAN, L., THOME, J., AND MICHEL, B. State-of-the-art of high heat flux cooling technologies. *Heat Transfer Engineering* 28 (2007), 258–281.
- [3] AGOSTINI, B., REVELLIN, R., THOME, J. R., FABBRI, M., MICHEL, B., CALMI, D., AND KLOTTER, U. High heat flux flow boiling in silicon multi-microchannels: Part iii. saturated critical heat flux of r236fa and two-phase pressure drops. *Int. J. Heat Mass Transfer* 51 (2009), 5426–5442.
- [4] ASME. *Test Uncertainty*. PTC 19.1-1998. American Society of Mechanical Engineers, New York, 1998.
- [5] BERGLES, A., AND KANDLIKAR, S. On the nature of critical heat flux in microchannels. *Journal of Heat Transfer* 127 (2005), 101–107.
- [6] BOWERS, M., AND MUDAWAR, I. High flux boiling in low flow rate, low pressure drop mini-channel and micro-channel heat sinks. *Int. J. Heat Mass Transfer* 37 (1994), 321–332.
- [7] BOWRING, R. *A simple but accurate round tube uniform heat flux dryout correlation over the pressure range 0.7-17 MN/m² (100-2500 psia)*, vol. 789. United Kingdom Atomic Energy Authority, 1972.
- [8] CELATA, G., CUMO, M., AND MARIANI, A. Assessment of correlations and models for the prediction of chf in water subcooled flow boiling. *Int. J. Heat Mass Transfer* 37 (1994), 237–255.
- [9] CELATA, G., MISHIMA, K., AND ZUMMO, G. Critical heat flux prediction for saturated flow boiling of water in vertical tubes. *Int. J. Heat Mass Transfer* 44 (2001), 4323–4331.
- [10] CHU, R. C., SIMONS, R. E., ELLSWORTH, M. J., SCHMIDT, R. R., AND COZZOLINO, V. Review of cooling technologies for computer products. *IEEE Transactions on Device and Materials Reliability* 4 (2004), 568–585.
- [11] COLEMAN, H. W., AND STEELE, W. G. *Experimentation and Uncertainty Analysis for Engineers*, second ed. John Wiley & Sons, New York, 1989.
- [12] COLGAN, E., FURMAN, B., GAYNES, M., GRAHAM, W., LABIANCA, N., MAGERLEIN, J., POLASTRE, R., ROTHWELL, M., BEZAMA, R., CHOUDHARY, R., MARSTON, K., TOY, H., WAKIL, J., ZITZ, J., AND SCHMIDT, R. A practical implementation of silicon microchannel coolers for high power chips. *IEEE Transactions on Components and Packaging Technologies* 30 (2007), 218–225.
- [13] COLLIER, J., AND THOME, J. *Convective Boiling and Condensation*, third ed. Oxford University Press, Oxford, 1994.

- [14] DORF, R. C., AND BISHOP, R. H. *Modern Control Systems*, ninth ed. Prentice-Hall, 2001.
- [15] FAULKNER, D., KHOTAN, M., AND SHEKARRIZ, R. Practical design of a $1000\text{W}/\text{cm}^2$ cooling system. In *19th IEEE SEMI-THERM Symposium* (2003), pp. 223–230.
- [16] HALL, D., AND MUDAWAR, I. Critical heat flux (chf) for water flow in tubes - i. compilation and assessment of world chf data. *Int. J. Heat Mass Transfer* 43 (2000), 2573–2604.
- [17] INCROPERA, F. P., AND DEWITT, D. P. *Fundamentals of Heat and Mass Transfer*, forth ed. John Wiley and Sons, 1996.
- [18] ISO. *Guide to the Expression of Uncertainty in Measurement*. International Organization for Standardization, Geneva, 1993.
- [19] KANDLIKAR, S. G., KUAN, W. K., WILLISTEIN, D. A., AND BORRELLI, J. Stabilization of flow boiling in microchannels using pressure drop elements and fabricated nucleation sites. *Journal of Heat Transfer* 128 (2006), 389–396.
- [20] KATTO, Y. General features of chf of forced convection boiling in uniformly heated rectangular channels. *Int. J. Heat Mass Transfer* 24 (1981), 1431–1419.
- [21] KATTO, Y. Critical heat flux. *Int. J. Multiphase Flow* 20 (1994), 53–90.
- [22] KATTO, Y., AND OHNO, H. An improved version of the generalized correlation of critical heat flux for the forced convective boiling in uniformly heated vertical tubes. *Int. J. Heat Mass Transfer* 27 (1984), 1641–1648.
- [23] KEW, P., AND CORNWELL, K. Correlations for prediction of boiling heat transfer in small diameter channels. *Applied Thermal Engineering* 17 (1997), 705–715.
- [24] KLINE, S. J., AND MCCLINTOCK, F. A. Describing uncertainties in single-sample experiments. *Mechanical Engineering* 75 (1953), 3–8.
- [25] KOOMEY, J. Estimating total power consumption by server in the u.s. and in the world. *available at: <http://www.koomey.com>* (2007).
- [26] KOSAR, A., KUO, C.-J., AND PELES, Y. Suppression of boiling flow oscillations in parallel microchannels by inlet restrictors. *Journal of Heat Transfer* 128 (2006), 251–260.
- [27] KOSAR, A., AND PELES, Y. Critical heat flux of r-123 in silicon-based microchannels. *Journal of Heat Transfer* 129 (2007), 844–851.
- [28] KUAN, W. V. *Experimental study of flow boiling heat transfer and critical heat flux in microchannels*. PhD thesis, Rochester Institute of Technology, 2006. *available at: <http://hdl.handle.net/1850/1887>*.
- [29] LIENHART-V, J. H., AND LIENHART-IV, J. H. *A heat transfer text book*, third ed. Phlogiston press, 2008.
- [30] MOFFAT, R. J. Contributions to the theory of a single-sample uncertainty analysis. *Transactions of the ASME: Journal of Fluids Engineering* 104 (1982), 250–260.
- [31] MOFFAT, R. J. Using uncertainty analysis in the planning of an experiment. *Transactions of the ASME: Journal of Fluids Engineering* 107 (1985), 173–178.
- [32] OH, C. H., AND ENGLERT, A. B. Critical heat flux for low flow boiling in vertical uniformly heated thin rectangular channels. *Int. J. Heat Mass Transfer* 36 (1993), 325–335.

- [33] PRIBYL, D. J., BAR-COHEN, A., AND BERGLES, A. E. An investigation of critical heat flux and two-phase flow regimes for upward steam and water flow. In *Proceedings of the 5th International Conference Boiling Heat Transfer* (Montego Bay, Jamaica, May 2003).
- [34] QU, W., AND MUDAWAR, I. Measurement and correlation of critical heat flux in two-phase micro-channel heat sink. *Int. J. Heat Mass Transfer* 47 (2004), 2045–2059.
- [35] REVELLIN, R., DUPONT, V., URSENBACHER, T., THOME, J., AND ZUN, I. Characterization of diabatic two-phase flows in microchannels: flow parameter results for r-134a in a 0.5mm channel. *Int. J. Multiphase Flow* 32 (2006), 755–774.
- [36] REVELLIN, R., QUIBEN, J. M., BONJOUR, J., AND THOME, J. Effect of local hot spots on the maximum dissipation rates during flow boiling in a microchannel. *IEEE Transactions on Components and Packaging Technologies* 31 (2008), 407–416.
- [37] REVELLIN, R., AND THOME, J. An analytical model for the prediction of the critical heat flux in heated microchannels. *Int. J. Heat Mass Transfer* 51 (2008), 1216–1225.
- [38] SCHNEIDER, B., KOSAR, A., AND PELES, Y. Hydrodynamic cavitation and boiling in refrigerant(r-123) flow inside microchannels. *Int. J. Heat Mass Transfer* 50 (2007), 2838–2854.
- [39] SHAH, M. Improved general correlation for critical heat flux during upflow in uniformly heated vertical tubes. *Int. J. Heat Fluid Flow* 8 (1987), 326–335.
- [40] SHAH, R., AND LONDON, A. *Laminar Flow Forced Convection in Ducts*. Academic Press, 1978.
- [41] TAITEL, Y. Flow pattern transition in two-phase flow. In *Proceedings of the Ninth International Heat Transfer Conference* (1990), pp. 237–234.
- [42] TAYLOR, J. R. *An Introduction to Error Analysis*, second ed. University Science Books, California, 1997.
- [43] THOME, J. R. *Engineering Data Book III: free book at website*. Wolverine Tube Incoperation, available at: <http://www.wlv.com/products/databook/db3/DataBookIII.pdf>, 2004.
- [44] THOME, J. R. State-of-the-art overview of boiling and two-phase flows in microchannels. *Heat Transfer Engineering* 27 (2006), 4–19.
- [45] WHITE, F. M. *Fluid Mechanics*, fourth ed. McGraw-Hill, 1999.
- [46] WOJTAN, L., REVELLIN, R., AND THOME, J. Investigation of saturated critical heat flux in a single uniformly heated microchannel. *Experimental Thermal and Fluid Science* 30 (2006), 765–774.
- [47] ZHANG, W., HIBIKI, T., MISHIMA, K., AND MI, Y. Correlation of critical heat flux for flow boiling of water in mini-channels. *Int. J. Heat Mass Transfer* 49 (2006), 1058–1072.

Curriculum Vitae

Personal Information

Name: PARK Jung Eung

Nationality: Korean

Date of birth: 17.12.1973

Email: jung-eung.park@epfl.ch

Education

2005-2008	Ph.D. in Mechanical Engineering EPFL (Swiss Federal Institute of Technology), Switzerland
1997-1998	Exchange research program in LMF (Laboratory of Fluid Mechanics) EPFL, Switzerland
1996-1999	M.S. in Aerospace Engineering KAIST (Korea Advanced Institute of Science and Technology), South Korea
1992-1996	B.S. in Aerospace Engineering KAIST, South Korea

Work Experience

2005-2008	Doctoral assistant in LTCM (Laboratory of Heat and Mass Transfer) EPFL, Switzerland
2000-2005	Thermal engineer (Senior Research Engineer) LG Electronics Inc., Digital Media/Storage Laboratory, Seoul, South Korea

Certificate and Awards

2008	Best poster award of Energy doctoral program in EPFL Research Day
2005	Top 5 best technical paper award (among 200+ researchers in LG DS Lab.)
2004	Top 5 best technical paper award (among 500+ researchers in LG DM Lab.)
2004	LG certified Black Belt in Six Sigma

Publications in International Journal

Park, J.E. and Thome, J.R. Critical Heat Flux in Multi-Microchannel Copper Elements with Low Pressure Refrigerants, *Int. J. Heat Mass Transfer*, in publication.

Agostini, B., Fabbri, M., Park, J.E., Wojtan, L., Thome, J.R. and Michel, B. State-of-the-art of High Heat Flux Cooling Technologies, *Heat Transfer Engineering*, vol. 28(4), 2007.

Publications in International Conference

Thome, J.R., Revellin, R., Agostini, B. and Park, J.E. Recent Advances in Thermal Modeling of Microevaporators for Cooling of Microprocessors, *Proceedings of the ASME International Mechanical Engineering Congress and Exposition (IMECE)*, Seattle, USA, November, 2007.

Thome, J.R., Revellin, R., Agostini, B. and Park, J.E. Cooling of Microprocessors Using Flow Boiling of Refrigerants in Micro-Evaporators, *Proceedings of 10th UK National Heat Transfer Conference*, Edinburgh, UK, September, 2007.

Park, J.E., Park, J., Dan, B., Seo, J., Choi, I. and Kim, J. Airflow Analysis in a Near Field Optical Disc System, *Proceedings of the International Symposium on Optical Memory 2005 (ISOM'05)*, Hawaii, July, 2005.

Park, J.E., Hong, S., Hwang, H., Lee, J. and Kim, W. A Study on the Thermal Problems of an Optical Pickup Actuator, *Proceedings of the 37th International Symposium on Microelectronics (IMAPS 2004)*, Long Beach, USA, November, 2004.

Park, J.E., Ryu, H., Lee, J. and Kim, W. Practical Thermal Design of Smart Display, *Proceedings of IMAPS Advanced Technology Workshop on Thermal Management for High-Performance Computing and Wireless Applications*, Palo Alto, USA, October, 2003.